

DOCTORAL THESIS

Numerical simulation of wooden boards considering morphological characteristics and complex failure processes

submitted in satisfaction of the requirements for the degree
Doctor of Science in Civil Engineering
of the Vienna University of Technology, Faculty of Civil Engineering

DISSERTATION

Numerische Simulation von Holzbrettern unter Berücksichtigung der Morphologie und komplexer Versagensprozesse

ausgeführt zum Zwecke der Erlangung des akademischen Grades eines
Doktors der technischen Wissenschaften
eingereicht an der Technischen Universität Wien, Fakultät für Bauingenieurwesen

von

Dipl.-Ing. **Markus Lukacevic**
Matr.Nr.: 0326057
Embelgasse 54/11, 1050 Wien, Österreich

Gutachter:

Univ. Prof. Dipl.-Ing. Dr. techn. DDr.h.c. **Josef Eberhardsteiner**
Institut für Mechanik der Werkstoffe und Strukturen
Technische Universität Wien
Karlsplatz 13/202, 1040 Wien, Österreich

Univ. Prof. Dr.-Ing. habil. **Michael Kaliske**
Institut für Statik und Dynamik der Tragwerke
Technische Universität Dresden
Georg-Schumann-Straße 7, 01062 Dresden, Deutschland

Wien, im Juli 2014

.....

Acknowledgements

This thesis is based on the work done during my employment as a research assistant at the Institute for Mechanics of Materials and Structures (IMWS) at the Vienna University of Technology (TU Wien). It would not have been possible without the help of numerous people who contributed to the scientific results and provided the essential boundary conditions for this work.

I especially thank my advisor Dr. Josef Füssl for his constant support and guidance throughout the last years. It was a pleasure to work with him and discuss all kinds of ideas extensively.

I would like to thank Associate Prof. Karin de Borst for introducing me to the world of wood research and for opening up the opportunity to pursue a PhD thesis at the IMWS, as well as for her supervision during the first years of my PhD. I also thank Dr. Christoph Hackspiel, on whose work the first two publications of this thesis are based.

Prof. Josef Eberhardsteiner, dean of the Faculty of Civil Engineering and former head of the IMWS, as well as the current head of the IMWS Prof. Christian Hellmich are thanked for their support as well as for creating a positive working environment. The work in the teaching team for strength of materials (Dr. Aram Amouzandeh, Dr. Andreas Fritsch, Dr. Stefan Scheiner, DI Krzysztof Luczynski) was a valuable experience. Prof. Michael Kaliske (TU Dresden, Germany) is thanked for serving as co-examiner of this thesis.

I am very thankful to current and former colleagues of the wood research group: Dr. Thomas Bader, Dr. Johannes Eitelberger, Dr. Stefan Gloimüller, DI Georg Hochreiner, Dr. Andreas Jäger, DI Georg Kandler, Dr. Christoph Kohlhauser, DI Wolfgang Lederer, DI Michael Schweigler, Dr. Reinhard Stürzenbecher and DI Christoph Wikete. I would like to thank the staff at the laboratory, who helped me during the preparation and conduction of the experiments, Wolfgang Dörner and Dr. Roland Reihnsner. In addition, I would like to thank Mag.(FH) Martina Pöll, Gabriele Ostrowski and Astrid Schuh for their help with various administrative issues. I would also like to thank DI Michael Griessner and DI Ralf Lampert for their cooperation during their Master's theses and their contributions to this thesis. Special thanks to my "room mates" Dr. Leopold Wagner and DI. Viktoria Vass, as well as Dr. Michael Dorn for all the discussions and for the great working environment.

Furthermore, I would like to thank my parents, my sister, her husband and my friends for their support during the last years.

Abstract

The naturally grown material wood exhibits a rather complex mechanical behavior. This is mainly caused by the growth-induced orthotropy of the clear wood material, and further increased by knots and the resulting fiber deviations in their vicinities.

A reliable prediction of the mechanical behavior of wooden boards and wood products by means of numerical simulation tools is not easy to accomplish. Nevertheless, for a better utilization and a more efficient use of this valuable building material, the demand for such prediction tools increases continuously. Motivated by this need, within this work, simulation tools for wooden boards were developed, enabling the consideration of realistic three-dimensional fiber deviations around knots and taking the complex mechanical behavior of clear wood into account. The resulting stress and strain fields within the elastic regime and the accuracy of the calculated fiber directions are validated by means of four-point bending tests, which are accompanied by full-field deformation measurements based on digital image correlation techniques.

Furthermore, a criterion, which indicates the point of structural failure, was developed. In the process, the effective strength values are determined by examining the qualitative stress changes in predefined volumes around knots. This approach is based on the formation of failure zones predominantly caused by perpendicular-to-grain tension in the vicinity of knots, and is confirmed by comparisons to four-point bending and tensile tests of wooden boards with various cross-sectional dimensions.

In a next step, the failure processes themselves were described and linked to the cell structure of wood, because the initiation and also the global direction of cracks on the macroscale are governed by structural features on the lower length scales. To depict this behavior accurately, all possible failure mechanisms for two repetitive units, representing late- and earlywood, respectively, are identified by an approach based on the extended Finite Element method. By using sampling techniques, a wide range of possible loading combinations were generated and applied to the two cell types. For all simulations, the obtained failure modes were evaluated, classified and global crack directions assigned. The following definition of two multisurface failure criteria with predefined global crack directions for the two cell types individually allows the implementation into subroutines of commercial Finite Element software. Through application of this approach by simulating tensile tests on the annual year ring scale its capability to reproduce essential failure mechanisms in wood correctly could be shown.

Finally, intended for direct practical application, the evaluation of common and the introduction of new indicating properties (IPs) for the strength grading of wooden boards are presented. While commonly used IPs hardly consider the 3D position and orientation of knots within wooden boards, new scanning techniques would allow highly improved yields within the wood grading process. Thus, algorithms for the manual and also automatic 3D reconstruction of wooden boards are presented. Based on this new knot information, novel IPs were developed, which allow for the consideration of knots, resulting fiber deviations and the knot location, which plays an important role under bending load. A statistical evaluation of common and novel IPs shows that by using these additional information significant improvements can be reached.

Kurzfassung

Der natürlich gewachsene Baustoff Holz weist ein komplexes Materialverhalten auf. Hauptursache dafür ist die wuchsinduzierte Orthotropie des astfreien Materials, zusätzlich jedoch wird dieser Effekt durch das Vorhandensein von Ästen und den daraus resultierenden Faserabweichungen verstärkt.

Eine zuverlässige Vorhersage des mechanischen Verhaltens von Holzbrettern und Holzprodukten mittels numerischer Simulationstools ist daher nicht einfach umzusetzen. Allerdings vergrößert der Wunsch nach einer besseren Ausnutzung bzw. einer effizienteren Verwendung dieses wertvollen Baustoffs den Bedarf für solche Vorhersagemodelle laufend. Dadurch motiviert wurden in dieser Arbeit Simulationstools für Holzbretter entwickelt, die die Berücksichtigung von realistischen dreidimensionalen Faserläufen rund um Äste und des komplexen Materialverhaltens von astfreiem Material ermöglichen. Die resultierenden Spannungs- und Verzerrungsfelder im elastischen Bereich und die Genauigkeit der berechneten Faserrichtungen werden mittels vollflächigen Verformungsmessungen an 4-Punkt-Biegeversuchen validiert.

Weiters wurde ein Kriterium zur Bestimmung des Zeitpunkts des Strukturversagens entwickelt. Dabei werden die qualitativen Spannungsänderungen in vorher definierten Volumen rund um die Äste analysiert. Diese Herangehensweise basiert auf der Entstehung von Versagenszonen in der Nähe der Äste, welche hauptsächlich durch Zugspannungen quer zur Faserrichtung verursacht werden. Dies wurde durch Vergleiche mit 4-Punkt-Biege- und Zugversuchen von Holzbrettern mit unterschiedlichen Querschnittsabmessungen bestätigt.

Im nächsten Schritt wurden die Versagensmechanismen selbst beschrieben und mit der Zellstruktur von Holz in Verbindung gebracht, weil sowohl die Rissinitiierung als auch die globale Richtung der Risse auf der Makroskala von den Struktureigenschaften der kleineren Längenskalen bestimmt werden. Um dieses Verhalten korrekt abbilden zu können, wurden alle möglichen Versagensmechanismen von zwei sich wiederholenden Einheitszellen ermittelt, welche Früh- bzw. Spätholz abbilden. Dabei wurde die sogenannte „eXtended Finite Element Method“ angewandt. Mittels eines Stichprobenverfahrens wurde eine Vielzahl möglicher Belastungskombinationen erstellt und die beiden Einheitszelltypen damit entsprechend belastet. Für alle Simulationen wurden die entstandenen Versagenszustände ausgewertet, klassifiziert und globalen Rissrichtungen zugeordnet. Die daraus folgende Festlegung von zwei Mehrflächen-Versagenskriterien mit zugeordneten Rissrichtungen für die beiden Zelltypen erlaubt eine Implementierung in Subroutinen von kommerzieller Finite-Elemente-Software. Die Anwendung dieser Methode auf Simulationen von Zugversuchen auf der Jahrringskala zeigte, dass damit die entscheidenden Versagensmechanismen in Holz korrekt abgebildet werden können.

Um eine direkte Anwendbarkeit zu ermöglichen, werden in einem letzten Schritt herkömmliche Sortierkriterien für die Festigkeitssortierung von Holzbrettern evaluiert und neue vorgestellt. Während herkömmliche Kriterien die 3D-Lage und Orientierung von Ästen kaum berücksichtigen, würden neuartige Scantechnologien eine weitaus höhere Ausbeute im Sortierprozess erlauben. Deshalb werden Algorithmen für die manuelle und auch die automatische 3D-Rekonstruktion von Holzbrettern vorgestellt. Basie-

rend auf den neuen Astinformationen werden neuartige Sortierkriterien entwickelt, welche die Berücksichtigung von Ästen, resultierenden Faserabweichungen und, vor allem für den Fall einer Biegebelastung, Astlagen ermöglichen. Eine statistische Auswertung von herkömmlichen und neuartigen Sortierkriterien zeigt, dass durch den Gebrauch dieser zusätzlichen Informationen signifikante Verbesserungen erreicht werden können.

Contents

Introduction	1
Motivation	1
Basic description of the used methods	2
Elastic material behavior	2
Inelastic material behavior	4
Cohesive elements	6
Extended finite element method	7
Research Objectives and Outline of the Thesis	15
Contribution by the author	17
1 Numerical simulation tool for wooden boards with a physically based approach to identify structural failure (Lukacevic and Füssl, 2014)	18
1.1 Introduction	19
1.2 Numerical simulation tool	22
1.2.1 Geometrical model	22
1.2.2 Mechanical model	24
1.2.3 Preliminary results	25
1.3 Structural failure criterion	26
1.4 Validation	30
1.4.1 Materials and methods	30
1.4.2 Results	34
1.5 Conclusion	35
2 Performance assessment of a numerical simulation tool for wooden boards with knots by means of full-field deformation measurements (Lukacevic et al., 2014a)	37
2.1 Introduction	38
2.2 Materials and methods	39
2.2.1 Full-field deformation measurements	40
2.3 Test results and evaluation	42
2.3.1 Strain distributions	43
2.4 Numerical analyses	48
2.4.1 Strain fields	50
2.4.2 Principal strain directions	52

2.4.3	Structural failure	54
2.5	Conclusion and future work	55
2.6	Appendix	55
3	Failure mechanisms of clear wood identified at wood cell level by an approach based on the extended finite element method (Lukacevic et al,2014b)	62
3.1	Introduction	63
3.2	Theoretical background	64
3.3	Materials and cell geometry	65
3.3.1	Wood cells	66
3.4	Methods and results	70
3.4.1	Unit cell method	70
3.4.2	Simulation program	71
3.4.3	Identification of failure modes	72
3.5	Application to annual ring scale	83
3.5.1	Method	83
3.5.2	Comparison of simulation and experimental results	84
3.6	Conclusions and outlook	85
4	Discussion of common and introduction of new indicating properties for the strength grading of wooden boards (Lukacevic et al., 2014c)	87
4.1	Introduction	88
4.1.1	State of the art	89
4.1.2	Motivation	92
4.2	Experiments	93
4.2.1	Selection of material	93
4.2.2	Four-point bending tests	93
4.3	Geometrical reconstruction of test specimens	94
4.3.1	Manual reconstruction	95
4.3.2	Automatic reconstruction	96
4.4	Indicating properties	98
4.4.1	Common indicating properties	98
4.4.2	Novel indicating properties	99
4.5	Assessment of indicating properties	101
4.5.1	Evaluation of common indicating properties	101
4.5.2	Evaluation of novel indicating properties	105
4.6	Conclusions	111
	Conclusions and Outlook	113
	Main Findings Concerning the Mechanical Behavior of Wooden Boards with Knots	113
	Perspectives and Future Research Studies	115
	Bibliography	116

CONTENTS	iii
Publications and Conference Contributions	126
Curriculum Vitae	128

Introduction

Motivation

In comparison to other building materials, such as concrete or steel, wood exhibits a much more complex material behavior. Mainly responsible for this is the growth-induced orthotropy of the clear-wood material and growth irregularities like knots, turning wooden boards into a strongly inhomogeneous building material. For this reason, existing design schemes are, to a large extent, based on empirical parameters and relationships, derived from comprehensive experimental programs. Accurate predictions of stress and strain distributions as well as failure mechanisms in wooden boards obtained from numerical simulation tools hardly exist and are quite difficult to gain.

In recent years, developments with respect to the identification of the wooden morphology, newly applied measurement methods delivering necessary data for the validation of prediction tools, and ever-increasing computing power opened up new possibilities in this field. An appropriate numerical simulation of the complex wooden behavior becomes possible. A contribution to this trend represents this work, in which sophisticated material models are used together with finite element approaches to describe the complex mechanical behavior of wooden boards at different scales of observation.

Considering a typical loading of a wooden board/product, the following characteristic regimes or points of interests, respectively, can be distinguished:

1. An **elastic regime**, where no plastic effects and failure processes occur. At this stage, the stress and strain fields within the material are of interest to predict the limit of serviceability of wooden products. Within this work, these stress and strain fields are predicted with a developed 3D numerical simulation tool, taking the orthotropic nature and the fiber deviations around knots into account. The obtained numerical results are validated by means of full-field deformation measurements, using the digital image correlation (DIC) technique. This comparison can be found in **Publication 2**.
2. The **point of structural failure**. Since wood allows for very localized highly plasticized zones without leading to structural failure, an identification of this point is quite difficult. Empirical correlations with experimental results are the common approach to overcome this problem. By analyzing the stress states, obtained with the developed simulation tool, around knots in detail, a physically-based structural failure criterion could be derived, which is presented in **Publication 1**.

This criterion has been validated by means of four-point bending tests on wooden boards with different dimensions.

3. Finally, a realistic simulation of the **failure mechanisms** in wood is one of the biggest challenges, because of very brittle material behavior and difficult to define crack directions, due to the orthotropic structure. For this purpose, a multi-surface failure criterion was derived, linking crack initiation and crack directions to microstructural characteristic at the wood cell level. An implementation of this model in the framework of an extended finite element approach showed that essential failure modes in clear-wood, derived from experiments, were able to be reproduced. This multiscale failure approach is presented in **Publication 3**.

Despite the powerful possibilities of numerical simulation tools, they serve mainly to gain scientific knowledge and to validate models, which are efficient enough for direct application in timber industry. For this reason, the morphological information gained as input for the simulation tools and the obtained experimental results were used to derive new indicating parameters for strength grading (see **Publication 4**).

In the following, the used methods for the numerical simulation tools are generally described. Afterwards, research objectives and the outline of the individual Publications can be found, before Publications 1 to 4 are presented. Finally, the main findings of this thesis are summarized and an outlook to future developments based on this work is given.

Basic description of the used methods

Within this section, the basics of the methods used within this work are described. For a realistic numerical simulation of the complex material behavior of wood, sophisticated material models are required, which are able to describe the anisotropic material behavior accurately.

The characterization of the material behavior is done in two steps. First, the elastic material behavior is described briefly, and then several methods for the description of inelastic material behavior are presented.

Elastic material behavior

The elastic material behavior at the clear wood level can be described suitably by an orthotropic stiffness tensor. As the elastic properties highly vary with variations of density, moisture content and microfibril angle (MFA), and a numerical simulation tool will be used to simulate experiments exhibiting such variations, a previously developed micromechanical model (Hofstetter et al., 2005, 2007) is used for the determination of the stiffness tensor. This model relates the macroscopic mechanical behavior to physical quantities at lower length scales, allowing the consideration of structural differences at these scales. For the accurate description of these differences three homogenization steps were developed (see Figure 1) (Hofstetter et al., 2007). It can be seen that the wood

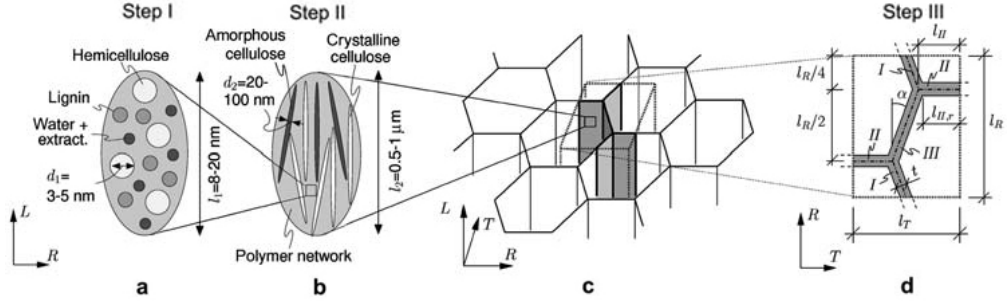


Figure 1: Combined random/periodic multi-step homogenization scheme for softwood elasticity: (a) RVE of polymer network; (b) RVE of cell wall material; (c) honeycomb structure of softwood; and (d) unit cell of softwood (Hofstetter et al., 2007).

cells (length scale: 20 to 40 μm), which are hollow tubes oriented in stem direction, are arranged in a honeycomb-like structure within the well-known two layers of clear wood, namely early- and latewood. The cell wall (cell wall thickness: 2 to 20 μm) material itself is built up by several cell wall layers, in which highly oriented cellulose microfibrils (fiber diameter: 50 to 200 nm) are embedded in a polymer matrix.

Thus, to model the mechanical properties at the macroscale, we have to start at the lowest scale.

Polymer network

In the first step of the homogenization scheme, the stiffness tensor of the polymer network, which is made up of hemicellulose, lignin, water and extractives, is determined by means of continuum micromechanics. The fundamentals of such an approach is the definition of a so-called representative volume element (RVE) with a characteristic length l (Zaoui, 2002). The separation of scales must be fulfilled at every hierarchical step. This means that the characteristic length l of the RVE has to be at least an order of magnitude larger than the characteristic length d of the inhomogeneities within the RVE ($l \gg d$) and at least an order of magnitude smaller than a characteristic dimension L of the investigated macroscopic structure and than the fluctuation length λ of its mechanical loading, $l \ll L, l \ll \lambda$.

For the polymer network a dispersed arrangement of the phases is assumed, and, thus, a self-consistent scheme with spherical inclusions is applied. The effective stiffness \mathbb{C}^{est} can be estimated by using a formulation by Zaoui (2002), which is based on Eshelby's solution for matrix-inclusion problems:

$$\mathbb{C}^{est} = \sum_r f_r \mathbb{C}_r : [\mathbb{I} + \mathbb{P}_r^0 : (\mathbb{C}_r - \mathbb{C}^0)]^{-1} : \left\{ \sum_s f_s [\mathbb{I} + \mathbb{P}_s^0 : (\mathbb{C}_s - \mathbb{C}^0)]^{-1} \right\}^{-1}, \quad (1)$$

where \mathbb{C}_r represents the elastic stiffness tensor, f_r the volume fraction and \mathbb{P}_r the characteristic shape of phase r in a matrix with stiffness \mathbb{C}^0 . For the polymer network, Equa-

tion 1.4 is specified for the three inclusions with stiffnesses \mathbb{C}_{hemcel} , \mathbb{C}_{lig} and \mathbb{C}_{H_2Oext} , for $\mathbb{C}^0 = \mathbb{C}_{polymer}^{SCI}$ and for $\mathbb{P}^0_{hemcel} = \mathbb{P}^0_{lig} = \mathbb{P}^0_{H_2O+Ext} = \mathbb{P}^{polymer}_{sph}$. The resulting stiffness tensor $\mathbb{C}_{polymer}^{SCI}$ now contains all the necessary information about the microstructure within the considered RVE, namely volume fractions, stiffnesses, morphology and shape of the inclusions.

Cell wall material

The second step of the homogenization scheme considers the embedment of cellulose fibers into the polymer matrix of the previous step. The shape of these inclusions motivates the use of the Mori-Tanaka scheme (Mori and Tanaka, 1973). There, Equation 1.4 is specified for two cylindrical inclusion phases (for crystalline and amorphous cellulose) with stiffnesses \mathbb{C}_{crycel} and \mathbb{C}_{amocel} and one polymeric matrix phase with stiffness $\mathbb{C}_{polymer}^{SCI}$ from the first step.

Wood cell structure

In the third homogenization step, the so-called unit cell method (Michel et al., 1999; Suquet, 1997; Böhm, 2004) is used to describe the periodic microstructure of the wood cells. This modeling approach allows the description of a heterogeneous material with repetitive features by means of a basic periodically repeating unit, the so-called unit cell. By subjecting the unit cell to periodic boundary conditions and analyzing the mechanical response of this unit, the components of the macroscopic homogenized stiffness tensor can be obtained. With this method, it is possible to account for the plate-like bending and shear deformations of the cell walls of the tube-like wood cells, which cannot be achieved by means of the just presented continuum micromechanical techniques.

Inelastic material behavior

To simulate structural failure of wood, either some kind of material softening must be implemented into numerical simulation tools or other methods to estimate the point of structural failure have to be employed. Wood exhibits not only orthotropic material behavior in the elastic range, but also the strength values differ both in the principle material directions (L, R and T) and also in the tensile and compressive range, respectively. The tensile strength in fiber direction is usually bigger than the compressive strength. Whereas the tensile strength in perpendicular-to-grain direction is more than a magnitude lower than the strength in fiber direction. The simplest way to implement these material characteristics into a numerical model is the use of elasto-plastic material behavior. Thus, in the next section several plasticity models are presented. Next, cohesive elements are introduced, which can be used to model the cracking of structures. The drawback of such elements is that the crack path is not independent, but predefined by the location of the cohesive layers. Thus, at the end of this section, the eXtended Finite Element method is described in detail, which can be used for studying the cracking behavior of structural elements without predefining the crack paths and without the need for remeshing.

Elasto-plastic material behavior

The elastic limit state is usually identified by means of a yield criterion. This limit is reached when the corresponding yield function $\Phi(\boldsymbol{\sigma})$ reaches a value of 0. For $\Phi(\boldsymbol{\sigma}) < 0$ the stress state is elastic and stress states resulting in $\Phi(\boldsymbol{\sigma}) > 0$ are inadmissible if no hardening is considered. If $\Phi(\boldsymbol{\sigma}) = 0$ is interpreted as a yield surface, then all stress states lying within the surface represent elastic stress states and points lying on the surface plastic ones.

As already mentioned, wood is an orthotropic material with different strength properties in the three principle material directions and also with varying tensile and compressive strengths in all three directions. Thus, only orthotropic yield surfaces are feasible for the description of the material behavior of wood.

Hill (1948) introduced an extension of the von Mises yield criterion in a quadratic form, reading

$$\Phi(\boldsymbol{\sigma}) = a_1(\sigma_{22} - \sigma_{33})^2 + a_2(\sigma_{33} - \sigma_{11})^2 + a_3(\sigma_{11} - \sigma_{22})^2 + 2b_1\sigma_{23}^2 + 2b_2\sigma_{31}^2 + 2b_3\sigma_{12}^2 - 1 \leq 0. \quad (2)$$

This criterion allows a consideration of the different strength values in the principle material directions, but uses the same tensile and compressive strengths.

Based on this formulation, Hoffman (1967) introduced linear terms to account for the difference in tensile and compressive strength values:

$$\Phi(\boldsymbol{\sigma}) = C_1(\sigma_{22} - \sigma_{33})^2 + C_2(\sigma_{33} - \sigma_{11})^2 + C_3(\sigma_{11} - \sigma_{22})^2 + C_4\sigma_{11} + C_5\sigma_{22} + C_6\sigma_{33} + C_7\sigma_{23}^2 + C_8\sigma_{31}^2 + C_9\sigma_{12}^2 - 1 \leq 0, \quad (3)$$

where the constants C_1 to C_9 are nine independent material parameters.

The quadratic formulation of the highly used failure criterion of Tsai and Wu (1971) for orthotropic materials with different strengths in tension and compression reads as:

$$\Phi(\boldsymbol{\sigma}) = a_{ij}\sigma_{ij} + b_{ijkl}\sigma_{ij}\sigma_{kl} - 1 \leq 0. \quad (4)$$

If interactions between normal and shear stresses are neglected and symmetries are considered, the failure criterion can be reduced to

$$\begin{aligned} \Phi(\boldsymbol{\sigma}) = & a_{11}\sigma_{11} + a_{22}\sigma_{22} + a_{33}\sigma_{33} + \\ & b_{1111}\sigma_{11}^2 + b_{2222}\sigma_{22}^2 + b_{3333}\sigma_{33}^2 + \\ & 2b_{1122}\sigma_{11}\sigma_{22} + 2b_{2233}\sigma_{22}\sigma_{33} + 2b_{3311}\sigma_{33}\sigma_{11} + \\ & 4b_{1212}\tau_{12}^2 + 4b_{2323}\tau_{23}^2 + 4b_{3131}\tau_{31}^2 - 1 \leq 0, \end{aligned} \quad (5)$$

where for wood the twelve independent tensor components (a_{ij} , b_{ijkl}) of (3.13) are estimated according to Eberhardsteiner (2002) and Kollmann (1982) by using the following equations:

$$\begin{aligned} a_{11} &= \frac{1}{f_{yt1}} + \frac{1}{f_{yc1}}, & a_{22} &= \frac{1}{f_{yt2}} + \frac{1}{f_{yc2}}, & a_{33} &= \frac{1}{f_{yt3}} + \frac{1}{f_{yc3}}, \\ b_{1111} &= \frac{1}{f_{yt1}f_{yc1}}, & b_{2222} &= \frac{1}{f_{yt2}f_{yc2}}, & b_{3333} &= \frac{1}{f_{yt3}f_{yc3}}, \\ b_{1212} &= \frac{1}{4f_{y12}}, & b_{2323} &= \frac{1}{4f_{y23}}, & b_{3131} &= \frac{1}{4f_{y31}}, \end{aligned} \quad (6)$$

with subscripts t denoting tensile and c compressive strengths. Equations (6) show that most of the tensor components can be determined by using the material's uniaxial strength and shear strength values. The remaining components b_{1122} , b_{2233} and b_{3311} can be obtained by means of biaxial strength tests.

For a better approximation of the different failure modes in wood (e.g. brittle tensile and ductile compressive failure), several researchers developed multisurface plasticity models (Mackenzie-Helnwein et al., 2003; Kohlhauser, 2009; Schmidt and Kaliske, 2006).

The sole consideration of elastic-plastic material behavior at the integration point level is not very feasible if wooden elements are examined. This effect is increased by the ubiquitous defects, like knots and the resulting fiber deviations in their vicinities, in such elements. These lead to local stress concentrations, which makes it impossible to use maximum stress failure criteria at the integration point level for the estimation of structural failure.

This deficiency can be overcome by using so-called mean-stress approaches. Within his *Finite Small Area Theory*, Masuda (1988) evaluated ordinary stress criteria with averaged stresses of finite small areas. He showed that the optimum size of such an area is related to the typical wood fiber structure. Landelius (1989) developed a similar approach, the so-called *Finite Area Method*, in which he used results of common linear elastic fracture mechanics approaches to estimate the length of the finite area in grain direction. As within this work only mode I fracture mechanisms were considered, Aicher et al. (2002) extended this technique to also take into account the mode II fracture mechanisms with a mixed mode stress criterion. Several other researchers (Serrano and Gustafsson, 2006; Sjödin and Serrano, 2008; Sjödin et al., 2008) applied similar approaches for the simulation of single and multiple dowel connections. Furthermore, Guindos (2011) investigated various volume definitions with regard to size and shape, over which the stresses are averaged, and compared the results of several applied common failure criteria.

Cohesive elements

To model the cracking behavior of wood under tensile and shear loading directly, so-called cohesive elements can be used. These are special-purpose elements with zero thickness, which can be arranged in planes of the FE model where failure is expected. The crack path is restricted to the cohesive elements layers and cannot drift into the surrounding elements. The mechanical constitutive behavior of such cohesive elements can be defined by using a constitutive model specified directly in terms of traction versus separation.

Prior to damage, a linear elastic traction-separation behavior is assumed, where in the 3D case the traction stress vector consists of the normal traction t_n and the two shear tractions t_s and t_t , and is linked to the corresponding separations δ by the elasticity

matrix \mathbf{K} :

$$\mathbf{t} = \begin{Bmatrix} t_n \\ t_s \\ t_t \end{Bmatrix} = \begin{bmatrix} K_{nn} & K_{ns} & K_{nt} \\ K_{ns} & K_{ss} & K_{st} \\ K_{nt} & K_{st} & K_{tt} \end{bmatrix} \begin{Bmatrix} \delta_n \\ \delta_s \\ \delta_t \end{Bmatrix} = \mathbf{K} \delta \quad (7)$$

To model the damage behavior of cohesive elements, in addition, damage initiation criteria and damage evolution behavior must be defined. Common initiation criteria, found in commercial FE software, are maximum nominal stress or strain and quadratic stress or strain criteria:

$$\max \left\{ \frac{\langle t_n \rangle}{t_n^0}, \frac{t_s}{t_s^0}, \frac{t_t}{t_t^0} \right\} = 1 \quad (8)$$

$$\max \left\{ \frac{\langle \varepsilon_n \rangle}{\varepsilon_n^0}, \frac{\varepsilon_s}{\varepsilon_s^0}, \frac{\varepsilon_t}{\varepsilon_t^0} \right\} = 1 \quad (9)$$

$$\left\{ \frac{\langle t_n \rangle}{t_n^0} \right\}^2 + \left\{ \frac{t_s}{t_s^0} \right\}^2 + \left\{ \frac{t_t}{t_t^0} \right\}^2 = 1 \quad (10)$$

$$\left\{ \frac{\langle \varepsilon_n \rangle}{\varepsilon_n^0} \right\}^2 + \left\{ \frac{\varepsilon_s}{\varepsilon_s^0} \right\}^2 + \left\{ \frac{\varepsilon_t}{\varepsilon_t^0} \right\}^2 = 1 \quad (11)$$

In Equations (8) to (11), the symbol $\langle \rangle$ represents the Macaulay brackets, which are used to signify that only values greater than zero cause failure for the corresponding component, and the superscript "0" denotes the peak values of the respective stress and strain components when the deformation is purely normal to the interface or in one of the shear directions, respectively. Once the defined damage initiation criterion is reached, the material stiffness is degraded by means of a damage evolution law, represented by a scalar damage variable D , which initially has a value of 0 and monotonically increases to a value of 1, where no more stresses can be transferred through the cohesive element. Several types of such damage evolution laws exist, like e.g. linear or exponential softening laws or laws based on the dissipated energy.

Within this work, cohesive elements were not used for the determination of structural failure of timber elements, but cohesive material behavior by means of traction-separation laws were applied in the framework of XFEM.

Extended finite element method

In the conventional FEM the discretization error highly depends on the chosen shape functions and on the FE mesh. To reduce this error or to achieve higher accuracies in particular parts of an FE model the mesh can be refined (by altering the mesh size h and, thus, using many linear elements) or higher order shape functions (by enlarging the polynomial degree p and, thus, using few complex elements) can be implemented, also known as the h-method and the p-method, respectively. For certain problems, e.g. in case of singularities due to cracks, this leads to high numerical demands. The efficient use of special shape functions can thus reduce the discretization error significantly. As the exact location of such singularities is usually not known a priori, the modeling of moving cracks in the conventional FEM requires a continued updating of the FE mesh.

The presented eXtended Finite Element Method (XFEM) allows to avoid this major drawback of the conventional FEM. It was first introduced by Belytschko and Black (1999) and is based on the partition of unity method (Melenk and Babuska, 1996), which allows the enrichment of degrees of freedom with special displacement functions of a part of an examined structure. Thus, the mesh does not have to match the geometry of the discontinuities and only those nodes whose support is cut by the discontinuity are enriched. For the description of the crack typology the so-called level set method is used. Furthermore, the cohesive segments method allows the use of traction-separation laws for the description of the interaction behavior of cracked surfaces. In contrast to cohesive elements, potential crack surfaces do not have to be predefined within the XFEM.

Partition of unity

The basis of the XFEM is the partition of unity method (PUM), which was introduced by Melenk and Babuska (1996) and Babuska and Melenk (1997) and whose key feature is the capability of including a priori knowledge about local solution properties into the conventional FE approach.

Therefore, the total domain Ω is divided into n overlapping subdomains Ω_i . Then, a set of functions φ_i , whose region of influence is restricted to the corresponding subdomain Ω_i , forms a partition of unity, if their values sum up to unity at each point \mathbf{x} in the domain Ω :

$$\sum_{i=1}^n \varphi_i(\mathbf{x}) = 1 \quad \forall \mathbf{x} \in \Omega. \quad (12)$$

For example, the field variable $u(\mathbf{x})$ can now be approximated by

$$u(\mathbf{x}) \approx \sum_{i=1}^n \varphi_i(\mathbf{x}) \sum_{j=1}^{m_i} \alpha_{ij} f_j(\mathbf{x}), \quad (13)$$

with n being the number of subdomains, forming the partition of unity, and $f_j(\mathbf{x})$ being m_i specific functions within the partition, to which the free values α_{ij} are assigned to.

The partition of unity concept is fulfilled by the standard FE shape functions:

$$\sum_{i=1}^n N_i(\mathbf{x}) = 1. \quad (14)$$

This property of the PUM leads to the fact that the arbitrary extension functions $G(\mathbf{x})$, implemented for the enhancement of the local approximation properties, can be reproduced exactly in the partition region:

$$\sum_{i=1}^{NN} N_i(\mathbf{x}) G(\mathbf{x}) = G(\mathbf{x}). \quad (15)$$

This yields the implementation of the PUM into the XFEM framework:

$$u(\mathbf{x}) \approx \sum_{i=1}^{NN} N_i(\mathbf{x}) \left[a_i + \sum_{j \in \mathcal{N}_i} G_j(\mathbf{x}) b_{ij} \right], \quad (16)$$

where NN is the number of nodes in the FE mesh, \mathcal{N}_i the set of active extension functions at the corresponding node, a_i the conventional FE degrees of freedom and b_{ij} the extended degrees of freedom. In general, different shape functions $N_i(\mathbf{x})$ can be used for the conventional degrees of freedom and for the extended ones. The only restriction is that linear dependencies of shape functions must be avoided.

This ability of the PUM to enrich only a subset of nodes within a certain region of interest makes this method highly efficient and, thus, superior compared to conventional discretization approaches.

Description of discontinuous geometry by means of level-sets

To describe the location and geometry of cracks without being bound to the FE mesh, the level-set method is highly used. It was introduced by Osher and Sethian (1988) and is an efficient numerical technique to track moving interfaces. The implementation in the framework of XFEM (Moës et al., 2002; Gravouil et al., 2002) allows the allocation of enrichment functions to nodes based on the crack location. The discontinuity is described by two almost-orthogonal signed distance functions, which can be defined by nodal values.

The first level set $\phi(\mathbf{x})$ defines the crack surface and is given by

$$\phi(\mathbf{x}) = (\mathbf{x} - \mathbf{x}_c) \cdot \mathbf{n}, \quad (17)$$

with \mathbf{x}_c being a point on the crack surface. This function describes the shortest distance of any point \mathbf{x} to the extension of the crack surface. This definition would be sufficient to describe material interfaces and cracks, which completely cut an FE element. To describe the crack surface of arbitrary cracks, a second level set $\psi(\mathbf{x})$ is used, which is approximately orthogonal to $\phi(\mathbf{x})$ so that the crack geometry can be described by a combination of the two signed distance functions, where

$$\phi(\mathbf{x}) = 0 \quad \wedge \quad \phi(\mathbf{x}) < 0 \quad \text{defines the crack surface,} \quad (18)$$

$$\phi(\mathbf{x}) = 0 \quad \wedge \quad \phi(\mathbf{x}) = 0 \quad \text{gives the crack front and} \quad (19)$$

$$\phi(\mathbf{x}) = 0 \quad \wedge \quad \phi(\mathbf{x}) > 0 \quad \text{does not intersect the crack.} \quad (20)$$

Figure 2 shows a representation of the two level set functions defining a crack, where \mathbf{n}^+ indicates the positive normal to the crack surface and \mathbf{m}^+ to the crack front, respectively, for example the normal vector of the crack surface can now be determined by using the normalized gradient of the ϕ level-set at $\phi = 0$:

$$\mathbf{n} = \frac{\nabla \phi}{\|\nabla \phi\|} \quad \forall \mathbf{x} \mid \phi(\mathbf{x}) = 0. \quad (21)$$

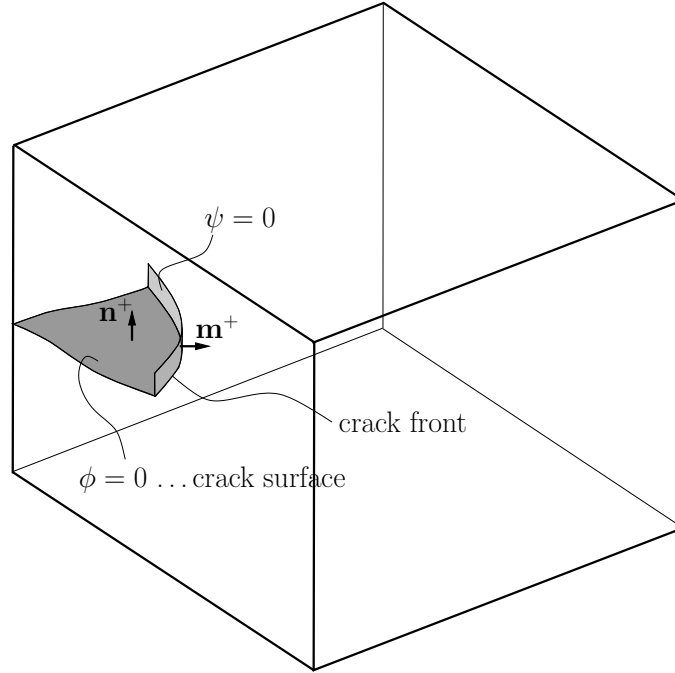


Figure 2: Representation of the two iso-zero level sets ϕ and ψ defining the crack geometry and location.

To describe the boundaries of interfaces in the framework of the FEM, the level set values ϕ_i and ψ_i are stored at the element nodes and by using the FE interpolation functions the level sets ϕ and ψ can be determined at any point \mathbf{x} :

$$\phi \approx \sum_{i=1}^{NN} N_i \phi_i \quad (22)$$

$$\psi \approx \sum_{i=1}^{NN} N_i \psi_i. \quad (23)$$

Nodal enrichment functions

The implementation of the partition of unity into the XFEM with arbitrary functions $G(\mathbf{x})$ was shown in Equation 16. In the following nodal enrichment functions for material interfaces and cracks will be presented.

Weak discontinuities

A weak discontinuity, e.g. caused by a material interface, causes a kink in the solution, i.e. a jump in the gradient. To model this influence Sukumar et al. (2001) introduced the absolute value function as the enrichment function by taking the absolute value of

the level set function ϕ

$$G_j(\mathbf{x}) = |\phi(\mathbf{x})| = \left| \sum_{i=1}^{NN} N_i \phi_i \right|. \quad (24)$$

As this type of functions leads to problems in blending elements, which are elements between the fully enriched domain and elements within the standard FE domain and thus elements with only some of their nodes being enriched, either smoothing or other strategies have to be applied to elements not including the interface (e.g. see Fries and Belytschko (2010)) or the modified absolute value enrichment function introduced by Moës et al. (2003) can be used

$$G_j(\mathbf{x}) = \sum_{i=1}^{NN} N_i |\phi_i| - \left| \sum_{i=1}^{NN} N_i \phi_i \right|. \quad (25)$$

This enrichment function has a value of zero for the elements, which are not crossed by the interface, and describes a ridge centered on the interface.

Strong discontinuities

This type of discontinuity refers to a jump in the solution, i.e. a jump in the displacement field and is used for the enrichment of elements, which are entirely cut by a crack. Typical choices for enrichment functions in this case are the sign function

$$G_j(\mathbf{x}) = \text{sign}(\phi(\mathbf{x})) = \begin{cases} -1 & : \phi(\mathbf{x}) < 0 \\ 0 & : \phi(\mathbf{x}) = 0 \\ 1 & : \phi(\mathbf{x}) > 0 \end{cases} \quad (26)$$

and the Heaviside function

$$G_j(\mathbf{x}) = H(\phi(\mathbf{x})) = \begin{cases} 0 & : \phi(\mathbf{x}) \leq 0 \\ 1 & : \phi(\mathbf{x}) > 0 \end{cases}, \quad (27)$$

leading to identical results as they span the same approximation space. In addition, both functions are unproblematic with regard to element blending as they are constant in the blending elements. Further, Moës et al. (1999) introduced a modified Heaviside function, which is also used for the XFEM implementation in Abaqus:

$$G_j(\mathbf{x}) = H(\phi(\mathbf{x})) = \begin{cases} -1 & : \phi(\mathbf{x}) < 0 \\ 1 & : \phi(\mathbf{x}) \geq 0 \end{cases}. \quad (28)$$

Singularities

For elements, which are not entirely cut by a crack, but contain the crack front, enrichment functions with singular derivatives must be used. For this case Belytschko and Black (1999) adopted the analytical solution for a straight crack obtained by means of

linear fracture mechanics to derive the often used four enrichment functions describing the crack tip displacement field:

$$G_1(r, \theta) = \sqrt{r} \sin\left(\frac{\theta}{2}\right) \quad (29)$$

$$G_2(r, \theta) = \sqrt{r} \sin\left(\frac{\theta}{2}\right) \sin(\theta) \quad (30)$$

$$G_3(r, \theta) = \sqrt{r} \cos\left(\frac{\theta}{2}\right) \quad (31)$$

$$G_4(r, \theta) = \sqrt{r} \cos\left(\frac{\theta}{2}\right) \sin(\theta) \quad (32)$$

with r and θ describing a local polar coordinate system at the crack tip, where $\theta = 0$ is the tangent at the crack tip. These polar coordinates can also be expressed in terms of the level set functions

$$r = \sqrt{\phi^2 + \psi^2} \quad , \quad \theta = \arctan\left(\frac{\phi}{\psi}\right) \quad (33)$$

In Abaqus, crack tip functions can only be used for stationary cracks.

Enrichment concepts

Figure 3 shows two common enrichment concepts used in the XFEM, which incorporate the presented enrichment functions.

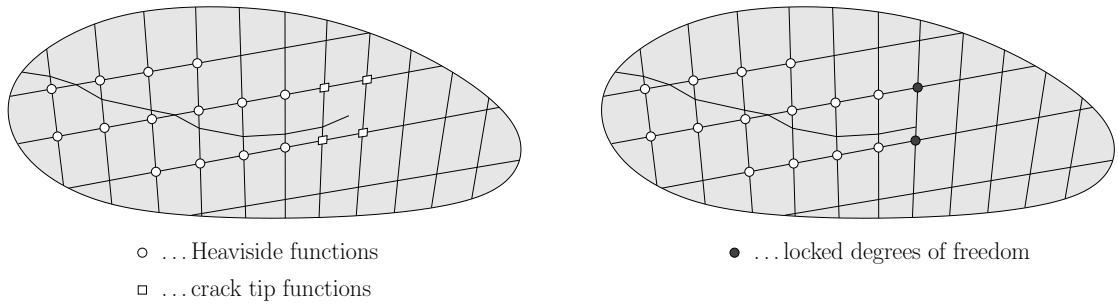


Figure 3: Enriched nodes for a domain with a crack: on the left by using crack tip functions and on the right with elementwise crack propagation

The so-called support of a node is the sum of all elements sharing this node. Nodes, whose support is fully cut by the crack, are enriched with the modified Heaviside function (see empty circled nodes in both sketches of Figure 3). If the crack ends within an element, its corresponding nodes are enriched with crack tip functions (squared nodes in Figure 3, left). This is the minimum version of enriching nodes, as in general the size of

the enriched subdomain can be chosen arbitrarily, but it has to be ensured that no linear dependencies between the enriched functions and the standard FE shape functions exist.

Abaqus uses a simplified version for modeling moving cracks. As depicted on the right of Figure 3, the crack moves elementwise and always ends on the border of an element. Thus, in these points (on the border where the crack ends), the crack opening must be zero and the corresponding degrees of freedom of these nodes must be locked (see full circles in Figure 3, right). Although the latter concept causes limitations in the crack propagation, like a dependency on the FE mesh, it has been successfully used before due to its simplicity (e.g. Wells and Sluys (2001)).

Phantom node method

Song et al. (2006) developed a convenient and efficient implementation of XFEM into the FEM framework based on an approach by Hansbo and Hansbo (2004). There so-called phantom nodes are superimposed on the original nodes. For elements not containing a crack, these phantom nodes are completely tied to the corresponding original nodes. If the element is cracked, it is then represented by two superimposed elements with a combination of phantom and original nodes, which are no longer constrained to each other.

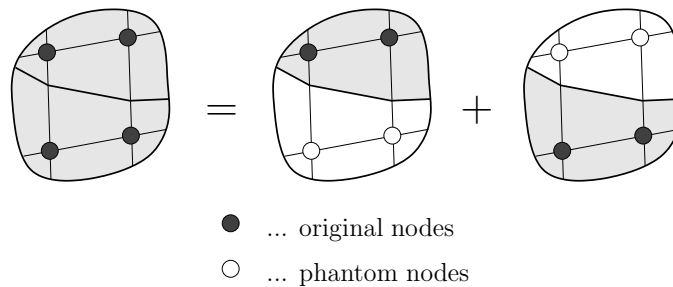


Figure 4: Principle of the phantom node method: example of superposition of two elements with two original and two phantom nodes each.

Figure 4 shows the principle of the phantom node method, where the behavior of a fully cracked element with four nodes is simulated by the superposition of two elements with two original and two phantom nodes each (filled circles denote original nodes and empty ones the phantom nodes, respectively).

In Figure 5 the comparison of the standard XFEM description and the phantom node method is represented, where it can be seen that in the latter the jump in the displacement field is realized by only integrating over the region from the side of the real nodes (solid nodes) up to the crack ($X = a$).

This approach, which is also used within Abaqus, has been successfully used for several simulations of crack propagation in Song et al. (2006) with only little mesh dependency. They also noted that, although the crack speed might be overestimated by the element-by-element propagation of a crack, its propagation path is usually in a

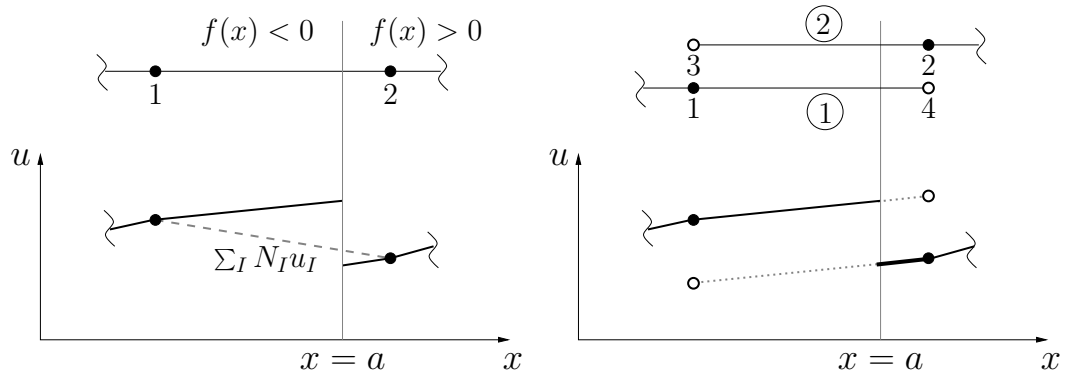


Figure 5: Comparison of a crack in the the standard XFEM (a) and in the phantom node method (b) for a 1D model (solid circles denote real and empty ones phantom nodes, respectively) (Song et al., 2006).

reasonable agreement with experiments. Further, Rabczuk et al. (2008) expanded the phantom node method to include crack tip enrichment functions into new element types.

Cohesive behavior

The behavior of the crack surfaces within cracked elements can be described by the same methods as the ones used for cohesive elements, which were presented before. This means that stresses can still be transferred through a cracked element until the defined damage evolution criterion is reached.

In Abaqus this behavior is implemented by using a traction-separation law with no coupling of the normal and tangential stiffness components:

$$\mathbf{t} = \begin{Bmatrix} t_n \\ t_s \\ t_t \end{Bmatrix} = \begin{bmatrix} K_{nn} & 0 & 0 \\ 0 & K_{ss} & 0 \\ 0 & 0 & K_{tt} \end{bmatrix} \begin{Bmatrix} \delta_n \\ \delta_s \\ \delta_t \end{Bmatrix} = \mathbf{K} \delta, \quad (34)$$

and the elastic terms K_{nn} , K_{ss} and K_{tt} are calculated based on the elastic properties for an enriched element and do not have to be specified individually.

Research Objectives and Outline of the Thesis

The research objectives of this thesis are outlined in the following. They are addressed in terms of the objectives of the four publications, of which this thesis is composed.

Publication 1 is dedicated to the development of a physically based approach to identify structural failure for wooden boards with knots, and its implementation into a numerical simulation tool. As knots and the resulting fiber deviations in their vicinities are mainly responsible for the reduction of effective stiffness and strength within wooden boards on a structural scale, the focus lies on the estimation of effective strength values by examining the qualitative stress changes in predefined volumes. This follows the assumption of the formation of failure zones with following stress redistribution, predominantly caused by perpendicular-to-grain tension in the vicinity of knots. The used numerical simulation tool is able to consider a realistic three-dimensional fiber course in the vicinity of knots and also accounts for density and moisture dependent strength and stiffness properties. The validation of the numerical simulation tool is carried out by a comprehensive test series of tensile and four-point bending tests.

In **Publication 2** the performance of the previously developed numerical simulation tool for wooden boards with knots is assessed by means of full-field deformation measurements. For this purpose, first, the suitability of full-field deformation measurements, using the digital image correlation (DIC) technique, for four-point bending tests on wooden boards with knots is evaluated. The investigation covers the experimental setup, choice and assessment of parameters within the evaluation software and discussion of local phenomena, with a special focus on the strain course in regions influenced by the presence of knots and fiber deviations. Next, the test series is used to validate the numerical simulation tool with regard to the influence of knots. Strain fields from the simulations are compared to the DIC measurement results and evaluated by means of contour plots of principal strains, strain distributions along vertical and horizontal sections and analyses of position and magnitude of peaks of relevant strain distributions. Additionally, the comparison of maximum principal strain directions is analyzed in detail to verify the efficiency of the used mathematical description for the fiber course used in the numerical simulation tool.

Publication 3 deals with the description of failure mechanisms at the wood cell level. For the development of a failure criterion at the clear wood level, which is able to describe the brittle failure mechanisms under tensile and shear loading, first, the initiation and the global direction of cracks at the cell level must be investigated, as structural features on the wooden microscale highly govern the macroscopic failure mechanisms. Thus, models of two repetitive units (unit cells) are used to identify all possible failure mechanisms within the two well-known layers in wood, late- and earlywood, by an approach based on XFEM. Samples of 800 load combinations are created and applied to the two cell types, individually, in highly nonlinear numerical simulations. The obtained failure modes are classified and global crack directions are assigned, enabling the determination of two multisurface failure criteria for the two cell types. The implementation of mentioned failure criteria is used to simulate the cracking behavior of wood models at

the annual year ring scale. The results of the simulations of uniaxial tensile tests under various fiber to loading orientations are compared to experiments.

In **Publications 4** so-called indicating properties (IPs), which are used for the assessment of strength properties within the grading process of wooden boards, are examined. For this purpose, the tensile and edgewise bending strengths of previously conducted experiments are determined. The tested boards are geometrically reconstructed by both manual and automatic reconstruction algorithms, whereas also improvements to the applied techniques are discussed to account for future developments in the wood grading industry. The now available 3D knot information is used to evaluate common IPs based on their efficiency to estimate effective strength properties, and is then used to modify and extend them to novel IPs, which allow the consideration of the knot location information. The statistical evaluation of combinations of the new indicating properties is presented and selected combinations are discussed in detail.

Contribution by the author

This thesis consists of four publications in peer-reviewed scientific journals. The author's contributions to the respective publications are as follows:

- **Publication 1:** *Numerical simulation tool for wooden boards with a physically based approach to identify structural failure (Lukacevic and Füssl, 2014):* The author greatly contributed to the development and worked out the concept of the structural failure criterion, performed a part of the mechanical tests, all of the experimental validation, and prepared most of the manuscript.
- **Publication 2:** *Performance assessment of a numerical simulation tool for wooden boards with knots by means of full-field deformation measurements (Lukacevic et al., 2014a):* The author performed a part of the mechanical tests, all data analysis and prepared most of the manuscript.
- **Publication 3:** *Failure mechanisms of clear wood identified at wood cell level by an approach based on the extended finite element method (Lukacevic et al., 2014b):* The author greatly contributed to the development of the multiscale damage approach, performed most of the model development, all data analysis, and prepared most of the manuscript.
- **Publication 4:** *Discussion of common and introduction of new indicating properties for the strength grading of wooden boards (Lukacevic et al., 2014c):* The author performed a part of the mechanical tests, all data analysis, proposed the developed novel indicating properties, and prepared most of the manuscript.

Chapter 1

Numerical simulation tool for wooden boards with a physically based approach to identify structural failure (Lukacevic and Füssl, 2014)

Authored by Markus Lukacevic and Josef Füssl

Published in *European Journal of Wood and Wood Products*, 72(4):497–508, 2014

Knots and the resulting fiber deviations are the main influence parameters of the effective stiffness and strength behavior of wooden boards on the structural scale. Depending on the size, shape and arrangement of knots/knot groups, certain effective mechanical properties can remain unaffected or change significantly. For this reason, a reliable prediction of the mechanical behavior of wooden boards is a basic requirement for efficiently designed wood products and timber structures. Within this work, a Finite-Element simulation tool was developed, which is able to consider a realistic three-dimensional fiber course in the vicinity of knots and also accounts for density and moisture dependent strength and stiffness properties. The estimation of effective strength values within this tool is done by examining the qualitative stress changes in predefined volumes, and is based on the formation of failure zones predominantly caused by perpendicular-to-grain tension in the vicinity of knots. Comprehensive test series, comprising tensile and four-point bending tests were carried out and used for validation. In general, a very good correlation between numerical and experimental results was obtained.

1.1 Introduction

The increasing use of wood and wood composites in engineering structures and, at the same time, lumber shortage in many areas of Europe forces a better utilization and a more efficient use of this building material. Gaining knowledge of the complex mechanical behavior of timber is therefore in the focus of current wood research. As is well-known, knots and the resulting fiber deviations in their vicinities strongly influence the mechanical behavior and are mainly responsible for qualitative downgrading of timber elements (Johansson, 2003). Within a grading process, sections which contain critical knots are cut out, and the remaining logs are categorized. Thereby, common grading techniques, like visual inspection or empirical correlations between effective properties and knot areas on log surfaces, are not able to take the effects of the anatomy of a knot and its resulting fiber deviations on the strength and stiffness of wooden boards appropriately into account. This means that, the full mechanical potential of wooden boards is not exploited yet and a much higher degree of utilization could be reached with better grading criteria. For this reason, mechanical tools for a reliable determination of effective strength and stiffness properties of timber elements are required, on which basis current grading criteria can be evaluated and new criteria may be developed.

In the past, various research studies examined the effect of knots on the mechanical properties of structural timber. Hatayama (1983) linked strength properties of wooden members to a fictive grain angle, which was obtained by measuring the fiber directions on the failure planes of tested strips and deriving empirical equations based on knot parameters, such as the knot diameter.

As not only the reduction of the cross-section by knots but also the resulting fiber deviations affect the strength of timber, various researchers investigated the fiber course around knots. The research of Goodman and Bodig (1978) and Phillips et al. (1981) resulted in the so-called *flow-grain analogy*, a mathematical formulation describing the two-dimensional fiber deviation around a single knot, based on the similarity of the fiber course pattern in the vicinity of knots and the fluid flow around an elliptic obstacle. The so found functions were used by Cramer and Goodman (1983) for further investigations of the influence of knot locations on stress concentrations and by Zandbergs and Smith (1988) for analyses of the fracture behavior in the vicinity of knots, respectively. Guindos and Guaita (2013) obtained the fiber direction for a three-dimensional Finite-Element approach by passing a laminar flow through the model and registering the velocity components in each element. The resulting velocity vectors were then used to define the local material orientation in a subsequent analysis, where the fluid elements are replaced by solid elements.

Another approach for a fiber orientation algorithm was presented by Mattheck (1997). Therein, it is assumed that the growth of a tree depends on its load history in such a manner that fibers are orientated in the direction of the maximum principal stress in any material point. Using an iterative method based on this algorithm, Resch and Kaliske (2005) determined the fiber course for three-dimensional problems by assuming a linear fiber course in global longitudinal direction and calculating the principal stresses caused by a uniaxial load by means of a Finite-Element simulation. The fibers are then

rotated into the direction of the maximum principal stress followed by the next iteration step, resulting in the fiber direction information for each finite element in compliance to Mattheck's theory.

Both approaches for the determination of the fiber course - *stress trajectories-based* and *fluid mechanical* - were compared by Lang and Kaliske (2013) using Finite-Element simulations. They concluded that both provide plausible results.

In most works only the fiber orientation in the global longitudinal-tangential (LT) plane was considered (Hatayama, 1983; Goodman and Bodig, 1978; Phillips et al., 1981; Cramer and Goodman, 1983; Zandbergs and Smith, 1988; Guindos and Guaita, 2013), whereas the fiber orientation in the radial direction, commonly noticed as dive angles in literature, is not considered explicitly. The research of Nagai et al. (2011) showed that tensile fracture was caused by the change of the fiber orientation in a three-dimensional manner in the vicinity of knots and that in such regions the fibers dive away from the pith. The algorithm for the determination of the fiber directions used in this work is based on the more realistic model of Foley (2003). Therein, it is assumed that all fibers, which are produced by a tree at the same time, are aligned along a so-called growth surface S , a curved plane in the three-dimensional space with theoretically zero thickness, which is not identical to the LT-plane. The flow-grain analogy is used to describe fiber deviations in the vicinity of knots in the LT-plane, and in addition the fiber deviations in the *out-of-plane* direction are obtained by fitting polynomial functions to growth ring patterns visible in the LR-planes.

The complex material behavior of wood together with the knot-triggered three-dimensional nature of the fiber course, makes the determination of global failure of a timber element through Finite-Element simulations a challenging task. In bending or tensile tests, failure is almost exclusively caused by knots (Johansson, 2003). Thus, it is obvious to investigate the regions in the vicinity of knots in more detail. As knots cause very localized stress and strain concentrations, traditional maximum stress failure criteria, evaluated at integration point level, cannot be simply related to structural failure, because the load carrying capacity of timber members would be vastly underestimated. For this reason, either cracking and softening effects have to be modeled or average stress states of selected areas may be accordingly evaluated, which leads to so-called *mean stress approaches*. These were first proposed by Masuda (1988) and Landelius (1989). The former assumed in his *Finite Small Area Theory* that fracture occurs when averaged stresses in a finite small area reach an ordinary criterion, whereas it was shown that the optimum size of such an area (1–2 mm by 0.4 mm) is related to the typical wood fiber structure. The latter used a similar approach in his *Finite Area Method*, in which he estimated the length x_0 of the finite area by comparing the resulting strength values to common linear elastic fracture mechanics (LEFM) approaches but only considering mode I fracture mechanisms. Aicher et al. (2002) extended this approach to also take into account the mode II fracture mechanisms with a mixed mode stress criterion to obtain the length x_0 in terms of energy parameters. Serrano and Gustafsson (2006), Sjödin and Serrano (2008) and Sjödin et al. (2008) used such a method, based on linear elastic fracture mechanics, to evaluate the mean stresses acting across an area, whose size is governed by the fracture properties of the material, for the investigation of single

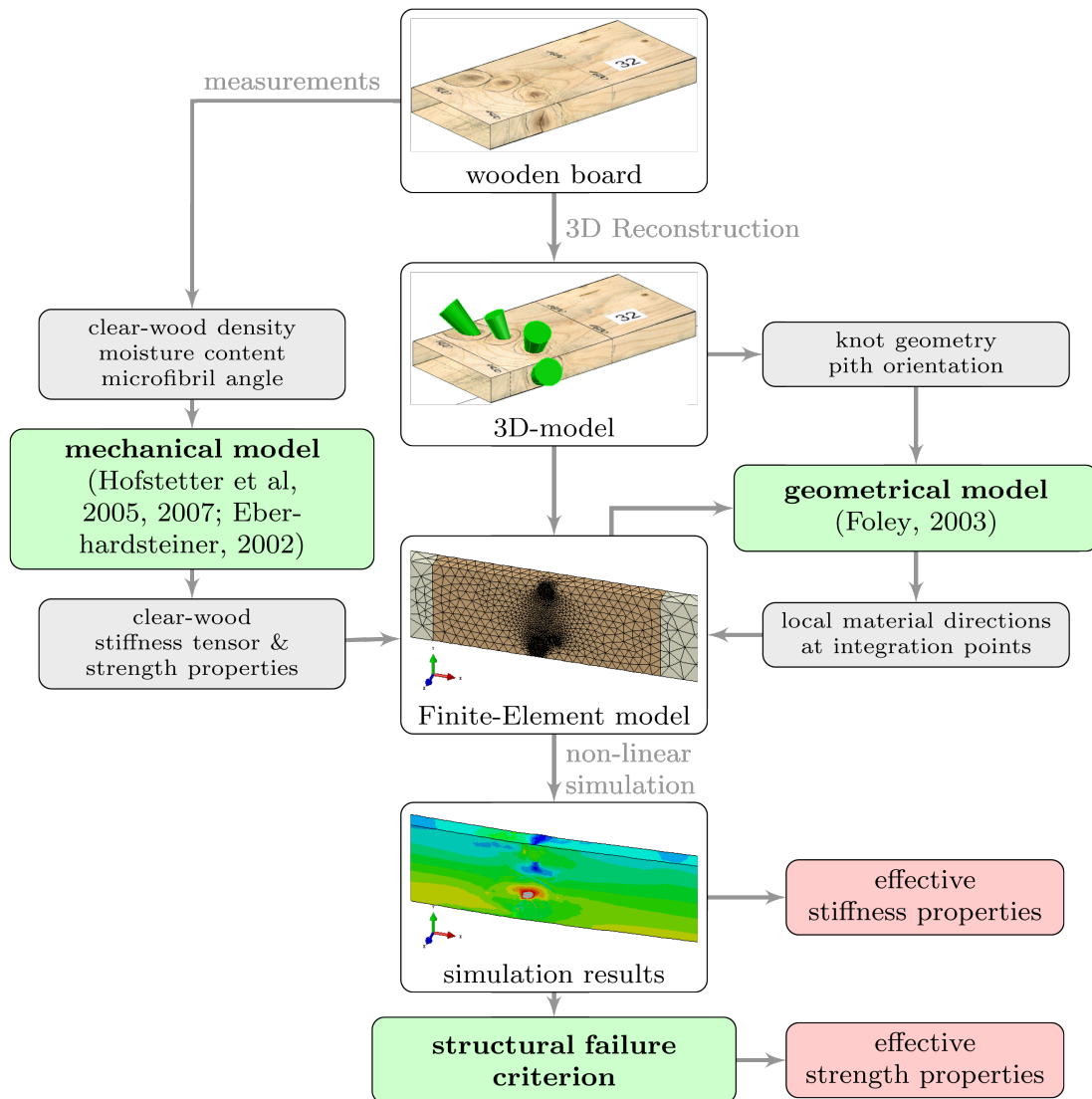


Figure 1.1: Concept of the numerical simulation tool for timber elements.

and multiple dowel connections. Guindos (2011) compared the efficiency of different volume definitions (size and shape), by averaging the stresses in these volumes and applying various failure criteria. Sandhaas et al. (2012) developed a three-dimensional material model for wood based on continuum damage mechanics and implemented it into a Finite-Element framework. In this nonlinear elastic approach the stiffness matrix is modified iteratively according to piecewise defined failure surfaces. Dias et al. (2007, 2010) presented a nonlinear Finite-Element model for the prediction of the mechanical behavior of timber-concrete joints, in which they used orthotropic yield criteria and several types of stress-strain behaviors, up to a tri-linear stress-strain curve with a yield drop.

Within this work, a three-dimensional numerical simulation tool for timber elements is proposed (Section 1.2), which is able to reliably determine effective stiffness and strength properties. The applied new physically-based structural failure criterion is described in Section 1.3. The validation of the model by means of comprehensive test series, comprising tensile and four-point bending tests, is discussed in Section 1.4. Finally, in Section 1.5 concluding remarks and a brief outlook on further developments are given.

1.2 Numerical simulation tool

The numerical simulation tool presented in the following enables the three-dimensional geometric reconstruction and the simulation of the mechanical behavior of wooden boards with knots. The main concept is based on the tool presented in Hackspiel (2010). Therein, `Comsol`, an extension for the commercial software `Matlab`, was used as Finite-Element code, while the tool presented in this work is built around the commercial Finite-Element software `Abaqus`. The simulation tool (basic concept illustrated in Figure 1.1) includes a geometrical model for the grain course and a micromechanical model for a density and moisture dependent characterization of the clear-wood material.

1.2.1 Geometrical model

This part of the simulation tool allows for the description of the three-dimensional fiber course in the vicinity of knots. For that, knots are modeled as rotationally symmetric cones with their apexes lying on a piecewise linear pith. Moreover, it is assumed that the cones and the surrounding block are perfectly connected. The fiber deviation region around a knot is defined by a cone with the same apex and axis as the cone representing the knot itself, but with the fourfold apex angle. In this region in each integration point the principal material directions are determined by an algorithm based on the model proposed by Foley (2003). This algorithm not only allows the consideration of the two-dimensional fiber deviation around a knot in the LT-plane but also includes the dive angle in the R-direction, resulting in a fiber direction vector, which reads as

$$\mathbf{df} = \mathbf{ds} + \mathbf{dr},$$

$$\text{with } \mathbf{ds} = \{0 \ \Delta t \ \Delta l\}^T \text{ and } \mathbf{dr} = \{\Delta r \ 0 \ 0\}^T. \quad (1.1)$$

It is assumed that there exists an analogy between the abovementioned two-dimensional fiber course in the vicinity of a knot in the LT-plane and the flow of a fluid around an elliptic obstacle (see Figure 1.3(a)). Thus, subvector \mathbf{ds} of the fiber direction vector \mathbf{df} can be calculated in each integration point. According to Shigo's knot formation theory (Shigo, 1990), fibers show different patterns of growth around the knot in different growth periods. Within this work, only fiber course according to the radial grain deviations later in the growth season (beta layer), has been considered. It is assumed that

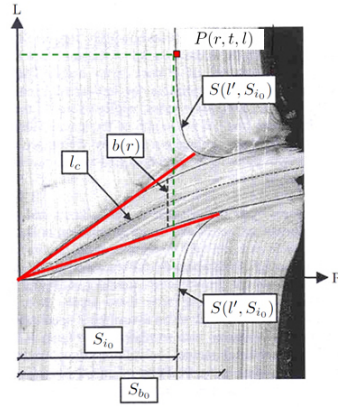


Figure 1.2: LR -plane with growth surface S for an arbitrary point $P(r, t, l)$ together with idealized knot boundaries (red lines) (Foley, 2003).

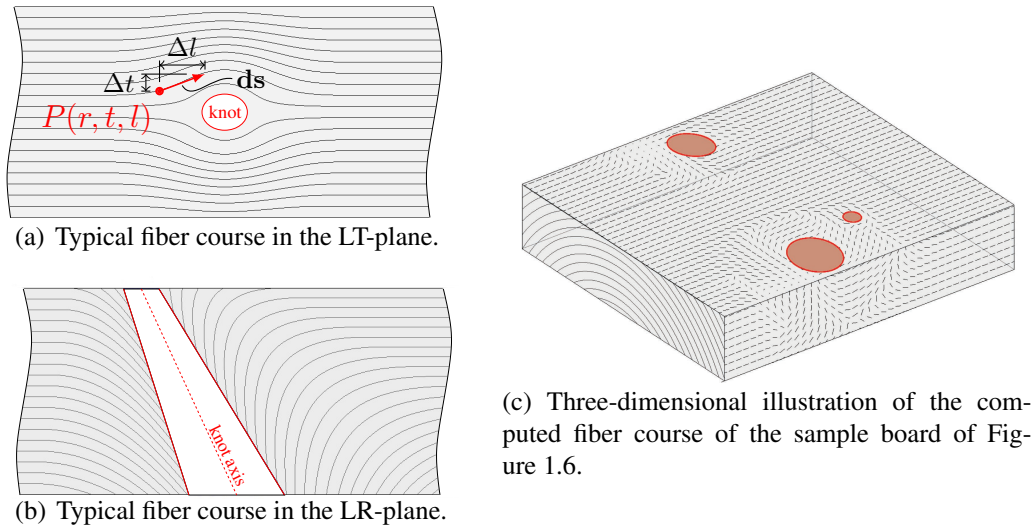


Figure 1.3: Typical fiber courses in the vicinity of knots.

the fibers are oriented within the growth surface S , and that subvector \mathbf{dr} in (1.1) is the projection of \mathbf{df} on the normal vector of the LT -plane (see Figure 1.2). Thus, the third dimension of the fiber direction vector for a point $P(r, t, l)$, the so-called dive angle, is obtained by using the following polynomial function for the growth surface

$$S(p, S_{i0}) = S_{i0} + A_{bump} \cdot S_{i0}^{A_{exp}} \cdot p^{-B_{bump}} . \quad (1.2)$$

Within this work, constant values were used for the empirical parameters A_{bump} , A_{exp} and B_{bump} , as all specimens were obtained from the same wood species and the small differences in the out-of-plane fiber deviations within this species would not justify further distinctions.

In each integration point the according fiber direction vector is calculated for each knot individually. In sections with knot clusters it is very likely that the global fiber direction is influenced by multiple adjacent knots. Thus, for integration points lying in

multiple overlapping fiber deviation cones the fiber direction vector df is obtained by calculating a distance-weight average (Lukacevic, 2009). The fiber direction in undisturbed clear-wood regions (not in the vicinity of a knot) only depends on the orientation of the pith and is maybe influenced by spiral grain. In the knots themselves, the local longitudinal fiber orientation is defined to be parallel to the direction vector of the corresponding knot cone axis.

1.2.2 Mechanical model

The orthotropic clear-wood material properties with respect to the principal material directions are determined by means of a micromechanical model developed by Hofstetter et al. (2005, 2007). It allows the calculation of the stiffness tensor from a few universal nanoscaled constituents and from microstructural properties, such as clear-wood density, moisture content, microfibril angle and volume fractions of hemicellulose, cellulose, lignin, and water. Thus, by varying the microstructural input parameters, the simulation tool can be applied to any wood species and sample, taking into account the large variability of stiffness properties. For the validation of the model in section 1.4, with the exception of clear-wood density and moisture content the micromechanical parameters of Table 1.1 were used for all samples as all of them were prepared of the same wood species. For the knots, transversal isotropic material behavior is assumed, whereas for the determination of the stiffness tensor the same chemical constituents as for the clear-wood sections was used with a 2.5 times higher density. This assumption was necessary to account for the well-known higher stiffness of knots and the lack of literature about the exact microstructural and mechanical properties of the knot tissue.

Table 1.1: Microstructural input parameters used in the micromechanical model of Hofstetter et al. (2005, 2007) for the prediction of the orthotropic stiffness tensor.

constituent	cellulose	hemi-cellulose	lignin	extractives
weight fraction [%]	43.5	27.7	23.6	5.0

The failure criterion of Tsai and Wu for orthotropic materials with different strengths in tension and compression is used to define local failure at the integration point level with perfect plastic behavior, using an associated flow rule. The failure criterion reads as

$$\begin{aligned}
 f(\boldsymbol{\sigma}) = & a_{LL}\sigma_{LL} + a_{RR}\sigma_{RR} + a_{TT}\sigma_{TT} + \\
 & b_{LLLL}\sigma_{LL}^2 + b_{RRRR}\sigma_{RR}^2 + b_{TTTT}\sigma_{TT}^2 + \\
 & 2b_{LLRR}\sigma_{LL}\sigma_{RR} + 2b_{RRTT}\sigma_{RR}\sigma_{TT} + \\
 & 2b_{TTLL}\sigma_{TT}\sigma_{LL} + 4b_{LRLR}\tau_{LR}^2 + \\
 & 4b_{RTRT}\tau_{RT}^2 + 4b_{TLTL}\tau_{TL}^2 \leq 1,
 \end{aligned} \tag{1.3}$$

where the twelve independent tensor components (a_{ij} , b_{ijkl}) of (3.13) are estimated according to Eberhardsteiner (2002) and Kollmann (1982), considering the actual clear-wood densities (see Table 1.2 for exemplary values). The material model of wood for the three-dimensional stress space was implemented into a user-subroutine (UMAT) of the commercial Finite-Element software *Abaqus* by Dorn et al. (2013).

Table 1.2: Overview of the Tsai-Wu tensor components for a clear-wood density of 400 kg/m^3 .

a_{LL}	a_{RR}	a_{TT}	b_{LLLL}	b_{RRRR}	b_{TTTT}
-0.00527	0.0585	0.0578	0.00023	0.0282	0.0276
b_{LLRR}	b_{RRTT}	b_{TTLL}	b_{LRLR}	b_{RTRT}	b_{TLTL}
0.00024	0.0	0.00024	0.00295	0.0254	0.00295

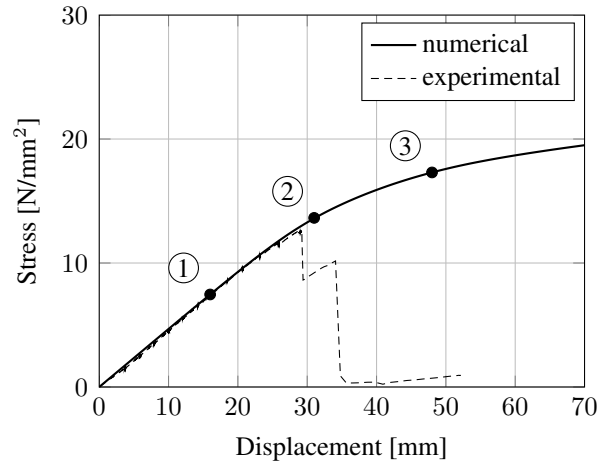


Figure 1.4: Stress-displacement curve (maximum effective bending stress in the area of the maximum moment as a function of the displacement at the load application point; the marked points indicate stress states, discussed in detail in Section 1.3 and Figure 1.6).

1.2.3 Preliminary results

First simulations of a wooden board ($40.7 \times 182.0 \times 3000.0 \text{ mm}$) under four-point bending about the major axis showed that the elastic response can be reproduced correctly with the proposed tool, but the ultimate load is overestimated, if it is solely determined by using the Tsai-Wu criterion with an associated flow rule, as can be seen in Figure 1.4. Therein, the stress-displacement curves, obtained at the load application point, of a wooden board are illustrated, where the continuous line indicates the numerical simulation and the dashed line the corresponding experiment. For this reason, a structural (global) failure criterion is required, which is proposed in the following section.

1.3 Structural failure criterion

Structural failure of wooden boards is characterized by brittle failure modes, unstable crack growth and different failure mechanisms triggered by a complex three-dimensional fiber course. An exact reproduction of all these effects with a numerical simulation tool is a challenging task and, at least, not suitable for a stable evaluation of several samples. For this reason, different strategies have been developed to identify structural failure, as mentioned in Section 2.1. The approach, presented in the following, is based on the same idea as the abovementioned *mean stress approaches* (Landelius, 1989; Aicher et al., 2002; Masuda, 1988), meaning that the stress states of a defined observation area indicate cracking or global failure, respectively. In contrast to these methods, where an average stress state of a certain area or volume serves as failure indicator, in the presented work the qualitative change of stress states within a volume is supposed to signal global failure. Moreover, the considered volumes are chosen depending on structural realities. The concept behind this and the used failure criterion are proposed in the following.

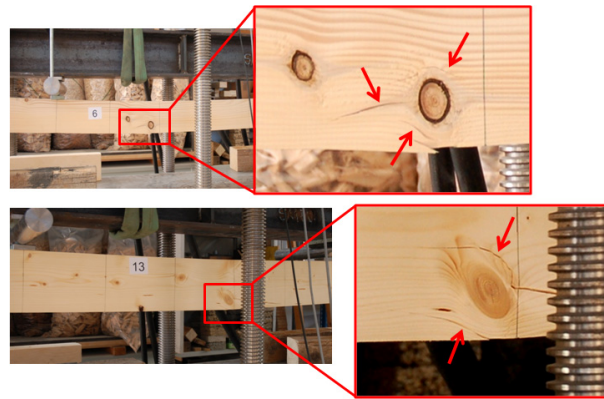
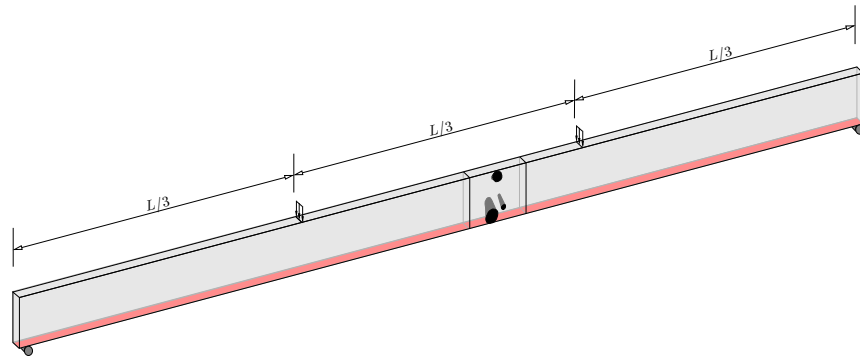


Figure 1.5: Start of cracking in two sample boards of the four-point bending test series.

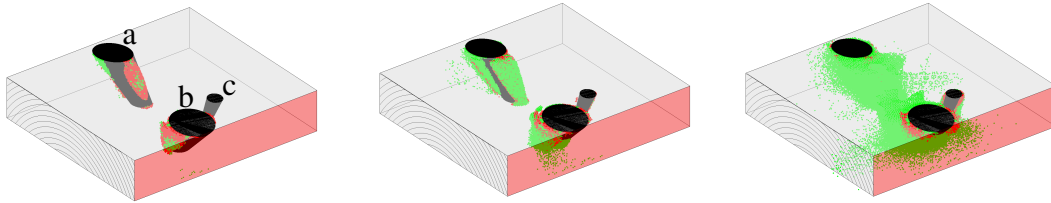
It is well known that the fracture toughness in planes with a surface normal in radial or tangential direction is almost one magnitude lower than of planes normal to the longitudinal direction (Schniewind and Centeno, 1973). Furthermore, the strength values perpendicular to the fiber direction are much lower than in fiber direction (Eberhardsteiner, 2002). For this reason and from experimental observations it can be shown that structural failure of timber is mainly characterized by brittle failure modes initiated in areas where perpendicular-to-grain tension stress states appear/dominate. This is the case either around knots (see Figure 1.5), due to strong fiber deviations, or at capped fibers at the surface of wooden boards. Within the presented numerical tool, start of structural failure is assessed by analyzing the stress states in the vicinity of each knot. Thus, the presented approach is not able to account for shear stress induced cracking far from the knot boundaries. Implementations of this failure mode are topic of future investigations of the simulation tool.

In Figure 1.6(a) the failure region of the same sample as in Figure 1.4 is illustrated, where the hatched surface identifies the tensile zone for bending about the ma-



(a) Failure region of the sample board (hatched surface identifies the tensile zone for bending about the major axis).

● predominant perpendicular-to-grain stress ● predominant normal stress in long. direction



(b) Time point ①: State prior to experimental failure (19.6%/0.2%).

(c) Time point ②: Fully failed interface zone (46.0%/14.4%).

(d) Time point ③: Development of global failure mode (41.1%/51.1%).

Figure 1.6: Evolution of failure modes around knots, illustrated by means of an exemplary wooden board from test series 4 (the percentages in the subfigures' captions refer to the knot failure volumes due to perpendicular-to-grain and longitudinal tension, respectively, for the crucial knot b).

major axis. Figure 1.6(b) shows a state prior to experimental failure (cf. time point ① in Figure 1.4), where the points indicate integration points reaching the Tsai-Wu failure criterion, which can be distinguished into points with failure predominantly due to perpendicular-to-grain tension and ones with failure predominantly due to tension in grain direction. It can be seen that failure starts at the interface zone between knots and surrounding wood material. Subsequently, the whole interface zone under perpendicular-to-grain tension reaches the failure criterion, as shown in Figure 1.6(c) (Time point ②). At this moment, stress redistribution from the perpendicular-to-grain to the longitudinal direction starts, and global failure modes develop (see Figure 1.6(d)) (Time point ③). The formation of abovementioned failure zones around the knots is now used to identify the begin of structural failure and in that way the effective strength of the wooden board. Therefore, for each cone, representing a knot, a so-called *failure cone* is defined, with the same apex as the original cone. The size of the failure cone, defined by the apex angle, is chosen so that the whole region in which perpendicular-to-grain stress develops around the knot is covered. A failure cone with $1.4d$ (as illustrated

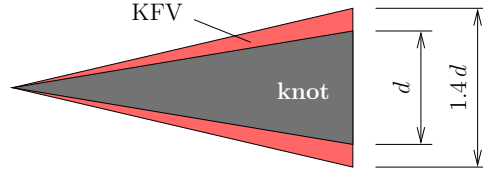


Figure 1.7: Considered region around knots: knot failure volume (KFV).

in Figure 1.7) was found to be sufficient in every case. Parameter studies of the failure cone size showed that larger cone apex angles lead to the same results but with higher computation cost (see Figure 1.8). If a stress state at an integration point in the *failure*

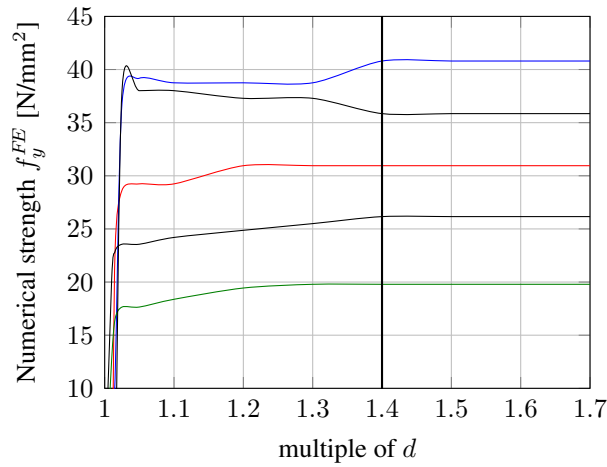


Figure 1.8: Development of the numerical strength as a function of the failure cone size for several sample boards.

cone reaches the Tsai-Wu failure criterion and its tensile stress components for the radial or tangential principal material directions reach a density dependent threshold f_{RT} ,

$$\sqrt{\sigma_{RR}^2 + \sigma_{TT}^2} \geq f_{RT}, \quad (1.4)$$

with f_{RT} being defined as one third of the mean strength in radial and tangential direction (see Figure 1.9), the corresponding volume of the integration point is added to the so-called *failure volume* of this cone.

Figure 1.10 shows the development of the *failure volumes* for each knot of above-mentioned bending test. If a failure volume due to perpendicular-to-grain tension around a knot starts decreasing, it is assumed that global stress redistribution takes place and structural failure occurs. This characteristic of the development of *failure volumes* could be observed for each tensile and bending test. In Figure 1.11 this distribution is shown for the critical knot of several tested samples, where the start of stress redistribution, and therefore global failure, is marked. All results in this section were exclusively obtained from numerical computations without the usage of any experimental measurements.

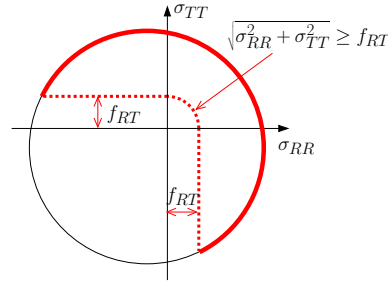


Figure 1.9: Transverse tensile stress threshold.

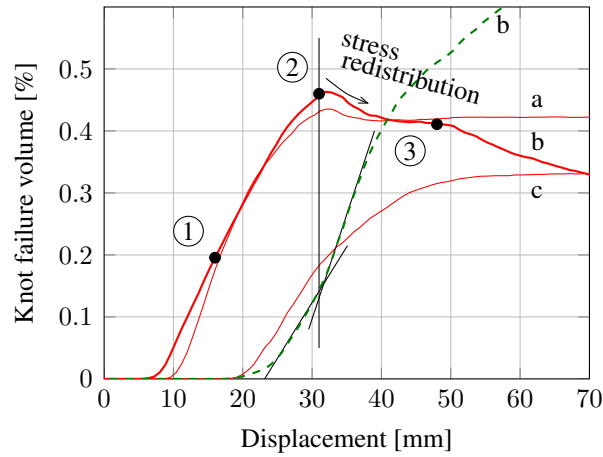


Figure 1.10: Development of *knot failure volumes* for three knots (solid lines indicate failure volumes reaching the Tsai-Wu failure criterion and the transverse tensile stress threshold according to Figure 1.9 and the dashed line the failure volume reaching only the former criterion; a, b and c refer to the labels in Figure 1.6(b)).

Thus, being able to identify structural failure as presented means that there is no need for “failure parameters”, which must be calibrated on the basis of experiments.

Finally, it should also be noted that for a knot-free board the numerical simulation tool predicts structural failure based on the Tsai-Wu criterion with perfect plastic behavior assigned to clear-wood regions. This leads to an effective failure stress which can also be specified analytically as

$$\sigma_{eff} = M_{pl}/W \text{ with} \tag{1.5}$$

$$M_{pl} = x \cdot h_1 \cdot b \cdot f_{ycL} . \tag{1.6}$$

In (1.6) h_1 is defined by $f_{ycL} \cdot h_1 = f_{ytL} \cdot h_2$ and $h = h_1 + h_2$, respectively, where h and b are the cross-sectional dimensions of the board, and f_{ycL} and f_{ytL} are the compressive and tensile clear-wood strength in longitudinal direction, respectively.

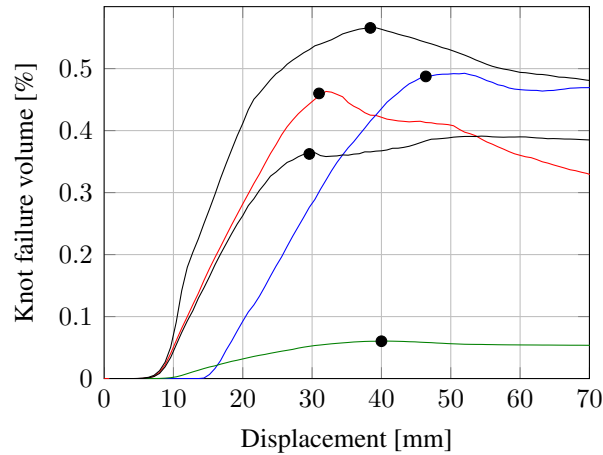


Figure 1.11: Development of decisive *knot failure volumes* for several sample boards (marked points are used to estimate structural failure).

1.4 Validation

The presented structural failure criterion was validated by means of tensile and bending tests of wooden boards with knots, which were manually reconstructed to obtain the exact knot geometries. The tests as well as the three-dimensional reconstruction and the corresponding Finite-Element simulations are described in detail in the following.

1.4.1 Materials and methods

All samples were prepared of Norway spruce (*Picea abies*). The first three test series were part of the stiffness validation of the numerical simulation tool for wood grading in Hackspiel (2010). The boards of test series 1 were loaded up to failure in uniaxial tensile tests in an Austrian wood processing company. All other experimental series consisted of four-point bending tests, based on DIN EN 408 (Timber structures - Structural timber and glued laminated timber - Determination of some physical and mechanical properties). An overview of the different test series is given in Table 1.3. The tests for the validation series 2 and 3 were performed at *Holzforschung Austria* (Vienna).

Table 1.3: Overview of the different test series used for model validation.

Series	# of tests	Cross-section [mm]	Length [mm]	Load case
1	12	80/40	500	tension
2	9	144/45	2592	bending (major axis)
3	6	189/45	3420	bending (major axis)
4	34	40/115,145,185	3000	bending (major axis)
5	32	115,145,185/40	1550	bending (minor axis)

Test series 4 and 5 were conducted at the laboratory of the Research Center of Building Materials, Material Technology and Fire Safety Science of the Vienna University of Technology (14 specimens) and at the Laboratory for Macroscopic Material Testing of the Institute for Mechanics of Materials and Structures (IMWS) of the Vienna University of Technology (52 specimens) and will be described in detail. The boards were taken from a wood trader and selected by taking certain points into account: knots should be situated in the center third and should especially be avoided under the load application points. This ensures the occurrence of significant knots in the area of the maximum moment (constant between the two load application points). Preferably, a single knot/knot group was situated in the tension zone of the board. Under these conditions explicit information about the influence of knots/knot groups (in combination with the fiber deviation in its vicinity) on the bending strength of the board could be gained. The width of all tested boards of test series 4 and 5 was 40 mm and the height varied between 115, 145 and 185 mm. For the tests at the IMWS a triaxial servo-hydraulic testing machine manufactured by Walter & Bai, with built-in load cells for a maximum load of 250 kN and 10 kN, respectively, an 0 to 110 mm encoder and computer assisted analysis, was used (see Figure 1.12).

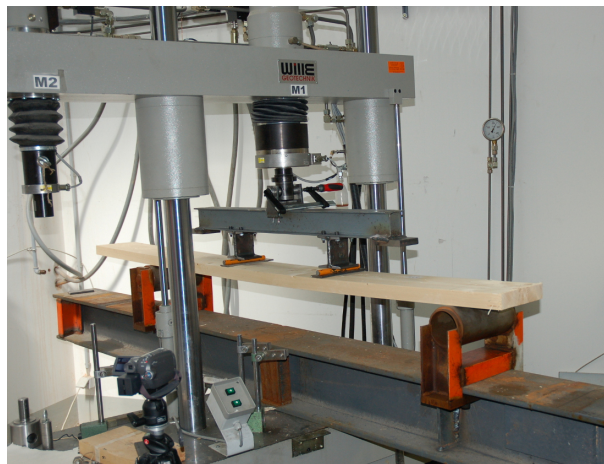


Figure 1.12: Experimental setup at the Laboratory for Macroscopic Material Testing.

The tests were performed displacement controlled, using the machine's 250 kN load cell. A steel girder distributed the load to the load application points. Small steel plates were situated on the specimen at the load application points and supports, in order to avoid local indentations. Steel cylinders, with a diameter of 10 mm, between girder and plate served as a roller-bearing, such that local constraints could be prevented. The load was applied with a constant rate of 20 mm/min and stopped as soon as the test specimen collapsed. For each test, a load-displacement curve up to failure (maximum load P_{max}) was recorded. Every single test was documented in detail with pictures and/or videos to provide an appropriate basis for the evaluation of the test results.

For all specimens, sample disks were cut out of clear-wood sections, i.e. sections with no knots and no fiber deviations caused by them. These disks were weighed, dried at 105°C and weighed again, to obtain the corresponding clear-wood densities ρ_{cw} and

the moisture content u for each board, which were used as input parameters for the micromechanical model.

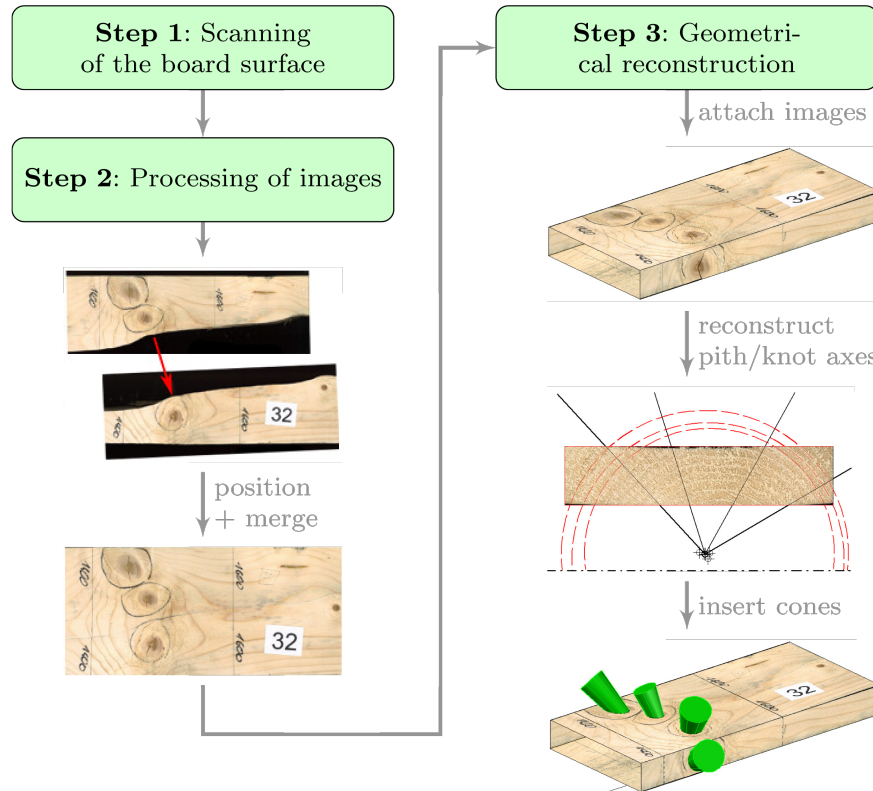


Figure 1.13: Flowchart illustrating the three-dimensional reconstruction process of the geometry of the tested boards.

Three-dimensional reconstruction of the test specimens

In order to provide a three-dimensional model of the specimens as a basis for the numerical simulations, the destructed test specimens had to be fully reconstructed on the computer. To allow a reasonable validation, the reconstruction should represent the real geometry as precisely as possible. Because of the insignificant influence of the sections between supports and load application points on the structural behavior, the reconstruction was limited to the area between the two load application points (area of maximum moment). The failure zone of every specimen had to be cut out and, if necessary, split into smaller pieces in order to enable scanning of the board surfaces. Due to the complexity of the material's structure, the following simplifications had to be accepted for the reconstruction:

- It is assumed that knots can be modeled as rotationally symmetric cones with their apexes lying on the pith,

- the pith itself is supposed to have a linear course and
- the stem is approximated by a circular cross-section.

The basic reconstruction process is shown in Fig. 1.13. First, the relevant parts of the specimen surface were digitized. After the images of the surface were edited, they were attached to a 3D-model of the board. In a last step, the locations of pith and knot axes were determined and the knots, approximated by rotationally symmetric cones, were inserted into the model.

Step 1: Scanning (digitalization) of the board surface

First, the specimens were cut into pieces to allow scanning with an A3 flatbed scanner. It was necessary to carefully mark and assort all members in order to ensure the distinct assignment of every single part to the corresponding test specimen. Scans were made of every board face and every member necessary to reconstruct the position and size of knots as well as the orientation of their axes. In addition, the cross section surface was scanned for the reconstruction of the pith location.

Step 2: Processing of the images

In a next step, the scans were edited by the use of an image editing program. After positioning and merging of the scans, the images were cropped such that only the board remained within the picture, like illustrated in Fig. 1.13. Result of the processing of the scans were at least three images of every specimen, one of the front side, the back side and one image of the cross-section. If necessary, additional images of the top and the bottom were made.

Step 3: Geometric reconstruction

The whole board with its exact dimensions was three-dimensionally reconstructed in AutoCAD, such that a 3D-model of the board's circumscribing cuboid was obtained. Next, the corresponding images were attached to the model and assembled in the correct position. The centers of the knots were marked and the boundaries of the knots were approximated by ellipses. The knot axes were determined by connecting the centers of each knot on two corresponding faces. The location of the pith was identified by approximating at least three growth rings with circles in the cross-section image. The pith location could be accurately determined through interpolation between the three different but fairly close centers of the constructed circles (see Fig. 1.13). Then, the knot axes were extended to the pith. Due to the assumption that the knots can be approximated as rotationally symmetric cones, the originally defined knot axes did usually not intersect the pith. In reality, the knot axis is slightly curved, thus, in most cases the reconstructed knot axis had to be marginally adjusted to assure that the apex lies on the pith. As soon as the definite location of the knot axis was defined, the rotationally symmetric cone representing the knot was inserted. The diameter of the cones were determined by the ellipses circumscribing the knot cross-section on each face of the board. The obtained 3D-models of the specimens comprise all relevant geometrical data needed as input for the numerical simulations.

1.4.2 Results

As mentioned in Section 1.4.1, the boards of test series 1 were subjected to tensile tests, whereas test series 2 to 4 consisted of four-point bending tests about the major axis. The comparison between the experimentally (f_y^{exp}) and numerically (f_y^{FE}) obtained effective strengths for these tests can be seen in Figure 1.14, and shows very good agreement.

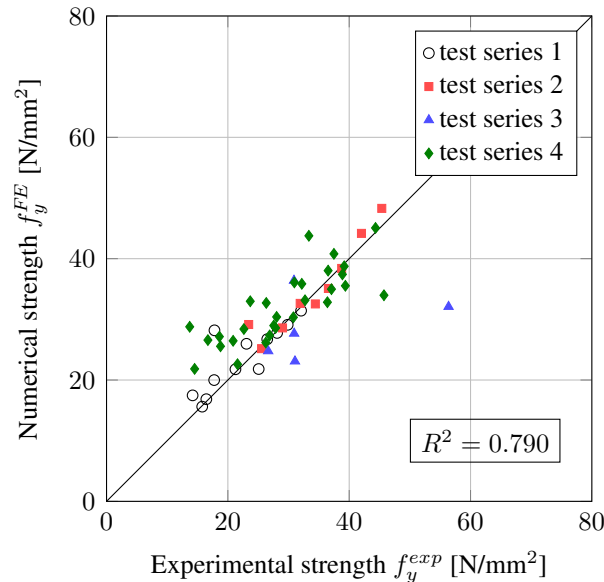


Figure 1.14: Comparison of experimentally and numerically obtained effective strengths (mean values and standard deviations of relative prediction errors: $9.07\% \pm 23.77\%$).

Horizontally tested specimens

The boards of test series 5 were subjected to four-point bending tests in a horizontal test configuration, i.e. bending about the minor axis. All tested boards had horizontal annual growth rings, i.e. the local tangential direction was parallel to the greater cross-sectional dimension. Additionally, the boards were arranged in such a manner that the worst case scenario relating to structural failure was tested, which is why always the bigger knot dimensions could be found at the bottom surface. This means that it is very likely that the knot axes are approximately facing in the same direction as the applied load. Due to the three-dimensional fiber deviations in the vicinity of knots, multiple fibers are cut at the tensile edge in a relatively large area, forming potential crack planes (cf. Figure 1.15). As can be seen in Figure 1.16 for two sample boards, this results in a very brittle failure mechanism, leading to an overestimation of the strength when using the presented structural failure criterion (see Figure 1.17).

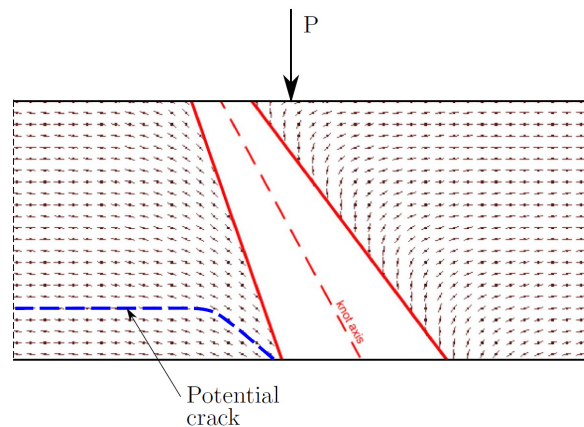


Figure 1.15: Assumed fiber course in the LR -plane approximated by the use of polynomial functions (board thickness=40 mm).



Figure 1.16: Bottom surfaces of two sample boards of test series 5.

1.5 Conclusion

A numerical simulation tool for the determination of the effective strength of wooden boards was proposed, which includes a new structural failure criterion based on the evaluation of stress states around knots. This tool allows the consideration of realistic three-dimensional fiber courses in the vicinity of knots, including the typical knot bump, and is also able to consider density and moisture content dependent strength and stiffness properties. For the validation of the model, comprehensive test series, comprising tensile and four-point bending tests, were carried out. Based on the results, the following conclusions can be drawn:

- The experimentally obtained bending strengths (about the major axis) as well as the tensile strengths agreed well with the results obtained with the numerical simulation tool. Therefore, the proposed structural failure criterion can be seen as an appropriate tool for a reliable and stable prediction of effective strength properties of timber elements.
- Under the assumption that global failure can be related to a stress transfer mechanism, which is clearly identifiable by evaluating stress fields in the vicinity of

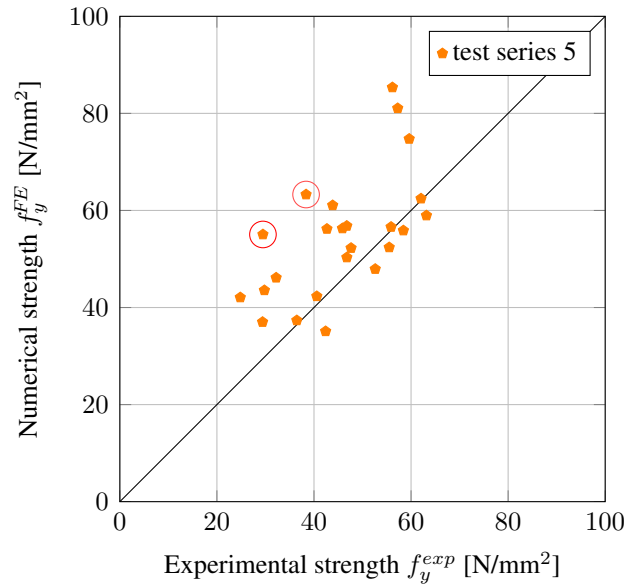


Figure 1.17: Comparison of experimentally and numerically obtained bending strengths for the horizontally tested boards of test series 5 (the specimens of Figure 1.16 are marked with red circles; mean values and standard deviations of relative prediction errors: $23.08\% \pm 36.42\%$).

knots, there is no need for empirical parameters. Meaning that no identification experiments are required to calibrate the structural failure criterion.

- Deficiencies of the failure criterion arise when the main failure mechanism is triggered by capped fibers in the tensile zone, as is the case for bending about the minor axis. Nevertheless, the trend of the effective strength distribution could be reproduced correctly. The consideration of this effect within this simulation tool is a current research focus at the IMWS.

In general, the combination of the Finite-Element method with a three-dimensional geometric model for the fiber course and a micromechanical model delivering reliable material properties, leads to a powerful simulation tool which is able to reliably predict the mechanical behavior of timber elements. For this reason, it could be used as basis for the evaluation and optimization of current grading criteria and design concepts. Furthermore, the model can easily be extended to study Cross-Laminated Timber or Glued Laminated Timber.

Performance assessment of a numerical simulation tool for wooden boards with knots by means of full-field deformation measurements (Lukacevic et al., 2014a)

Authored by Markus Lukacevic, Josef Füssl, Michael Griessner and Josef Eberhardsteiner

Published in *Strain*, DOI: 10.1111/str.12093, 2014

In wooden boards, knots and the resulting fiber deviations in their vicinities are mainly responsible for qualitative downgrading of timber elements. Thus, the development of reliable numerical simulation tools for the determination of effective strength and stiffness properties of timber elements and, in a next step, for the development and evaluation of grading criteria is highly desirable. Due to the complexity of such tools a comprehensive validation is required. Within this work, the suitability of full-field deformation measurements for four-point bending tests on wooden boards with knots is evaluated first. Next, the test series are used to validate a previously developed three-dimensional numerical simulation tool, which combines a geometrical model for the grain course and a micromechanical model for a density and moisture dependent characterization of the clear-wood material. The digital image correlation technique proved to be capable to reproduce the strain fields in the vicinity of knots under bending load. Moreover, a very good correlation between numerical and experimental results was obtained.

2.1 Introduction

The increasing use of wood and wood products in engineering structures and, at the same time, lumber shortage in many areas of Europe forces a better utilization and a more efficient use of this building material. This in turn drives the development of simulation tools, which contribute to a better understanding of the mechanical behavior of wood products and allow for a realistic performance review of them.

One of the main factors influencing the mechanical performance of timber elements are knots and the resulting fiber deviations (Johansson (2003)). This means that common grading techniques, which are based on single parameters and geometrical characteristics of wooden members, e.g. empirical correlations between effective properties and knot areas on specimen surfaces, are not able to take the effects of the anatomy of a knot and its resulting fiber deviations on the strength and stiffness of wooden boards appropriately into account. These approaches, therefore, lack in the acquisition of the rather complex relations in the material's structure, which mainly account for the mechanical behavior. Gaining knowledge of this complex mechanical behavior of timber is therefore in the focus of current wood research.

In the past, several researchers have developed Finite Element (FE) models to investigate the influence of knots on wooden boards. The work of Goodman and Bodig (1978) and Phillips et al. (1981) on the so-called *flow grain analogy*, which describes the two-dimensional fiber deviations in the vicinity of knots mathematically often served as basis for such models. Cramer and Goodman (1983) used this model for further investigations of the influence of knot locations on stress concentrations and Zandbergs and Smith (1988) for the analyses of the fracture behavior close to knots, respectively. Guindos and Guaita (2013) developed a FE model which allows the consideration of a three-dimensional fiber course in the vicinity of knots using a laminar flow model for the definition of the local material orientation. They validated their model by conducting four-point bending tests on nine beams and comparing the numerical results to photogrammetrically measured displacements of an average of 65 FE nodes. The FE model of Resch and Kaliske (2005) uses the approach for the fiber orientation of Mattheck (1997), which assumes that fibers are orientated in the direction of the maximum principal stress in any material point. Lang and Kaliske (2013) compared both approaches for the determination of the fiber course - *stress trajectories-based* and *fluid mechanical* - by means of FE simulations, leading to the conclusion that both provide plausible results.

All these models have in common that their validation is based almost exclusively on discrete measurements, whereas it could not be examined directly if strain fields are captured appropriately across larger regions. But especially for wooden boards with knots, which exhibit a highly inhomogeneous structure, this information would be necessary to gain understanding of the mechanical process within the material and to be able to usefully implement structural failure criteria or cracking algorithms in the FE model.

The application of non-contact optical methods for deformation analysis, such as the digital image correlation (DIC) technique, could allow for such an areal review of strain

fields and subsequently a comprehensive validation of FE models. This method can be used to obtain full-field deformation information with such a high resolution to, e.g., study the strain field in the vicinity of knots. Despite the wide application of the DIC technique, its use in the field of wood science and technology is rather limited. In 2006, Murata et al. (2006) investigated the strain distribution of wooden members subjected to four-point bending tests using the DIC method. Oscarsson et al. (2012) used the DIC technique to detect strain fields around knots in tensile loaded Norway spruce specimens and compared them to results of linear-elastic FE calculations. Dubois et al. (2012) studied the characterization of timber fracture employing DIC and FE method. Further applications of the DIC technique in connection with wood were investigations of adhesive bonds (Serrano and Enquist (2005)) or steel-to-timber joints, both accompanied by two-dimensional FE simulations (Sjödín et al. (2006, 2008)). Xavier et al. (2012) used DIC to account for the influence of specimen parasitic end-effects in the determination of the modulus of elasticity in longitudinal direction in compression tests. In addition to these applications of the DIC technique, Le Magorou et al. (2002) and Xavier et al. (2013) used full-field measurements to simultaneously identify wood material parameters in plate bending tests of wood-based panels, like medium density fiberboards (MDF), in single tests instead of identifying each parameter by itself.

As far as the authors know, a complex three-dimensional numerical simulation tool for wooden boards with knots has not experienced a comprehensive validation by means of the DIC technique yet. This is the main focus of the presented work, in which the performance of the FE model by Lukacevic and Füssl (2014) is assessed by means of four-point bending tests accompanied by full-field deformation measurements with a DIC system. The used numerical tool combines a realistic geometrical model for the grain course and a micromechanical model for a density and moisture dependent characterization of the clear-wood material, allowing a realistic reproduction of the complex three-dimensional fiber course in the vicinity of knots to analyze its effect on the stiffness and strength of wooden boards under several loading conditions. The emergence of such new modeling approaches increases the need for additional validation techniques in addition to simple comparisons of effective stiffness and strength values.

Within this paper, the suitability of full-field deformation measurements for four-point bending tests on wooden boards is discussed first and local phenomena are considered in detail. A comprehensive test series is then used to validate the strain field distributions determined by the abovementioned numerical simulation tool (Lukacevic and Füssl (2014)), especially with regard to the influence of knots.

2.2 Materials and methods

Four-point bending tests were conducted at the laboratory of the Research Center of Building Materials, Material Technology and Fire Safety Science of the Vienna University of Technology (14 specimens) and at the Laboratory for Macroscopic Material Testing of the Institute for Mechanics of Materials and Structures (IMWS) of the Vienna University of Technology (20 specimens). All samples were prepared of Norway spruce

(*Picea abies*). The boards were taken from a wood trader and selected by taking certain points into account: knots should be situated in the center third and should especially be avoided below the load application points. This ensures the occurrence of significant knots in the area of the maximum moment (constant between the two load application points). Preferably, a single knot/knot group was situated in the tension zone of the board. Under these conditions explicit information about the influence of knots/knot groups (in combination with the fiber deviation in its vicinity) on the bending strength of the board could be gained. The width of all tested boards of the test series was 40 mm and the height varied between 115, 145 and 185 mm. For the tests at the IMWS a tri-axial servo-hydraulic testing machine manufactured by Walter & Bai, with built-in load cells for a maximum load of 250 kN and 10 kN, respectively, an 0 to 110 mm encoder and computer assisted analysis, was used (for further details see Griessner (2013)).

The experimental setup is based on the regulations defined in DIN EN 408 (Timber structures – Structural timber and glued laminated timber – Determination of some physical and mechanical properties) (DIN EN 408, 2010a). The standard provides information about specimen properties and dimensions, experimental setup and load application.

The tests were performed displacement controlled, using the machine's 250 kN load cell. A steel girder distributed the load to the load application points. Small steel plates were attached to the specimen at the load application points and supports, in order to avoid local indentations. Steel cylinders, with a diameter of 10 mm, between girder and plate served as a roller-bearing, such that local constraints could be prevented. The load was applied with a constant rate of 20 mm/min and stopped as soon as the test specimen collapsed. For each test, a load-displacement curve up to failure (maximum load P_{max}) was recorded. Every single test was documented in detail with pictures and/or videos to provide an appropriate basis for the evaluation of the test results.

The overall length of the vertically tested boards was 4000 mm, the distance between the supports was specified with 3000 mm and the load was applied in the boards' third points, allowing a flexibility in the alignment of the boards with respect to knots/knot groups.

2.2.1 Full-field deformation measurements

15 vertically tested boards were selected to be investigated in detail by using the digital image correlation (DIC) technique. This method allows full-field, non-contact and three-dimensional surface deformation measurements and enables thereby the evaluation of the influence of 'material inhomogeneities' on the global mechanical behavior. In our case the focus was laid on the impact of knots and the resulting fiber deviations in their vicinity on the bending strength of wooden boards.

The measurement technique was first developed in the 1980s (Sutton et al., 1986, 1983) and is based on the correlation of facet elements in digital images taken by CCD cameras. To allow such a subdivision of the digital image of the test specimen into small, partially overlapping square subsets or facets, an identifiable gray value pattern on the sample's surface is required. Such a pattern was applied to the regions of interest (ROIs)

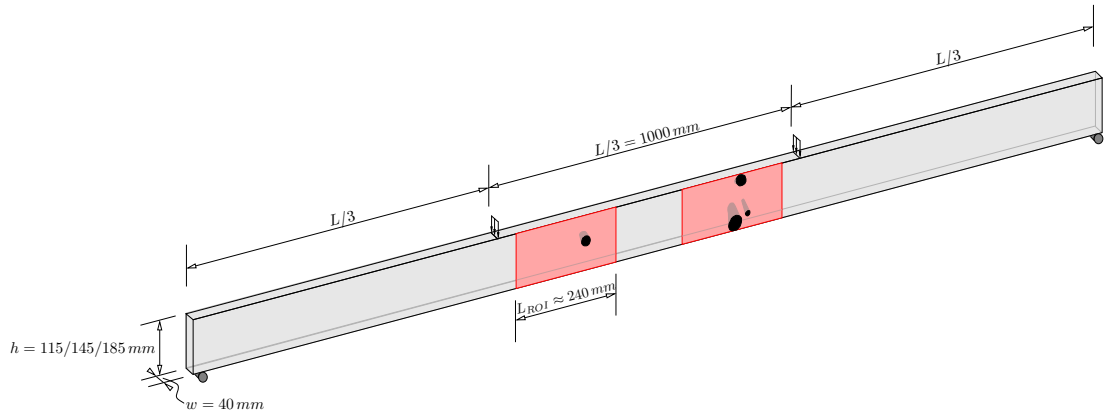


Figure 2.1: Four-point bending test setup and configuration of the wooden boards with two regions of interest (reddish areas).

of the specimens using ordinary spray paint (see Figure 2.2 for an exemplary pattern). In order to avoid the infiltration, and thus a dispersion of the paint, in a pre-treatment step, the surface of the specimens was covered with a thin layer of wax.

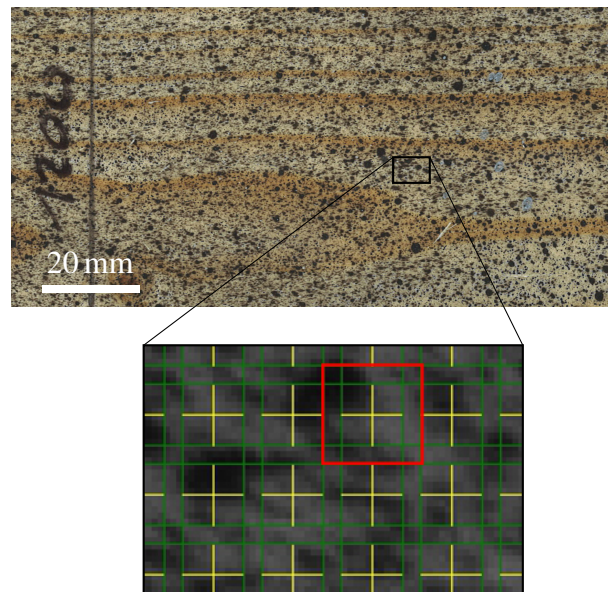


Figure 2.2: Example of the applied gray value pattern of specimen 17, and detail of the specimen surface with grid spacing of the facets and overlap of neighboring facets. The boundary of one facet is indicated in red.

For every specimen, two ROIs were specified, one on each side of the middle axis (see Figure 2.1, reddish rectangles), with two cameras working together in a master-slave fashion on each ROI, respectively, as for three-dimensional, stereoscopic measurements a two camera setup is needed. The high-resolution cameras are numbered in ascending order from left to right, hence, the left ROI (ROI_I) is recorded with cameras 1 and 2 and the right ROI (ROI_{II}) with cameras 3 and 4 (see Figure 2.3). With such a

setup, it could be ensured that the location of first cracking was covered by one of the ROIs. In order to guarantee high quality images and good contrast features of the gray value pattern, in addition to the regular illumination, separate floodlights were installed and focused on the ROIs.

The device used is the Digital Image Correlation System Q-400 from Dantec Dynamics including the evaluation software ISTR4 4D, with cameras of the type Stingray F-504 from Allied Vision Technologies with 5 Megapixel CCD sensors (ICX655) and a resolution of 2452×2056 pixels (Stingray F-504bc, 2013).

After the final alignment of the test specimens, the cameras had to be focused on the ROIs and calibrated to determine the intrinsic (e.g. focal lengths and distortions of the lenses) and the extrinsic (e.g. translation vector) parameters of the DIC system. For this calibration procedure, a target plate, which is a chess pattern with known geometry (9×9 squares with a side length of 23 mm for the single squares), was positioned in front of the cameras under different perspective views, allowing the software to automatically calculate the required parameters. At the beginning of each test the load increment between two pictures was specified with 1 kN. As soon as the first discontinuities in the load-displacement curve appeared, the interval was adjusted in order to ensure an appropriate documentation of the crack propagation.

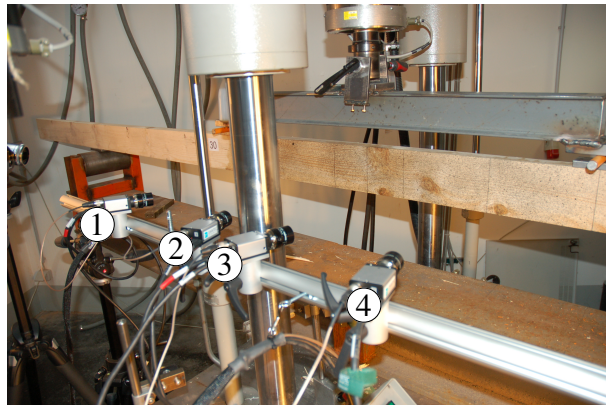


Figure 2.3: DIC camera setup with cameras 1 and 2 focused on ROI_I and cameras 3 and 4 on ROI_{II} .

2.3 Test results and evaluation

In the following, the performance of the DIC technique in general and the detectability of strain fields around knots is shown by means of an illustrative example. Moreover, the applicability of such a contact-free full-field deformation measurement system for the detection of failure and load transfer mechanisms during four-point bending tests of wooden boards is evaluated. This is a requirement for its use as a validation method of the complex, three-dimensional FE simulation tool, which will be introduced in the next chapter.

2.3.1 Strain distributions

The abovementioned evaluation software, ISTRA 4D by Dantec Dynamics (2012), allows the visualization of computed strain fields as colored contour plots of various strain components at certain load steps and section diagrams, respectively. The former ones can be used to qualitatively investigate the specimens' behavior under loading, i.e. to identify highly stressed regions and crack initiation. Section diagrams show quantitative strain variations along predefined paths.

Table 2.1: Correlation settings used for the computation of the strain fields from the DIC data.

Facet Size (<i>px</i>)	Accuracy (<i>px</i>)	Residuum (—)	3D-Residuum (<i>px</i>)	Overlap (<i>px</i>)	Grid Spacing (<i>px</i>)
15-17	0.1	15-20	0.4-0.7	3-4	12-13

The quality of the computed strain fields depends on the facet size and, as such, can be controlled by several parameters in the evaluation software. The detail in Figure 2.2 shows a typical facet grid with the overlap of neighboring facets. According to the software manual, the facet size (green) should be set to $4/3$ of the grid spacing (yellow). The chosen facet size and overlap is controlled by the desired spatial resolution and measurement accuracy. Table 2.1 gives a summary of the used parameters for the evaluation of the DIC data. The slightly bigger facet sizes and overlaps were used for a small number of samples, where the applied spray pattern showed insufficient contrast features. The parameters for the correlation residuum and the 3D-residuum, respectively, were taken from the software's default values. The chosen correlation settings result in a spatial resolution of about 1.5 mm, which is at least by a magnitude smaller than the size of the knots and about two magnitudes smaller than the height of the ROIs. Thus, it can be ensured that the heterogeneous strain fields, which must be expected due to knots, can be reproduced correctly. Furthermore, the obtained measurement data had to be smoothed to reduce the amount of noise. The smoothing intensity of the available smoothing spline filter can be controlled by the grid reduction factor and the smoothness factor, respectively. The former one defines the density of the grid points relative to the data grid and was set to 2, and the latter one limits the global curvature under the spline function and was set to -0.1, both within the recommended value range according to the software manual. Figure 2.4 shows the influence of the smoothness factor on the strain peaks in a horizontal section of specimen 16, ROI_I (cf. Figure 2.10). On the left, the strain course for the whole recommended value range is illustrated, although it must be mentioned that for low smoothness factors the resulting contour plots become very patchy and, thus, close to unusable. Anyhow, a comparison of the area under considered strain distribution, a finite length change, (see reddish area in the right plot of Figure 2.4) shows that higher peak values are accompanied by broader peaks, such that the area under the considered strain distribution remains almost constant.

A surface scan of test specimen 17 can be found in Figure 2.5, where ROI_I is sketched in red. In the lower left corner of this ROI a knot can be identified, which is cut

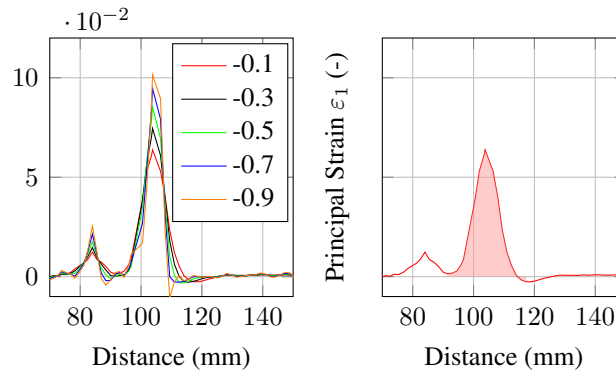


Figure 2.4: Influence of the smoothness factor on the strain course for a horizontal section (left plot) and definition of the *change in length* caused by a peak on the right.

Table 2.2: Comparison of the change in length for several smoothness factors (cf. Figure 2.4).

smoothness factor	-0.1	-0.3	-0.5	-0.7	-0.9
change in length [mm]	0.594	0.601	0.599	0.598	0.585

at the tensile loaded edge of the wooden board. Missing parts in this scan are attributed to splintering during the failure of the wooden board, more precisely, those parts did not include any knots and, thus, were not accounted for in the virtual reconstruction of the test specimen. Figure 2.6 shows the corresponding force-displacement curve, measured at the load application point. For the marked load steps, the corresponding longitudinal strain distributions ϵ_{xx} obtained from DIC measurements for ROI_I are illustrated in Figure 2.7. Steps without any apparent difference in the strain distribution compared to its previous step were omitted. Sample 17 was chosen to be analyzed in detail as the images assembled in Figure 2.7 show all essential aspects that were observable during testing and study of the evaluated strain fields.

In Figure 2.7, Step 00 shows the reference step, which was taken right after the final alignment of the test specimen with the load distributing beam already in place. Also, the testing machine's punch was in full contact with the load distributing beam. Thus, before starting the displacement controlled test, at least a force of 0.5 kN, which is equal to the beam's weight, was already applied in the reference configuration. This information must be kept in mind when evaluating the subsequent load steps. In step 02,

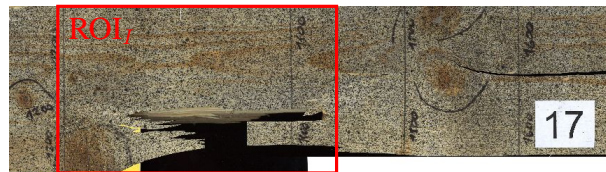


Figure 2.5: Surface scan of specimen 17 with a sketch of ROI_I (red).

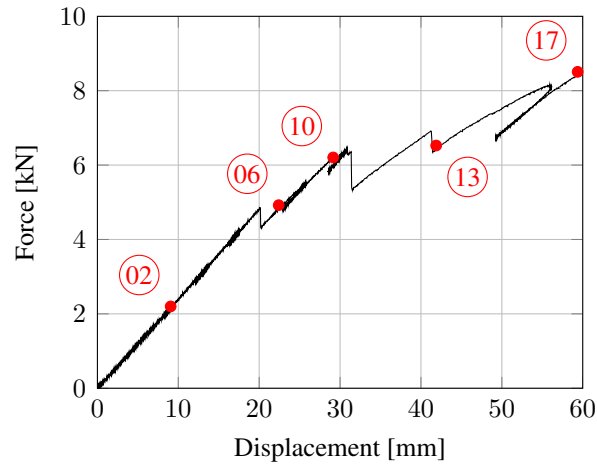


Figure 2.6: Force-displacement curve of specimen 17 (measured force as a function of the displacement at the load application point; the marked points indicate load steps, discussed in detail in this section and Figure 2.7).

which according to Figure 2.6 is clearly a purely elastic one, the tension zone in the lower part and the compression zone in the upper part are already identifiable. The largest strains in global longitudinal direction can be noticed in the knot itself. This can be explained by a vertical drying crack in the knot, which could be detected prior to testing. Such cracks can have two effects on the contour plot of the strain distribution: for regions, where large cracks destroy the applied gray value pattern, gaps in the plot become visible. As a second effect, the rigid body movements of close-by crack surfaces can be interpreted as large strains, which is not consistent with the real behavior. This effect may increase slightly by the inevitable use of smoothing algorithms. A detailed view of the knot area is shown in Figure 2.8(a). Therein also negative strains on both sides of the crack can be seen. This is caused by the abovementioned reference of the strains to step 00, in which in reality the specimen was already preloaded due to the test setup. In more specific terms, this means that actually this regions are already unloaded and free of distortion, as expected for regions close to such load free edges.

The illustrations of steps 02 to 05 show a continuous increase of strain levels in all material points. Now, the influence of the fiber deviations in the vicinity of the knot can be clearly identified. The slope of the yellowish patch in the illustration of step 05 follows the expectable stress flow around a cracked defect under bending load, so-called stress flow lines (Karihaloo (1995)). This effect is intensified by the fiber course around the knot, which deviates significantly from the global longitudinal direction. Step 06 shows the abrupt emergence of the first new crack in the lower right corner of ROI_I without any previous signs in the strain distribution. This is again accompanied by gaps in the contour plot and a successive appearance of large positive and also negative strains, respectively. This first load-induced cracking of the test specimen can also be noticed by a drop in the force-displacement curve (see Figure 2.6) right before load step 06. The sudden appearance of cracks without any prior accumulation of higher

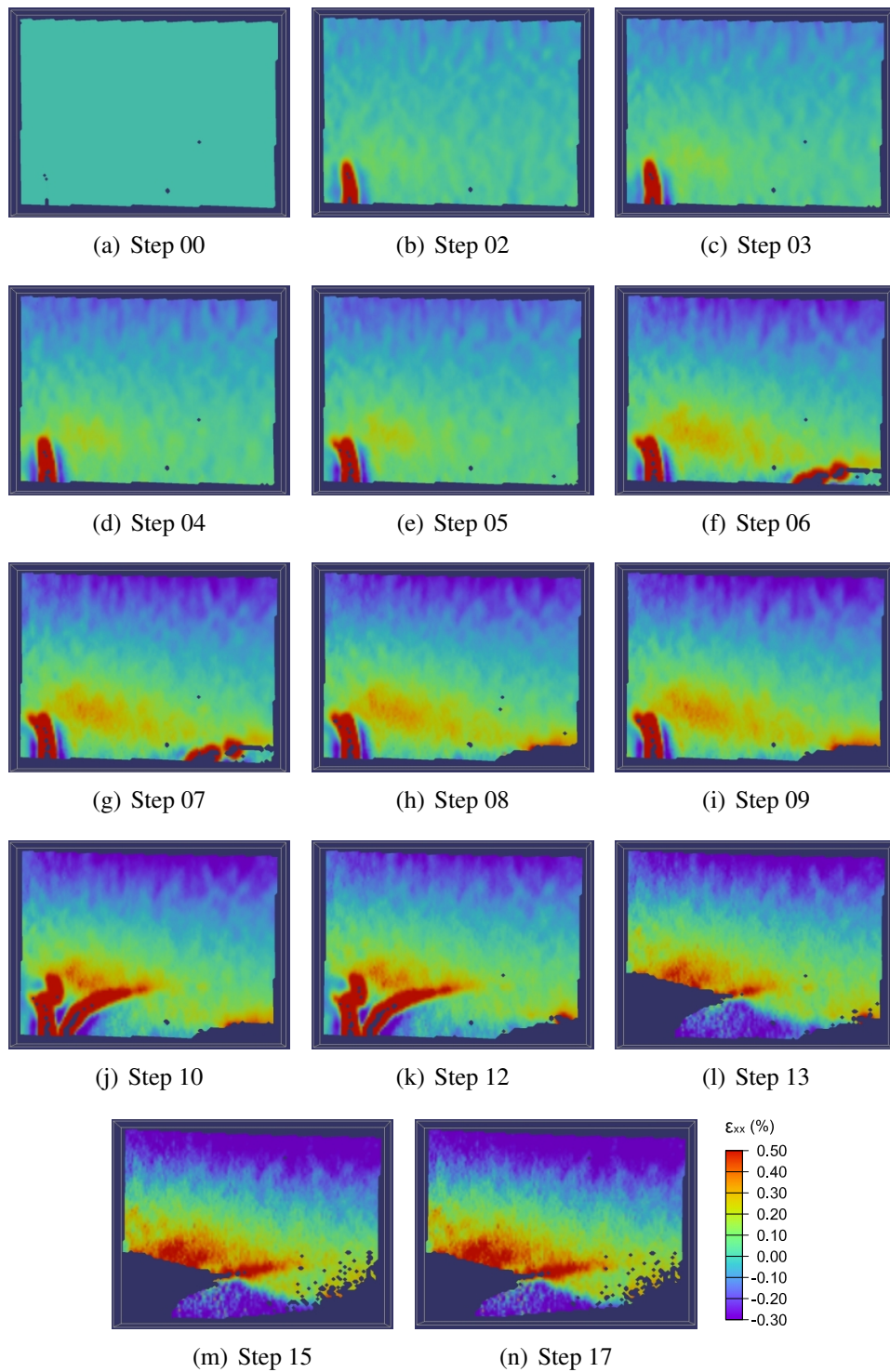


Figure 2.7: Strain distribution ϵ_{xx} obtained from DIC measurements, specimen 17, ROI_I.

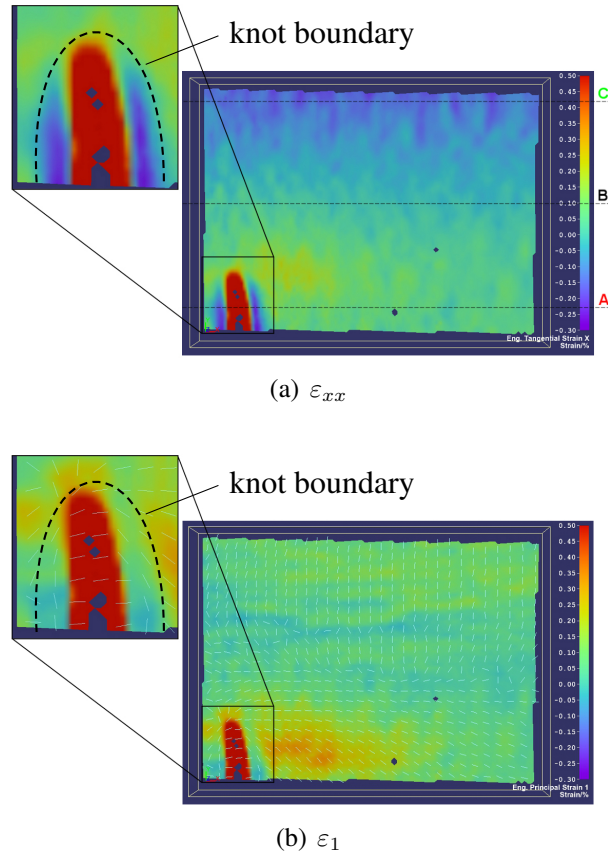


Figure 2.8: Comparison of longitudinal strains ε_{xx} and principal strains ε_1 for specimen 17, step 04, ROI_I.

strain levels could be observed throughout the whole test series. A lower load application rate could probably be used to capture such accumulations. At step 08, the cracked part of the cross section finally breaks off and at step 10, another crack/strain concentration appears in the immediate neighborhood of the knot. At step 13, the knot section finally breaks off the specimen. This can not be seen in the surface scan in Figure 2.5, as this part was virtually reattached with an image editing software during the virtual reconstruction process. The remaining cross section is already significantly weakened and at step 17 the specimen collapses. Paying special attention to the strains at the crack tip, it can be seen that they constantly increase until the final collapse at step 17.

The computation of strain values requires that the whole facet is fully covered with the stochastic pattern. For facets placed along the top or bottom edge of the specimen, just a part of the facet is inside the area of the applied pattern. This explains the discontinuous boundaries of the plotted strain fields.

Figure 2.8 shows a comparison of longitudinal strains ε_{xx} and maximum principal strains ε_1 for time step 04. In addition to the contour plot, Figure 2.8(b) illustrates the principal strain directions indicated by the light blue lines. The dashed lines in Figure 2.8(a) mark sections where the strains are plotted in the corresponding diagram

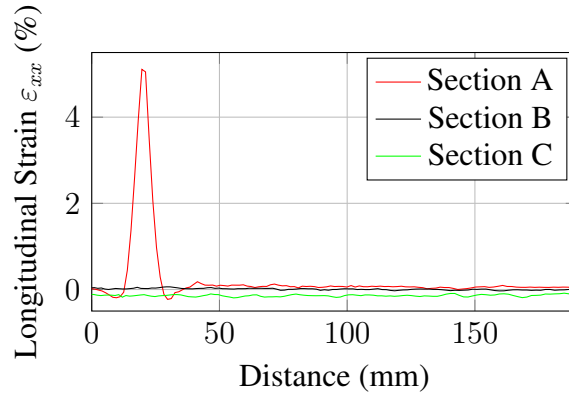


Figure 2.9: Section strain diagram ε_{xx} for sections A, B and C, as defined in Figure 2.8(a).

in Figure 2.9. The colors of the letters naming the sections indicate the color of the corresponding curve in Figure 2.9.

The directions of the principal strains in the area of the knot are in longitudinal direction of the board perpendicular to the crack. In the adjacent area, the vectors are in almost vertical direction in accordance with the negative longitudinal strains. With increasing distance from the knot region, the direction of the principal strains in the tension zone changes continuously to the expected longitudinal direction. Furthermore, the development of tension and compression zone can be clearly identified in the right part of Figure 2.8(b). The vectors in longitudinal direction in the lower half indicate the tension zone and the vertical vectors in the upper half describe the compression zone. In the neutral axis the vectors change their direction.

The peak of the graph of section A in Figure 2.9 depicts the huge apparent strains in longitudinal direction in the area of the knot with a maximum of 5.1%. As discussed above the peak rather represents displacements caused by gradual widening of the drying crack than real strains. Section B is situated more or less in the neutral axis of the specimen and the graph shows that the strains ε_{xx} are approximately equal to zero. The position of section C is close to the upper edge in the compression zone and the longitudinal strains are negative, indicated by the green line in Figure 2.9.

The presented example should demonstrate that with the DIC technique reliable and consistent full-field strain information can be obtained. Strain field variation around knots can be captured and cracks are simple to identify. Distortion free regions, as supposed around cracks, appear and evolve as expected. A comparison of experimentally and numerically obtained strain fields is therefore possible and will be shown later.

2.4 Numerical analyses

The experimental results were used to assess the performance of a three-dimensional simulation tool for wooden boards with knots, which is proposed in detail in Lukacevic and Füssl (2014). A brief description is given in the following.

The simulation tool basically combines a geometrical model for the grain course and a micromechanical model for a density and moisture dependent characterization of the clear-wood material. The former allows for the description of the three-dimensional fiber course in the vicinity of knots. For that, knots are modeled as rotationally symmetric cones with their apexes lying on a piecewise linear pith. The fiber deviation region around a knot is defined by a cone with the same apex and axis as the cone representing the knot itself, but with the fourfold apex angle. In this region in each integration point the principal material directions are determined by an algorithm based on the model proposed by Foley (2003), which assumes that there exists an analogy between the two-dimensional fiber deviation around a knot in the LT-plane and the flow of a fluid around an elliptic obstacle. Polynomial functions, which are fitted to growth ring patterns visible in the LR-planes, yield the out-of-plane fiber deviations and describe the typical knot bump. The fiber direction in undisturbed clear-wood regions (not in the vicinity of a knot) only depends on the orientation of the pith. In the knots themselves, where transversal isotropic material behavior is assumed, the local longitudinal fiber orientation is defined to be parallel to the direction vector of the corresponding knot cone axis.

Table 2.3: Microstructural input parameters necessary for the used micromechanical model Hofstetter et al. (2005, 2007) for the prediction of orthotropic stiffness tensor components.

constituent	cellulose	hemi-cellulose	lignin	extractives
weight fraction [%]	43.7	27.7	23.6	5.0

The material properties with respect to the principal material directions are determined by means of a micromechanical model developed by Hofstetter et al. (2005, 2007). It allows the calculation of the stiffness tensor components from a few universal nanoscaled constituents and from microstructural properties, such as clear-wood density, moisture content, microfibril angle and volume fractions of hemicellulose, cellulose, lignin, and water (see Table 2.3 for the used input parameters). Thus, by varying the microstructural input parameters, the simulation tool can be applied to any wood species and sample, taking into account the large variability of stiffness properties. The failure criterion of Tsai and Wu for orthotropic materials with different strengths in tension and compression is used to define local failure, where the twelve independent nonzero tensor components are estimated according to Eberhardsteiner (2002) and Kollmann (1982), considering the actual clear-wood densities. The material model of wood for the three-dimensional stress space was implemented into a user-subroutine (UMAT) of the commercial FE software *Abaqus* by Dorn (2012).

To allow a comparison of the tested specimens with numerical simulations, the destructed wooden boards had to be fully reconstructed on the computer. Therein, the reconstruction should represent the real geometry as precisely as possible. This was done by scanning the board surfaces with a commercial flatbed scanner, processing and

putting the images together in a photo editing program and finally generating a three-dimensional geometric model from that information. This reconstruction process is described in detail in Lukacevic and Füssl (2014).

2.4.1 Strain fields

In this section, results obtained from DIC analyses are compared to simulation results of the same virtually reconstructed boards. This was carried out on a basis of contour plots of principal strains and strain distributions along marked sections in horizontal as well as in vertical direction. In Figure 2.10 such a comparison is exemplarily shown, in which plot 2.10(a) represents the numerical result and plot 2.10(b) the experimentally obtained one. Further comparisons for another 8 boards are provided in the Appendix (Figures 2.14 to 2.21). All pairs of strain fields are compared at the same load level, which was defined as being the last load level before the samples collapsed. Moreover, to all contour plots the same scale and color spectrum is applied.

In all contour plots horizontal and vertical sections are defined, indicated with dashed lines. Horizontal sections are named with letters A, B and C and vertical sections are marked with numbers 1, 2 and 3. The different colors of the denotations indicate the color of the graph in the corresponding diagram. In the diagrams (c) and (d) of the comparison figures of strain fields (Figures 2.10 and 2.14 to 2.21), the results obtained from *Abaqus* are illustrated with a solid line and those obtained from DIC analysis with a dashed line. Because of the missing possibility for a calibration of the global coordinate systems of the two different software packages, the position of the sections had to be adjusted manually, using the knots as orientation points. Additionally, in *Abaqus* the positioning of sections was restricted by the position of element nodes, which were needed at each end of the section. Nevertheless, the comparison should allow good qualitative as well as meaningful quantitative statements about the reliability of the FE simulations.

Three sections are evaluated in horizontal as well as in vertical direction, unless for specimens with just one knot or 'incomplete' strain fields. The position of the sections is chosen depending on the strain distribution and position of knots, in order to show detailed information of the most interesting zones.

Figure 2.10 shows the comparison of the strain distributions for ROI_I of specimen 16 and will be discussed in detail. Due to necessary model assumptions, like geometrical idealizations and a perfect connection of the cones representing knots to the surrounding block, not all visible effects in the experiment can be reproduced by the FE simulation. Since the maximum principal strains in the compression zone are of little significance, the main focus of the comparison is on the tension zone. In the compression zone the largest absolute values of strains are, in fact, the minimum principal strains. Thus, especially in the tension zone similarities can be identified. As already mentioned, drying-induced pre-cracking of knots and also the emergence of load-induced cracks were not considered in this simulation tool. Therefore, especially in the knots themselves, quite large discrepancies can be noticed. The effect of large strains in knots, caused by rigid body movements of crack surfaces and microcracks,

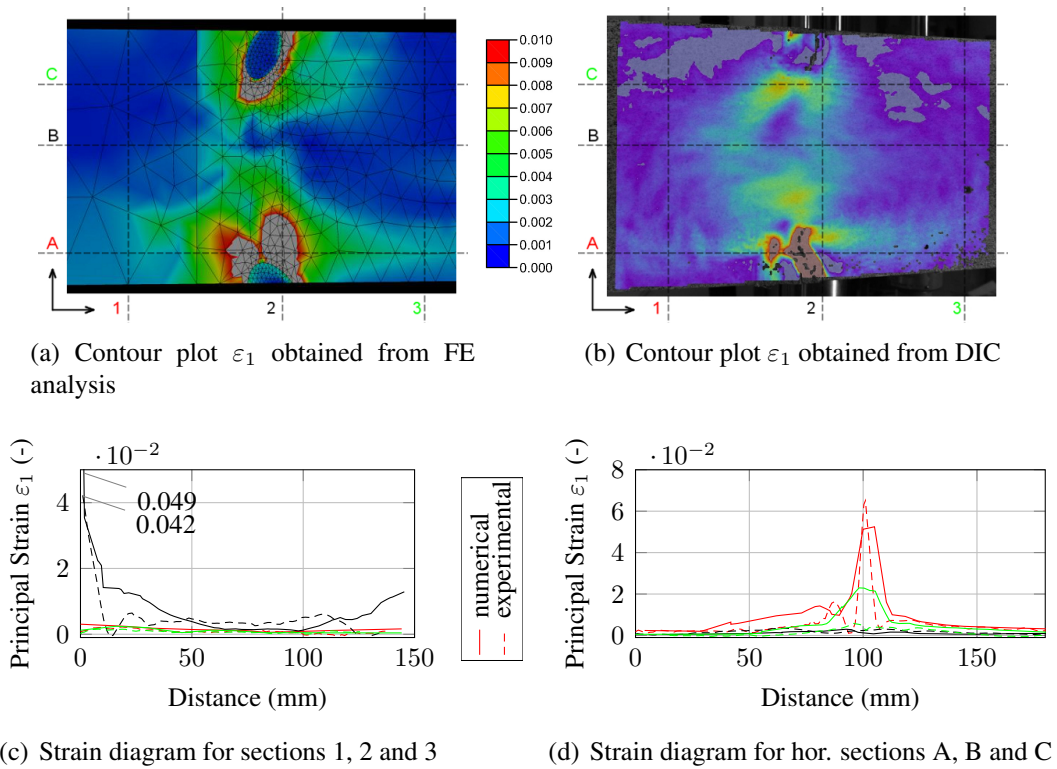


Figure 2.10: Comparison of maximum principal strain distribution, specimen 16, ROI_T.

can clearly be seen in Figure 2.10(b), where the corresponding strain values (gray areas) are higher than the largest value on the strain scale. In contrast, the highest strains in Figure 2.10(a) can be found in the immediate neighborhood of the bottom knot with clearly visible knot boundaries. This sharp transition of strain levels from surrounding wood material to knot material is on one hand caused by the abovementioned perfect connection of the knots, on the other hand in the FE model the stiffness of the knot material is by far higher than the one of the clear wood material and stiffness reducing effects such as drying cracks are not considered. But, in general, the strain distribution in and around knots obtained from the FE analysis is consistent with the assumed load transfer in this region, like explained earlier. The redirection of longitudinal stresses around knots causes large stresses and strains in the immediate vicinity of knots, while the knot area itself is widely free of stresses and strains in longitudinal direction.

The section diagrams also show good agreement between experimental and numerical results. For sections not situated in the direct vicinity of knots, the measured as well as the computed strains are small and show an approximately constant trend for the illustrated scale. Due to their small size they are largely irrelevant for the purpose of this comparison. The accumulation of large strains close to knots is indicated by the peaks in the section diagrams. Considering the imprecisions in matching the sections in the different evaluations, the peaks show good agreement in size and position. The density of data points for the DIC evaluation depends on the size of the facet mesh, which is much finer than the element mesh of the FE simulation. As already mentioned

Table 2.4: Comparison of the area under the curve caused by peaks in the strain course of several sections ($R^2=0.849$ and average absolute error of 20.4 %).

specimen nr.	ROI	area under the curve [mm]		absolute error [%]
		experimental	numerical	
16	I_h	0.594	0.732	8.8
16	I_v	0.216	0.209	3.2
16	II	0.217	0.337	35.5
18	I	1.260	1.585	20.5
19	I	0.215	0.228	5.6
20	I	0.498	0.487	2.3
20	II	0.608	0.472	29.0
22	II	0.215	0.338	36.3
23	II	0.387	0.539	28.2
24	I	0.420	0.560	25.1

before, the peak values of the experimental evaluations depend on the used smoothness factors. Thus, instead of comparing the peak values of the experiments to the results of the numerical simulations, for the horizontal section of specimen 16 (ROI_I) and for the vertical sections of all evaluated specimens and ROIs the corresponding areas under the considered strain distributions are compared in Table 2.4 (cf. Figure 2.4). This comparison shows that the FE simulation tool is able to not only capture the position of the peaks but also the magnitude of the peaks of relevant strain concentrations reliably. An average error of 20.4 % can be accepted as reasonable, taken the complexity of the problem into account.

2.4.2 Principal strain directions

Within this section, the directions of the maximum principal strains are analyzed in detail for the two ROIs of log 16 (see Figures 2.11 and 2.12). Results obtained from the FE simulation are compared to results gained from the evaluation of DIC measurement data, additional comparisons (see Figures 2.22 to 2.26) can be found in the Appendix. The maximum principal strain directions are illustrated by means of vector field plots. For an easier study of the principal strain directions, the vector fields are plotted over the corresponding board surface, obtained by the FE software, with the red areas depicting knots.

To obtain the vector fields from the FE simulations, an extrapolation step had to be conducted first, as the necessary strain information was only available in the integration points. Thus, for all elements lying on the front surface the strain components of the corresponding integration points were projected onto this surface. In addition, due to the coarse mesh size in some areas of the board and for a better comparability of the strain fields to the DIC measurements, the projected strain components had to be interpolated

in order to obtain an evenly spaced vector field. The strain directions obtained from the DIC measurements are related to the equidistant facet grid specified in the evaluation process. The small grid spacing required a reduction of data points in order to allow a clear representation of the directions.

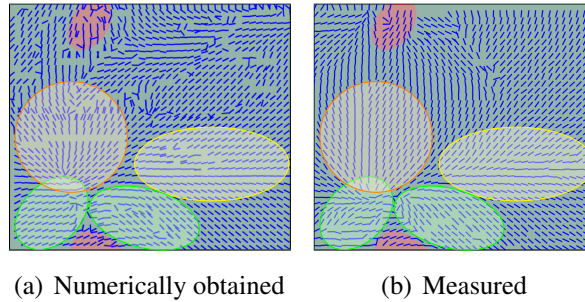


Figure 2.11: Comparison of maximum principal strain directions, specimen 16, ROI_I.

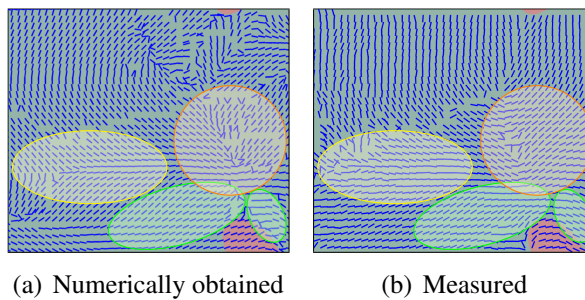


Figure 2.12: Comparison of maximum principal strain directions, specimen 16, ROI_{II}.

The principal strains in the compression zone of the loaded boards are small compared to the maximum strains in the tension zone and, therefore, their directions are of minor significance. Hence, the main focus of this comparison is laid on the tension zone, especially on the area around knots, where the largest strains appear.

Figures 2.11 and 2.12 provide a qualitative comparison of measured and numerically obtained maximum principal strain directions. Paying special attention to the tension zone and to the neighborhood of knots, the vector plots show reasonable agreement. The directions to the left and right of the lower knots (marked with green ellipses) show an almost identical course. Also the change from the inclined to the horizontal direction (yellow ellipses) is represented precisely in both images. Moreover, both vector fields indicate scattered directions immediately above the knot and the transition to the vertical direction above this scattered area is also visible in the measured as well as in the numerically obtained vector fields (orange ellipses).

The comparison of log 20, ROI_I (see Figure 2.23) exhibits some discrepancies in the compression zone. These are caused by incomplete measurement data obtained from the DIC measurements. Figure 2.25 indicates large strains in vertical direction to the left of the lower knot, which are even more distinct in the measured data. The large strains in

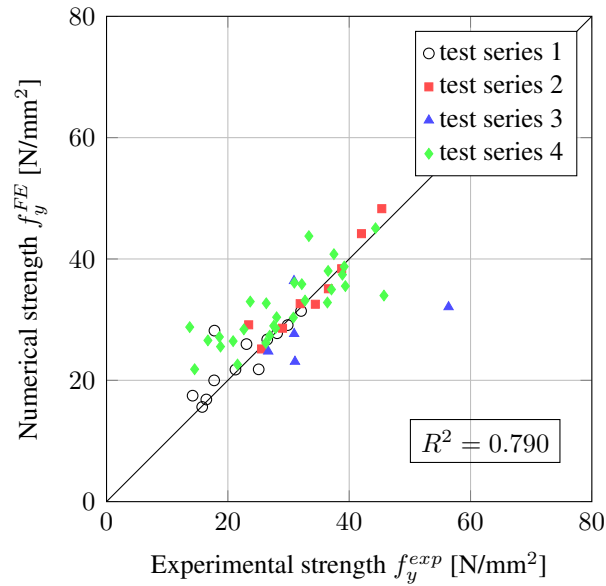


Figure 2.13: Comparison of experimentally and numerically obtained effective strengths.

this area can also be identified in the related contour plot in Figure 2.18. Those large maximum principal strains in vertical direction are assumed to be the cause of the following crack, which emerges in this area in longitudinal direction of the board. In case of a knot situated within the cross section, the stress flow around the knot in longitudinal direction happens to both sides of the knot. This causes the distinct redirection of stresses immediately next to the knot (cf. Figure 2.24).

2.4.3 Structural failure

As shown so far, within the elastic regime the numerical simulation tool is able to depict strain fields around knots appropriately and also capture the magnitude of peak values. Subsequently, these test series were also used to validate a structural failure criterion implemented in that tool, presented in Lukacevic and Füssl (2014). Therein, by evaluating the qualitative stress changes in predefined volumes in the vicinity of knots, effective strength values are determined for the reconstructed test specimens. This estimation of the strength is based on the formation of failure zones predominantly caused by perpendicular-to-grain tension close to knots. The comparison of experimentally and numerically obtained strengths are shown in Figure 2.13, where test series 4 denotes the results of the vertically tested boards described within this work. Test series 1 to 3 are previous results from bending and tensile tests, described in detail in Lukacevic and Füssl (2014). This comparison shows a very good agreement in effective strength values.

This result further indicates, that the developed numerical simulation tool is able to appropriately reproduce the basic structural behavior and does completes the validation.

2.5 Conclusion and future work

The objective of this work was to conduct comprehensive bending test series, accompanied by DIC measurements, as basis for the validation of a previously developed numerical simulation tool for wooden boards.

The DIC technique proved to be capable to reproduce the strain fields in the vicinity of knots under edgewise bending load when a few deficiencies of this method are kept in mind. Large strains in the vicinities of cracked edges, like in some knots, occur only due to the measurement type, as rigid body motions of the free crack edges can not be taken into account, leading to an overestimation of the actual strain values in these areas. Considering these discrepancies between the numerically and experimentally obtained strain fields, the overall agreement between both strain fields and also section diagrams is very good.

The comparison of the principal strain directions show predominantly clearly identifiable similarities in the confronted images. Especially in the area of large strains the plots are largely congruent. It is assumed, that the high accuracy of the computed three-dimensional fiber course based on the realistic 3D-reconstruction of the test items is the main reason for the good approximation of the strain directions. Like described earlier, the load transfer around a knot can be explained by means of stress flow lines, which widely coincide with the fiber course. Thus, the fiber course is one of the main criteria for the load transfer around the knot and its accurate approach in the FE model contributes significantly to the realistic simulation of the stress flow.

Furthermore, the conducted test series could be used for an additional validation of a previously developed structural failure criterion, showing very good agreement for most test results.

Therefore, and also to eliminate the minor differences between DIC measurements and numerical simulations, current research focus lies on the implementation of crack initiation and evolution into the existing numerical simulation tool for wooden boards by means of the extended FE method (XFEM). Using this method, a multiscale approach is used to obtain crack directions on a global level by analyzing the start of cracking at the single cell level and a homogenization scheme considering the annual year ring structure of softwood under several three-dimensional loading conditions. The numerical simulation tool can then be used as basis for the evaluation and optimization of current grading criteria and design concepts. Furthermore, the model can easily be extended to study Cross-Laminated Timber or Glued Laminated Timber.

2.6 Appendix

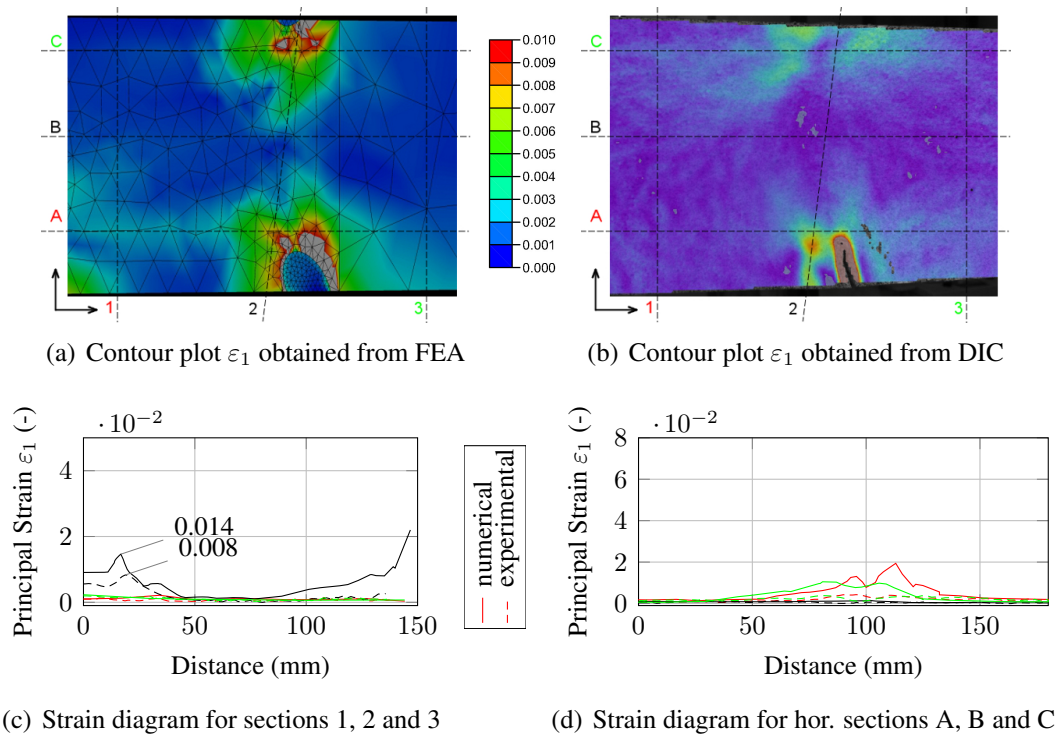


Figure 2.14: Comparison of maximum principal strain distribution, specimen 16, ROI_{II}.

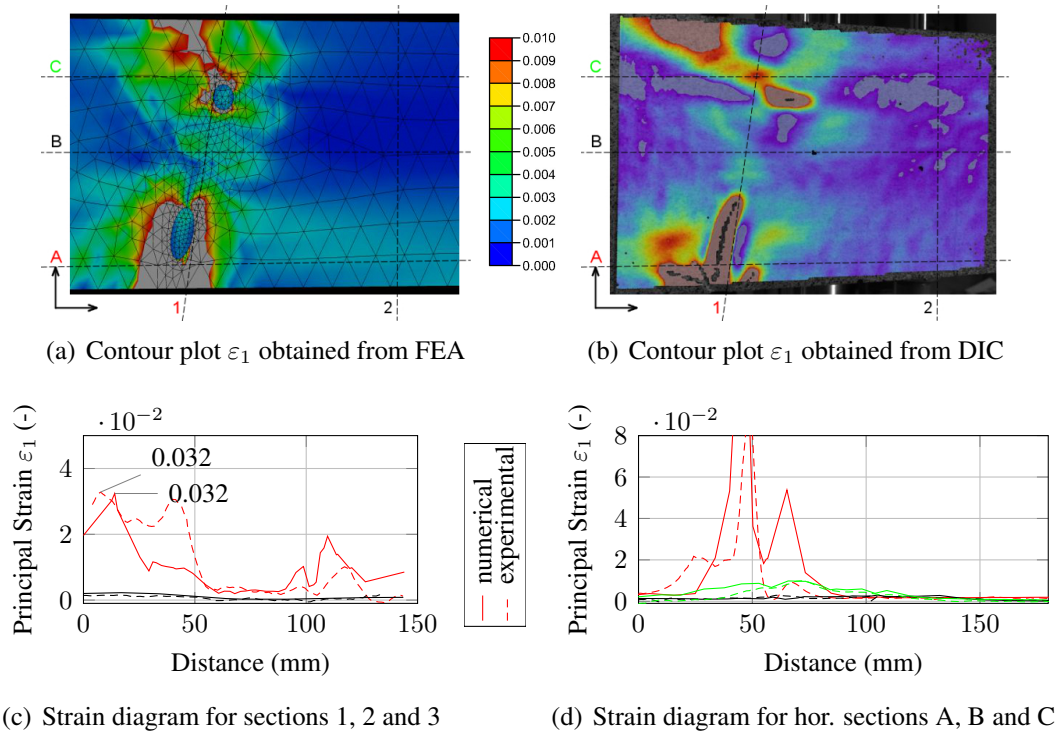


Figure 2.15: Comparison of maximum principal strain distribution, specimen 18, ROI_I.

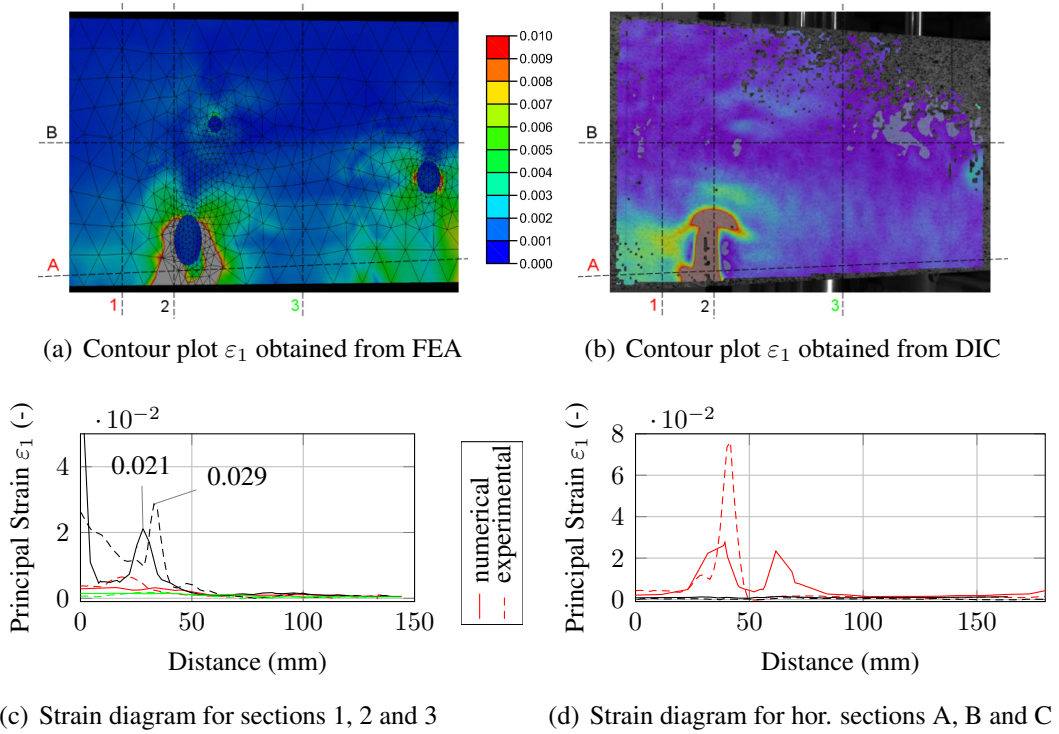


Figure 2.16: Comparison of maximum principal strain distribution, specimen 19, ROI_I.

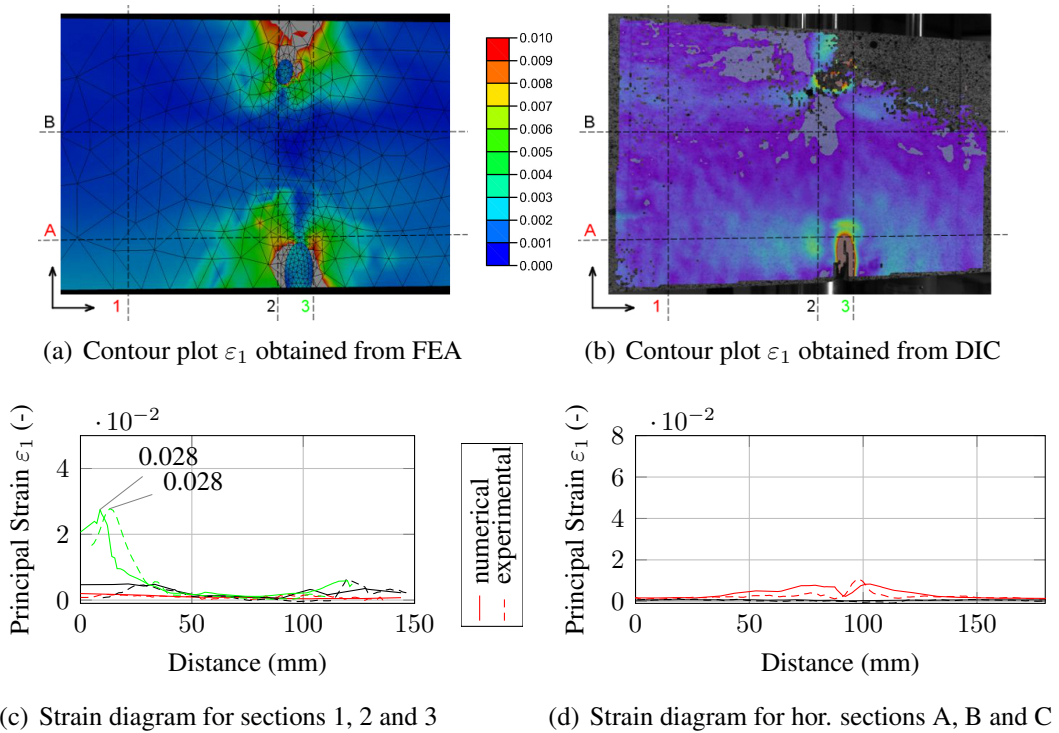


Figure 2.17: Comparison of maximum principal strain distribution, specimen 20, ROI_I.

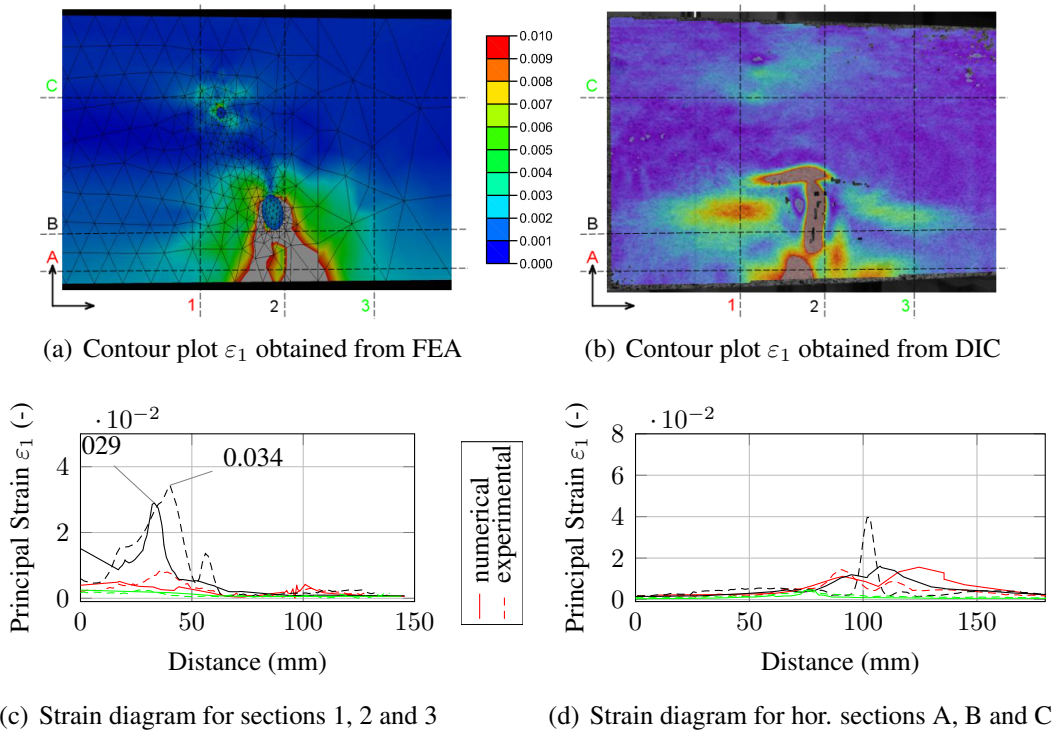


Figure 2.18: Comparison of maximum principal strain distribution, specimen 20, ROI_{II}.

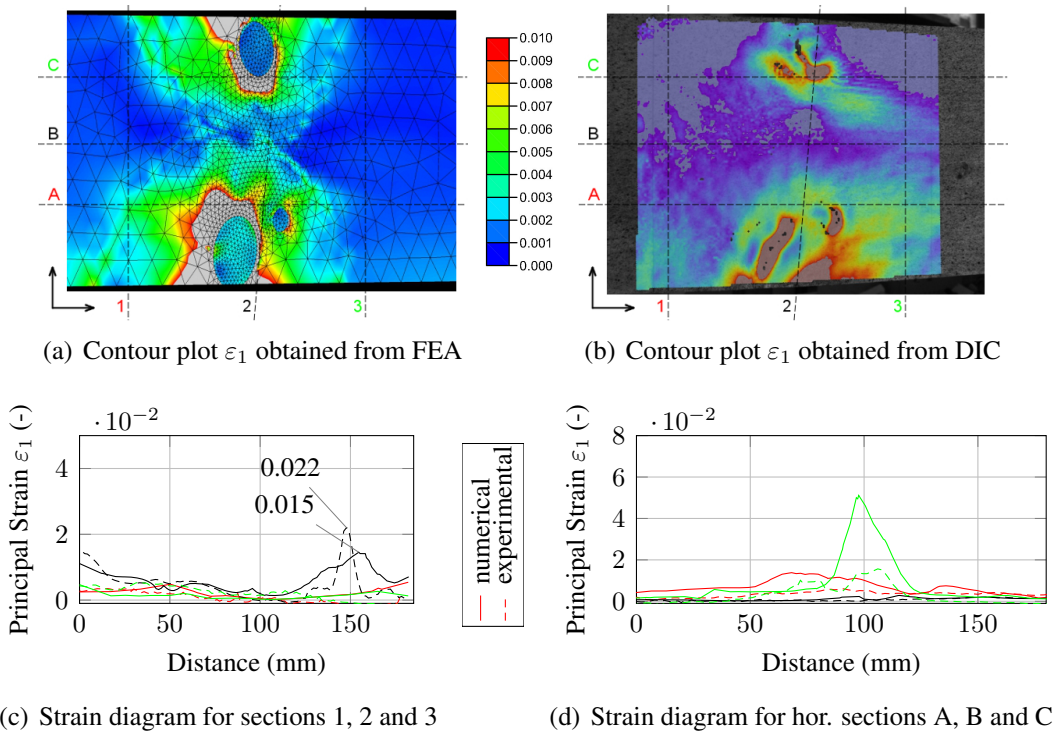


Figure 2.19: Comparison of maximum principal strain distribution, specimen 22, ROI_{II}.

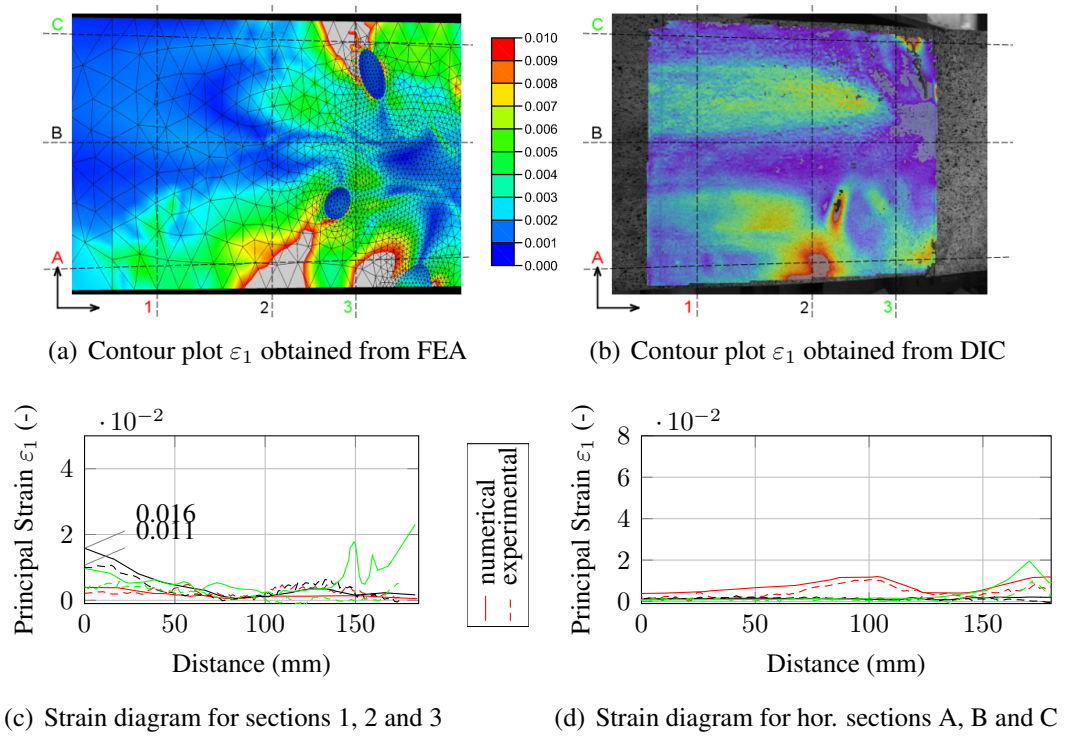


Figure 2.20: Comparison of maximum principal strain distribution, specimen 23, ROI_{II}.

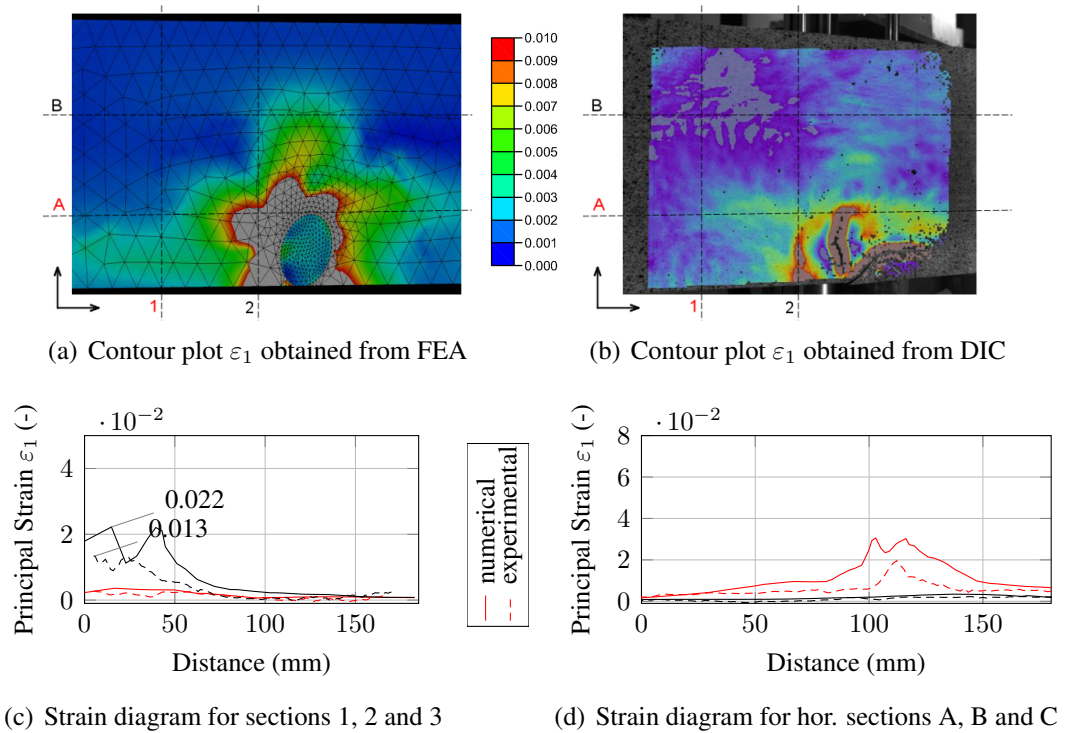


Figure 2.21: Comparison of maximum principal strain distribution, specimen 24, ROI_I.

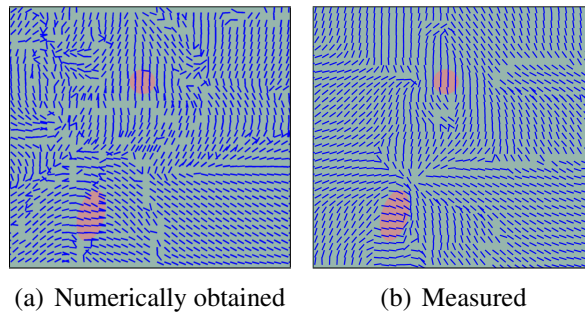


Figure 2.22: Comparison of maximum principal strain directions, specimen 18, ROI_I.

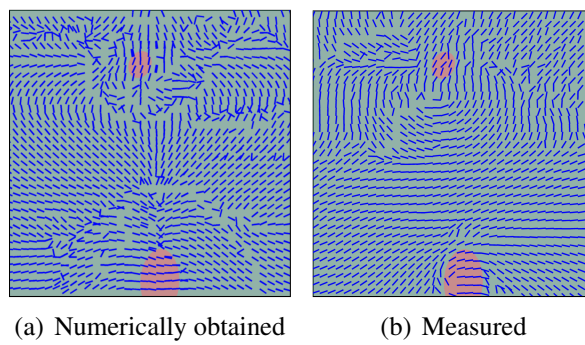


Figure 2.23: Comparison of maximum principal strain directions, specimen 20, ROI_I.

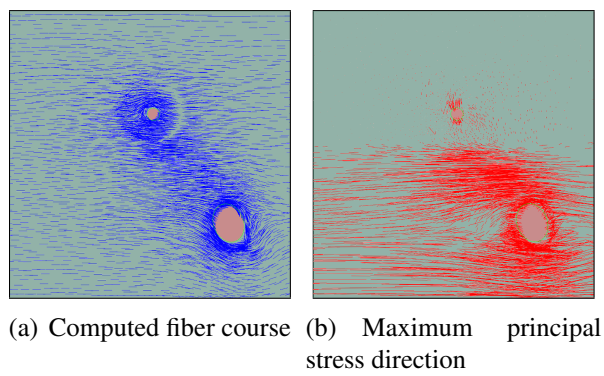


Figure 2.24: Computed fiber course and maximum principal stress directions obtained from the FE simulation, specimen 20, ROI_{II}.

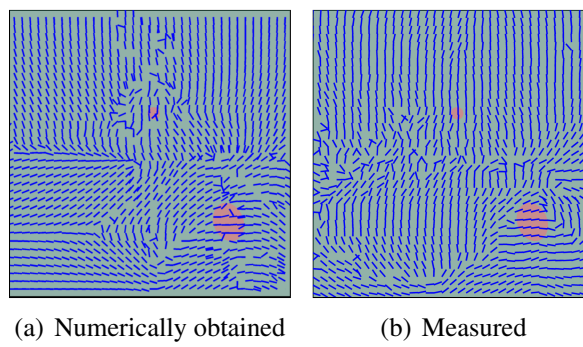


Figure 2.25: Comparison of maximum principal strain directions, specimen 20, ROI_{II}.

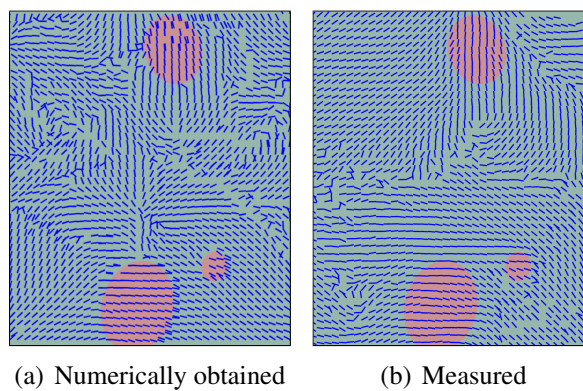


Figure 2.26: Comparison of maximum principal strain directions, specimen 22, ROI_{II}.

Failure mechanisms of clear wood identified at wood cell level by an approach based on the extended finite element method (Lukacevic et al., 2014b)

Authored by Markus Lukacevic, Josef Füssl and Ralf Lampert

Submitted to *Computational Materials Science*, 2014

Due to the complex material behavior of wood a realistic numerical simulation of its failure mechanisms is a challenging task. Nevertheless, for a reliable performance prediction of wooden boards and wood products and, thus, efficient and competitive wooden structures in civil engineering applications, it is urgently needed. The initiation and also the global direction of cracks are governed by structural features on the wooden microscale. For this reason, and to account for the layered structure of wood, within this work, all possible failure mechanisms for two repetitive units, representing late- and earlywood, respectively, are identified by an approach based on the extended finite element method (XFEM). For this purpose, 800 highly nonlinear numerical simulations have been carried out for each cell type, capturing a wide range of possible loading combinations. The classification of the obtained failure modes with assigned global crack directions leads to the definition of two multisurface failure criteria for the two cell types individually. Finally, these criteria are implemented into the subroutine of a commercial FE software and applied to tensile tests at the annual year ring scale. A

comparison of simulation and experimental results showed that the developed approach is able to reproduce essential failure mechanisms in wood correctly.

3.1 Introduction

Wood is one of the oldest but still highly used building materials. Its excellent mechanical and physical properties combined with the general trend of growing environmental awareness in civil engineering have led to an increasing demand for wooden building structures in recent years. This trend is strongly inhibited by the less sophisticated prediction of the mechanical behavior of wood as opposed to other building materials.

Here, one of the major tasks is the reliable estimation of the bearing strength of wooden structures, which allows a more efficient use and a better utilization of wood and wood composites. For this, several methods exist, which take the complexity of this naturally grown material more or less into account. A brief overview of the existing methods is given in the following.

In general, failure in wood is induced by growth irregularities, which cause very localized stress peaks. Plastic effects, such as cell wall failure, reduce these stress peaks and allow for stress redistribution. For this reason, the stress state/field at which structural failure occurs is very difficult to estimate. The use of traditional maximum stress failure criteria with an evaluation of the stress state at the integration point level leads to an underestimation of the load carrying capacity. One possibility to overcome this problem is the use of so-called *mean stress approaches* (Masuda, 1988; Landelius, 1989), where averaged stresses over a finite small area are assumed to indicate failure. These areas can be adjusted to typical features of wood, such as structural characteristics of wood fibers (Aicher et al., 2002). Serrano and Gustafsson (2006), Sjödin and Serrano (2008) and Sjödin et al. (2008) applied this approach in combination with findings of linear elastic fracture mechanics. They investigated single and multiple dowel connections, where the size of the finite area was governed by the fracture properties of the material. The suitability of different volume definitions, over which the stresses are averaged, and also the efficiency of various failure criteria was compared by Guindos (2011). Lukacevic and Füssl (2014) presented a physically-based structural failure criterion, where it was assumed that in wooden boards with knots, global failure can be related to a stress transfer mechanism, which is identifiable by evaluating averaged stress fields in the vicinity of knots.

Either way, such models are mostly dependent on empirical parameters and the true failure mechanisms cannot be mapped. This can be overcome by directly modeling fracture processes. Common damage models, which are applied successfully for other building materials like reinforced concrete, are usually not suitable for wood due to its highly brittle failure mechanisms. Therefore, several researchers used so-called cohesive elements to model cracks directly. Schmidt and Kaliske (2006) developed a 3D multisurface failure criterion, with a cohesive zone model for the description of the brittle failure under tensile and shear loading conditions. Applications of this model show promising results regarding the estimation of load carrying behavior (Schmidt

and Kaliske, 2007, 2009). Danielsson and Gustafsson (2014) also used a cohesive zone model based on plasticity theory for parameter studies of a glued laminated timber beam with a hole.

These approaches work well for a homogeneous fiber orientation and if the location of the crack path is known in advance. The weak point of this method is the influence on the failure mechanism by specifying the crack direction. As wood is a naturally grown material, usually complex stress states prevail, especially in the presence of knots and other defects, where such an approach is difficult to apply.

Within this work, the basis for a crack initiation and propagation criterion in the framework of the eXtended Finite Element Method (XFEM) is established, which will be implemented into a previously developed numerical simulation tool for wooden boards (Lukacevic and Füssl, 2014; Lukacevic et al., 2014a). The implementation of such an approach poses two questions: (1) which stress states cause the initiation of a crack? and (2) what is the corresponding global crack direction? A closer look into the material wood reveals several structural features on different length scales. Thus, to obtain the global crack direction, a multiscale damage approach is taken. First, the failure mechanisms at the single cell level are identified for late- and earlywood cells, respectively, to obtain the crack direction for several loading conditions at the lowest length scale by using the unit cell method in combination with XFEM with a special emphasis on the radial(R)/tangential(T)-plane. In a next step, these results will be combined at the annual year ring level, where late- and earlywood cells form a layered structure. This should finally lead to the future development of a failure criterion with predefined global crack directions for varying loading conditions, which can be implemented into a subroutine of commercial FE software.

In the next Section (Section 3.2), the basic concept of XFEM is briefly introduced. In Section 3.3, the early- and latewood cell geometries are defined, and their material properties, including failure mechanisms and criteria, are derived. The used methods, the simulation program and the evaluation of the results, leading to the definition of failure surfaces and crack directions for both cell types, are discussed in Section 3.4. Next, in Section 3.5, the implemented failure criteria are applied to simulations at the annual ring level and compared to experiments found in literature. Finally, in Section 3.6 concluding remarks and an outlook to future developments are given.

3.2 Theoretical background

In the conventional FEM the modeling of cracking is complicated by the lack of knowledge of the exact position of such singularities a priori. This means in case of modeling a moving crack, the mesh must be updated continuously, which makes this approach highly inefficient. The eXtended FEM (XFEM), first introduced by Belytschko and Black (1999) and based on the partition of unity method of Melenk and Babuska (1996), allows the enrichment of degrees of freedom in certain regions of the investigated model

with special displacement functions:

$$u(\mathbf{x}) \approx \sum_{i=1}^{NN} N_i(\mathbf{x}) \left[a_i + \sum_{j \in \mathcal{N}_i} G_j(\mathbf{x}) b_{ij} \right], \quad (3.1)$$

where NN is the number of nodes in the FE mesh, \mathcal{N}_i the set of active extension functions at the corresponding node, a_i the conventional FE degrees of freedom, b_{ij} the extended degrees of freedom and arbitrary extension functions G_j .

Within this work, the commercial FE software `Abaqus` is used, where the so-called level-set method (Osher and Sethian, 1988; Moës et al., 2002; Gravouil et al., 2002) is applied to describe the location and geometry of cracks. Two level-set functions (ϕ and ψ), which are two almost-orthogonal signed distance functions, are sufficient to describe arbitrary material interfaces and cracks by using FE interpolation functions.

As already mentioned, the XFEM allows the utilization of a priori knowledge about the material behavior by using specialized nodal enrichment functions. Commonly, within the XFEM, singularities caused by crack tips are modeled with crack tip functions, derived from LEFM calculations (Belytschko and Black, 1999). For elements, which are completely cut by a crack, the corresponding nodes are enriched by sign or Heavyside functions. In `Abaqus` the so-called phantom node method, developed by Song et al. (2006) and based on an approach by Hansbo and Hansbo (2004), is implemented for the simulation of moving cracks. These so-called phantom nodes are superimposed on the original nodes, which are completely tied to the corresponding original nodes for uncut elements. If the element is fully cracked, it is represented by two superimposed elements with a combination of phantom and original nodes, which are no longer constrained to each other. The behavior of the cracked surfaces can now be described by the same methods, which are used for cohesive elements. The element-by-element propagation of a crack has been successfully used for several simulations of crack propagation in Song et al. (2006) with only little mesh dependency. They also noted that, although the crack speed might be overestimated by the element-by-element propagation of a crack, its propagation path is usually in a reasonable agreement with experiments.

3.3 Materials and cell geometry

For the determination of the failure modes and, thus, the crack directions within early- and latewood of spruce, respectively, the wood cell geometries have to be defined first. Then, material models including the description of failure mechanisms are assigned to the two cell types. To be able to account for the repetitive structural features in terms of a honeycomb-like structure of the wood cells in the RT-plane, the unit cell method with periodic boundary conditions is applied.

Figure 3.1 shows a wooden log at the macroscopic scale with the used cylindrical coordinate system for the longitudinal (L), radial (R) and tangential (T) directions, taking into account the orthotropy of wood on this scale. Further, the layered structure of early- and latewood, the so-called annual rings, represent the next scale of observation.

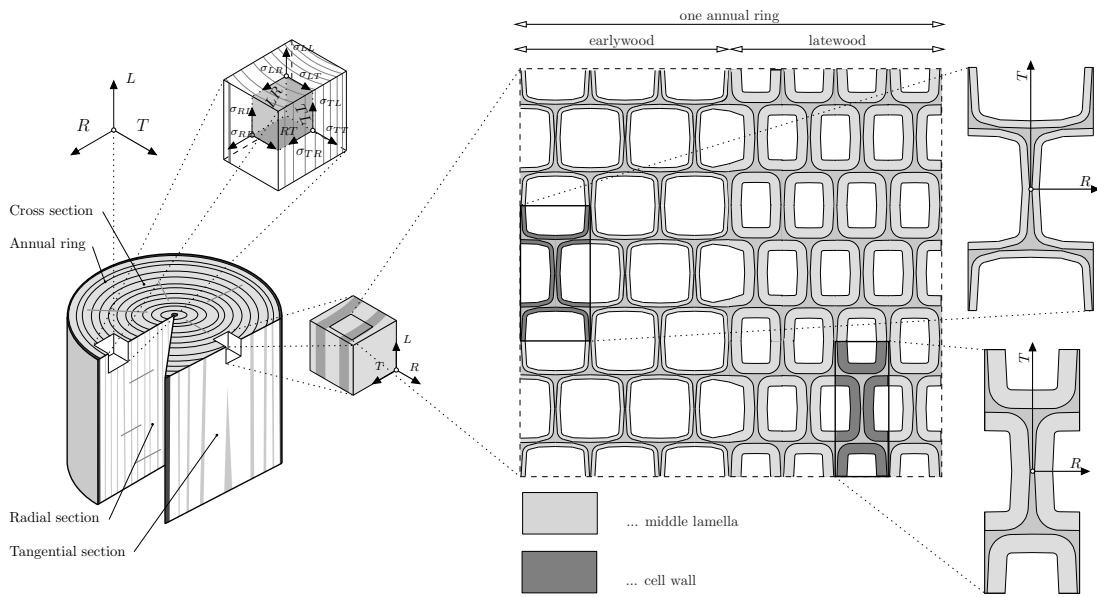


Figure 3.1: Sections of a log, coordinate system, honeycomb-like structure with extracted earlywood and latewood unit cells.

If we take a closer look at these layers, the abovementioned honeycomb-like structure is revealed. Within this paper, it is assumed that this cell structure essentially defines when plastic effects occur and how failure modes develop. Thus, for the determination of crack initiation and crack directions within these layers, the two highlighted cell types on the right of Figure 3.1, which are able to reproduce this structure, are analyzed in simulations.

3.3.1 Wood cells

Wood cells are hollow tubes running in L -direction and are connected by the so-called middle lamella, which exhibits an almost isotropic material behavior. The cell wall consists of several layers, containing cellulose fibers arranged in different angles and forming materials similar to fiber reinforced composites (see Figure 3.2).

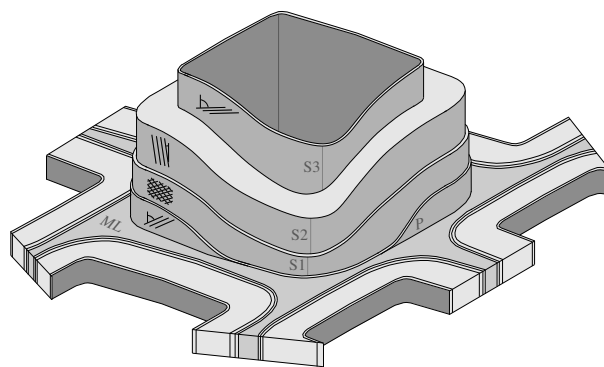


Figure 3.2: Schematic illustration of the layered cell wall

Middle lamella

The governing constituent for the mechanical behavior of the middle lamella is lignin. Due to the lack of cellulose fibers, no principle material directions can be distinguished and isotropic material behavior is assumed. The used elastic material properties are based on the findings of Gloimüller (2012) and accordingly defined as follows:

$$E = 5927.7 \text{ MPa} , \nu = 0.316 . \quad (3.2)$$

Bader et al. (2010) used the knowledge that lignin fails in shear (Zimmermann et al., 1994; Hepworth and Vincent, 1998) and a poroelastic multiscale model for softwood with a von Mises-type failure criterion to estimate the shear strength of lignin to $\sigma_{d,lig}^{ult} = 14.3 \text{ MPa}$, which will be used for the strength of the middle lamella.

With respect to this, for modeling cracks in the middle lamella with XFEM also the von Mises criterion is used to indicate crack initiation. Based on the chosen failure criterion, the plastic strain tensor can be evaluated as follows:

$$d\varepsilon_{ij}^p = d\lambda \left(\frac{s_{ij}}{\|s\|} \right) , \quad (3.3)$$

with s_{ij} being the deviatoric stress tensor. It is now assumed that the maximum principle plastic strain direction coincides with the main distortion direction and therefore indicates the crack direction (fracture plane) in the middle lamella. After crack initiation a perfect brittle damage evolution is assumed, meaning that the transferable traction stresses drop almost immediately to zero (displacement from crack initiation to stress free crack surfaces is set to 10^{-5}).

Cell wall

Figure 3.2 shows a model of the layered cell wall, which consists in total of four layers.

The primary cell wall (P), which is adjacent to the middle lamella and formed first in the cell growth process, exhibits cellulose microfibrils with a high and right-turning inclination angle. The first layer of the secondary wall ($S1$) contains crosswisely arranged microfibrils with a high microfibril angle. The second layer of the secondary cell wall ($S2$), which is the thickest of all layers, with microfibrils arranged in a small and left-turning winding angle, is primarily responsible for the structural stiffness and strength in the cells' longitudinal direction. Further, the varying thickness of the early- and latewood cell walls is caused by varying thicknesses of this layer. Finally, in the third layer of the secondary wall ($S3$) a very high, right-turning microfibril angle can be found.

As the individual modeling of several cell wall layers, including material behavior and failure mechanisms, is assumed to not lead to better results regarding the identification of the global crack direction, these layers are combined in the model to a single cell wall layer with homogenized material behavior. By using the laminate theory, according to El Omri et al. (2000), and based on a micromechanical model by Bader et al. (2011), the stiffness properties for this cell wall are obtained. All layers are composed

of highly aligned cellulose fibrils, the so-called microfibrils, embedded into a polymer matrix consisting of hemicelluloses, lignin and extractives with varying inclination angles of the microfibrils. Therefore, to all layers the same transversely isotropic stiffness tensor can be assigned. In the FE model the cell wall is subdivided into segments (see

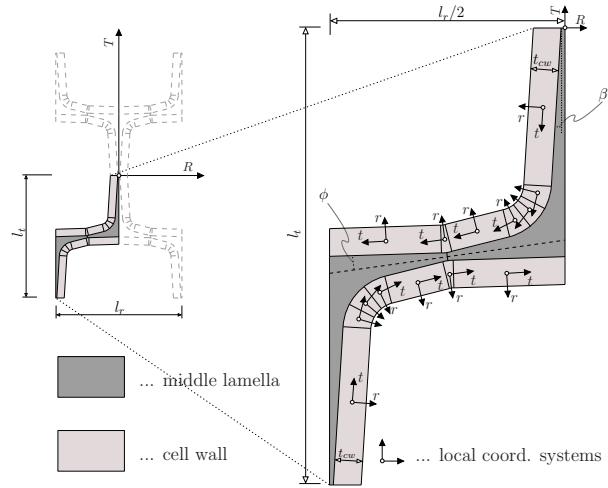


Figure 3.3: Geometry, dimensions, crack domains and local coordinate systems of the unit cells.

Figure 3.3) to allow a definition of a section-wise constant local coordinate system, describing the orthotropic material behavior. The local tangential direction is denoted by t and the radial direction, which is the direction normal to the cell wall, by r . By rotating the individual layers about the r -axis by their respective microfibril angle and through application of the laminate theory, the stiffness tensor for the cell wall is obtained, where the local l -direction is determined by the direction of the microfibrils in the S_2 -layer. The resulting stiffness tensors for the homogenized early- and latewood cell walls, respectively, are:

$$C_{cw,EW} = \begin{bmatrix} C_{rrrr} & C_{rrtt} & C_{rrll} & & & \\ & C_{tttt} & C_{ttll} & & & \\ & & C_{llll} & & & \\ & & & C_{rtrt} & & \\ \text{sym.} & & & & C_{rlrl} & \\ & & & & & C_{tlll} \end{bmatrix} \quad (3.4)$$

$$= \begin{bmatrix} 14330 & 7549 & 5717 & & & \\ & 19821 & 7227 & & & \\ & & 77408 & & & \\ & & & 6380 & & \\ \text{sym.} & & & & 2994 & \\ & & & & & 3241 \end{bmatrix} \text{ [MPa]}$$

$$C_{cw,LW} = \begin{bmatrix} 14330 & 7668 & 5598 & & & \\ & 16943 & 6361 & & & \\ & & 82018 & & & \\ & & & 4680 & & \\ \text{sym.} & & & & 2979 & \\ & & & & & 3259 \end{bmatrix} \text{ [MPa]} \quad (3.5)$$

Furthermore, it is assumed that the main failure mechanisms of the cell wall are governed by the behavior of the *S2*-layer. As already mentioned, this layer resembles a unidirectional fiber reinforced composite, a material for which several failure criteria have been developed. Following Puck's failure criterion (Puck, 1996; Puck and Schuermann, 1998), which identifies fiber failure and inter-fiber failure in a unidirectional composite, three failure criteria for the cell wall have been defined:

$$f_{cw,1}(\boldsymbol{\sigma}) \leq \frac{\sigma_l}{f_{y,l}} \quad (3.6)$$

$$f_{cw,2}(\boldsymbol{\sigma}) \leq \frac{\sigma_t}{f_{y,t}} \quad (3.7)$$

$$f_{cw,3}(\boldsymbol{\sigma}) \leq \left(\frac{\sigma_{rt}}{f_{y,rt}} \right)^2 + \left(\frac{\sigma_{tl}}{f_{y,tl}} \right)^2 \quad (3.8)$$

Equation (3.6) describes the fiber failure in local *l*-direction to which a normal direction to the fracture plane facing towards the *l*-direction is assigned to. Equation (3.7) and (3.8) both describe inter-fiber failure, and the fracture plane normal is chosen to point towards the local *t*-direction. This means that cracks are always parallel or normal to the local *l*-direction, and in the former case also normal to the cell wall and facing in the local *r*-direction. The corresponding tensile and shear strength values in Equations (3.6) to (3.8) read as:

$$f_{y,l} = 175 \text{ MPa} , f_{y,t} = 75 \text{ MPa} , \quad (3.9)$$

$$f_{y,rt} = f_{y,tl} = 43 \text{ MPa} .$$

The strength $f_{y,l}$ complies with the tensile strength of the cell wall in local *l*-direction, and for $f_{y,t}$, $f_{y,rt}$ and $f_{y,tl}$, respectively, it was assumed that the matrix material mainly consists of lignin strengthened by hemicelluloses. In addition, the strengthening effect of the opposing orientations of the microfibrils in the remaining cell wall layers *P*, *S1* and *S3*, which can be compared to a transversal reinforcement, is taken into account by increased strength levels. After crack initiation a perfect brittle damage evolution is assumed, meaning that the transferable traction stresses drop almost immediately to zero (displacement from crack initiation to stress free crack surfaces is set to 10^{-5}). Numerical simulations confirmed that the chosen values are able to reproduce the known two main fracture mechanisms for spruce in the *RT*-plane, which are fiber debonding for the thick-walled latewood cell loaded in *T*-direction and cell wall rupture for the thin-walled earlywood cells under a load in *R*-direction (Dill-Langer et al., 2002; Frühmann et al., 2003).

Table 3.1: Geometry variables and dimensions of the early- and latewood cells.

cell type	cell diameters		wall angles		thicknesses	
	l_R [μm]	l_T [μm]	ϕ [$^\circ$]	β_1 [$^\circ$]	t_{ml} [μm]	t_{cw} [μm]
earlywood	34	33	8.0	3.5	1.5	1.5
latewood	26	33	8.0	3.0	2.0	4.7

3.4 Methods and results

3.4.1 Unit cell method

According to microscopy images and values found in literature (Kollmann, 1982; Fengel and Wegener, 1983), the dimensions in Table 3.1 are chosen for the geometry definitions in Figure 3.3. The generation of the FE model within the commercial Finite-Element software Abaqus was realized by means of fully automated Python scripts, allowing for parameter studies of the geometric details in future studies.

The original unit cell method (Michel et al., 1999; Suquet, 1997; Böhm, 2004) enables the description of a heterogenous material exhibiting repetitive structural features, like the honeycomb-like arrangement of the wood cells, by means of a basic periodically repeating unit, the so-called unit cell. Periodic boundary conditions are used to obtain the microstress and microstrain fields, which allow the determination of the material's stiffness properties. For example, this approach was used for the estimation of the clear wood stiffness properties by Hofstetter et al. (2007).

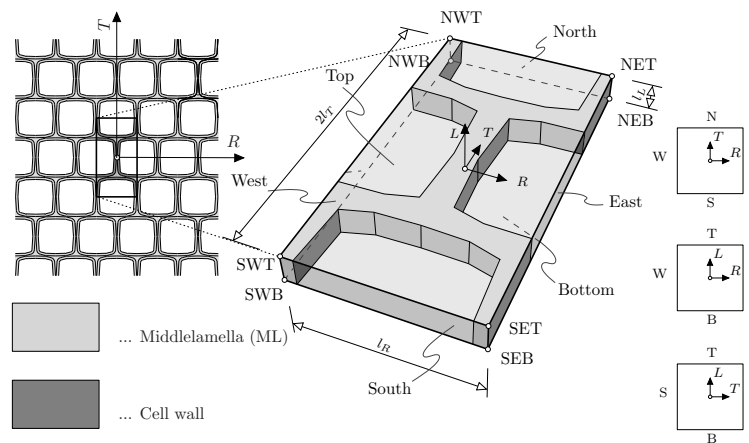


Figure 3.4: Periodic boundary condition with its master nodes

The same technique is now used to study the failure mechanisms of wood cells. Thus, the prescribed periodic boundary conditions allow the modeling of only a single

unit cell, which represents an early- and latewood layer, respectively, with an infinite number of cells. The load is applied by using so-called master nodes (see Figure 3.4).

3.4.2 Simulation program

The purpose of the simulation program was to be finally able to assign structural failure mechanisms for both, early- and latewood, to any arbitrary loading combination, i.e. tensile, compressive and shear loading. First, in preliminary simulations the maximum and minimum displacements for the three normal and the three shear directions, which have to be applied to cause failure, were determined. Then, a statistical method for generating test samples, namely latin hypercube sampling (McKay et al., 1979), was used to create a total of 800 samples with different combinations of the six applicable displacements for both cell types individually. This sampling technique ensured that the resulting stress states at failure were evenly distributed, which enabled the identification and grouping of regions with the same failure mechanisms.

Eight-node linear brick elements are used with a maximum edge length of $0.25 \mu\text{m}$ at the model borders, resulting in 17.310 and 33.804 elements for the early- and latewood unit cell, respectively. The depth of the unit cell, i.e. the length in the global L -direction of the model, was set to $0.5 \mu\text{m}$, as parameter studies showed that multiple depth values resulted in the same failure mechanisms for all examined loading conditions.

The simulations were conducted on a high-performance computing cluster with a total of three nodes, with two Intel(R) Xeon(R) E5-2640 (2.50GHz) cpus (twelve cores) and 256 GB of RAM each.

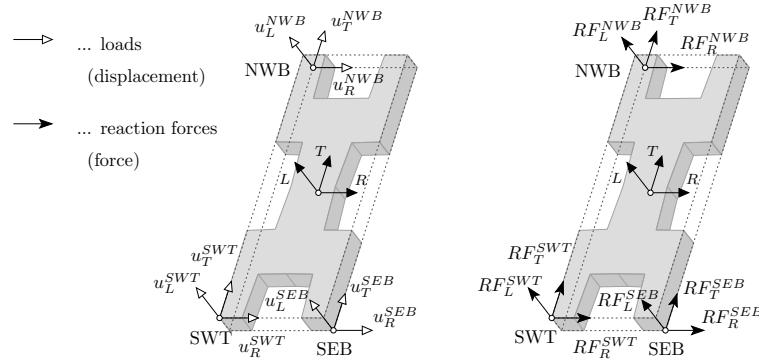


Figure 3.5: Applied loadcases and resulting reaction forces at master nodes for LW cells

On the right of Figure 3.5, the resulting reaction forces for the simulation of a unit cell are sketched. These can now be used to determine the averaged stresses on the unit cells' exterior faces:

$$\sigma_{hom} = \frac{1}{2V} \cdot (\mathbf{RF}^{-1} \cdot \mathbf{P} + \mathbf{P}^{-1} \cdot \mathbf{RF}), \quad (3.10)$$

with

$$\mathbf{RF} = \begin{bmatrix} RF_R^{SEB} & RF_T^{SEB} & RF_L^{SEB} \\ RF_R^{NWB} & RF_T^{NWB} & RF_L^{NWB} \\ RF_R^{SWT} & RF_T^{SWT} & RF_L^{SWT} \end{bmatrix}, \quad (3.11)$$

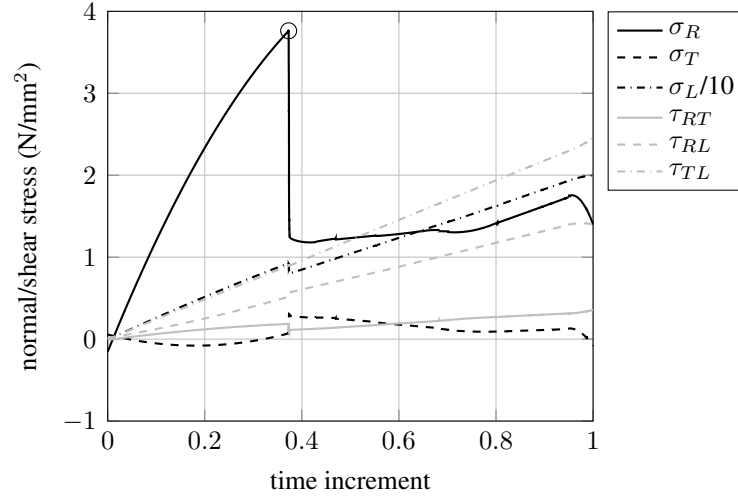


Figure 3.6: Evaluation of the stress curves for a single simulation.

$$\mathbf{P} = \begin{bmatrix} l_R & 0 & 0 \\ 0 & 2l_T & 0 \\ 0 & 0 & l_L \end{bmatrix} \text{ and } V = l_R 2l_T l_L. \quad (3.12)$$

Due to the symmetry of the shear stresses, this can be reduced to three normal and three shear stress components, which can be plotted as a function of the simulation time increment (see Figure 3.6). Within this Figure the identification of the point of failure for a single simulation is shown exemplarily (marked point). Here, the stresses were smoothed first by applying a moving average filter, before the maximum stress of the decisive curve was identified. Decisive curve means that an algorithm was used to identify first the curve with the biggest stress drop.

Figures 3.7 and 3.8 show the stress states at failure for all simulations of the late- and earlywood unit cell, respectively. The results are plotted in the σ_R - σ_T stress plane, where the size of the points is correlated to the magnitude of longitudinal shear (the bigger the points the higher the sum of τ_{LR} and τ_{LT}) and the colors indicate the magnitude of the in-plane shear component τ_{RT} (red points account for high in-plane shear stresses). Especially, the results of the much stiffer latewood show clearly that a drop-shaped envelope can be identified. In addition, the points lying on this imaginary envelope are rather small and more likely yellowish, whereas the points lying closer to the center are bigger and reddish.

3.4.3 Identification of failure modes

Based on the results of the comprehensive simulation program, the objective of this section is the definition of failure surfaces with assigned failure modes and global crack directions. To achieve this, the following procedure is applied to the two cell types individually:

- a) 2D plotting of results for selected stress regimes (with thresholds for the other stress components)

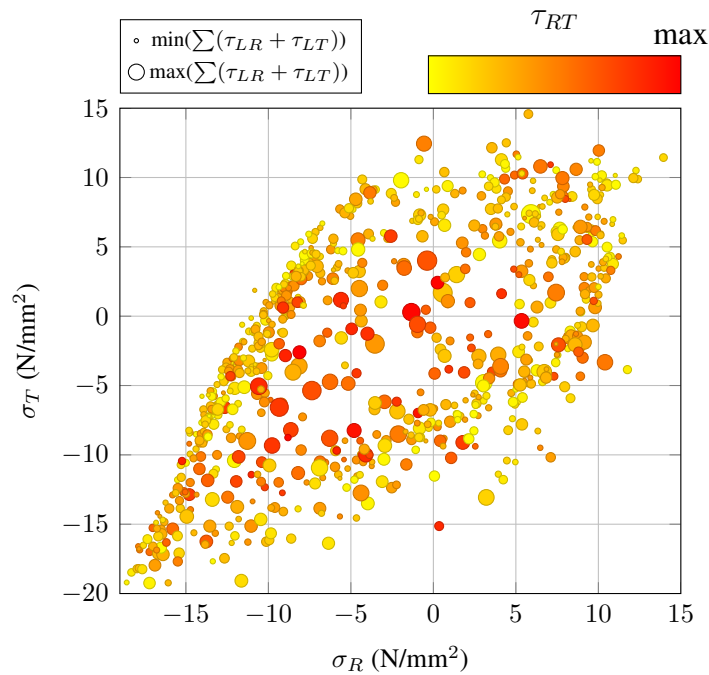


Figure 3.7: Failure stress states obtained from simulations of the latewood unit cell plotted in the σ_R - σ_T plane (the bigger the points the higher the sum of τ_{LR} and τ_{LT} , and the colors indicate the shear stress τ_{RT} according to the colorbar).

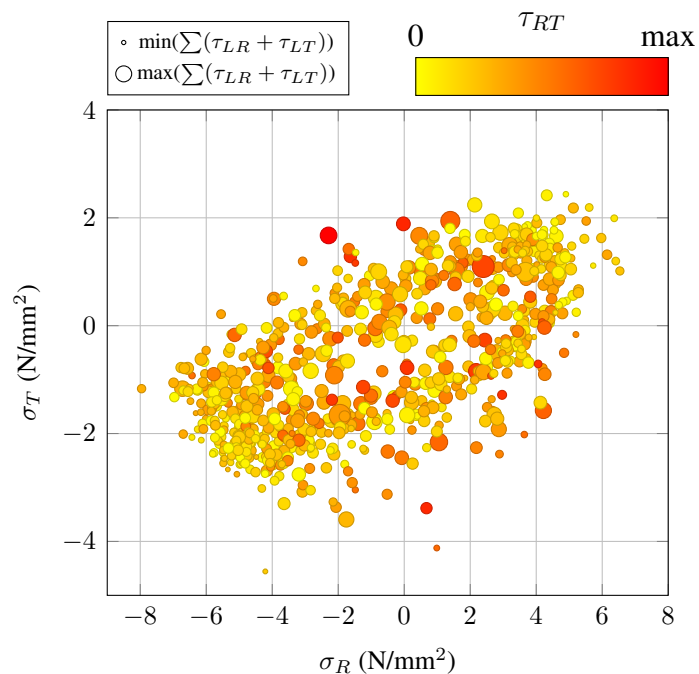


Figure 3.8: Failure stress states obtained from simulations of the earlywood unit cell plotted in the σ_R - σ_T plane (the bigger the points the higher the sum of τ_{LR} and τ_{LT} , and the colors indicate the shear stress τ_{RT} according to the colorbar).

- b) identification and classification of main failure mechanisms
- c) assignment of failure modes and global crack directions
- d) determination of failure surface for each failure mode in several stress planes

Latewood

a) Results in the σ_R - σ_T plane

As the main focus of this work lies on the identification of the crack direction within the RT -plane under an arbitrary loading condition, we first concentrate on the results within this stress plane. Further, abovementioned evaluation of Figure 3.7 showed that by concentrating on the results with low shear stress components, the total results could be reduced to the ones lying on an imaginary outer envelope. Thus, for the plot on the left of Figure 3.9 thresholds for the shear stress components and also for the normal stress in L -direction are introduced. Accordingly, the presented results only represent stress states, for which just the stress components σ_R and σ_T are not close to zero.

b) Identification of main failure mechanisms

For each simulation the associated illustration of the cracked unit cell is generated automatically at the determined point of failure. This allows for an easy evaluation of the failure mechanism for each stress state in Figure 3.9. On the bottom of Figure 3.9 the identified main failure mechanisms are shown. The arrows on the top of Figure 3.9 emphasize that the transition from one failure mode to another is in most cases very smooth. Failure mechanism ① is mainly caused by tension in T -direction, which leads to failure of the middle lamella, inducing the well-known cell wall peeling of the thick-walled latewood cells. Failure mechanism ② represents the transition from cell wall peeling to the rupture of the cell wall in the cell corner, which can be found in failure mechanism ③. The tensile loading in R -direction, which can be identified for the results of failure mechanism ④, causes mainly cracks parallel to the T -direction. Failure mechanisms ⑤ to ⑧ are mainly caused by compressive loading, leading to the appearance of cracks in the middle lamella caused by tension transversal to the loading direction.

c) Assignment of failure modes and global crack directions

In the next step, shown in Figure 3.10, the different failure mechanisms are assigned to a failure mode and to a global crack direction, respectively. The cell wall peeling of failure mechanism ① leads to a crack parallel to the R -direction. Thus, the normal to the crack plane is defined to coincide with the unity vector describing the global T -direction. The inclined crack of failure mechanism ③ is assigned to a crack normal with an angle lying between the R and T -directions. This angle is strongly influenced by cell geometry, and can therefore be considered as a geometry-dependent material parameter. The direction of the angle is governed by the sign of the in-plane shear stress τ_{RT} : the angle of the crack normal lies between the positive R and T -vectors for $\tau_{RT} \geq 0$ and is flipped about the R -axis otherwise. Failure mechanism ④ causes at the final stage a rupture of the cell walls parallel to the T -direction and is therefore assigned to a crack

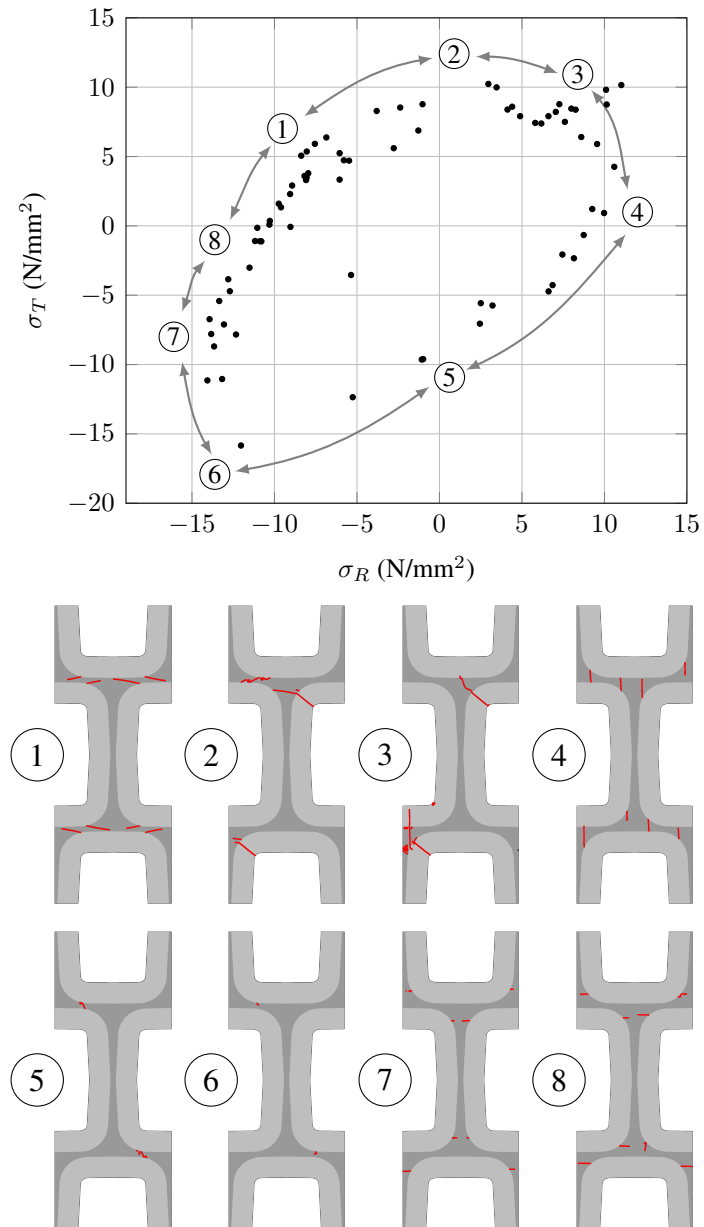


Figure 3.9: Obtained failure modes for the latewood unit cell identified in the σ_R - σ_T plane. Failure stress states with $\tau_{RT} > 0.6$ N/mm² and $\tau_{RL} = \tau_{TL} > 2.5$ N/mm² or $\sigma_L < -20$ and $\sigma_L > 20$, respectively, were excluded from the plot.

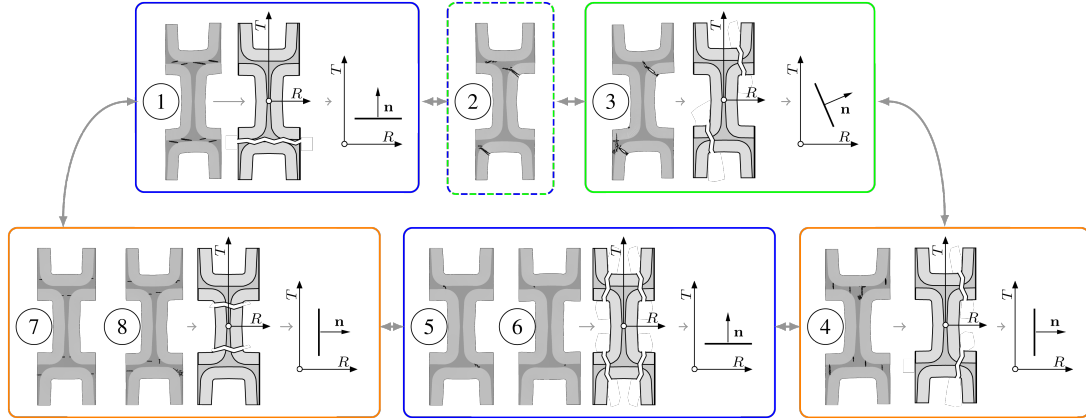


Figure 3.10: Classification of failure modes and crack directions, respectively, for the latewood unit cells.

normal, which is parallel to the vector describing the global R -direction. Both failure mechanisms (5) and (6) represent the compression of the cell in T -direction. This leads to rupture of the cell walls in the cell corners parallel to the T -direction, which is only visible if the deformed state of the cracked cell is scaled with a high deformation scale factor. Thus, these failure mechanisms are assigned to a crack normal facing towards the global T -direction. But it has to be emphasized that wood under compressive load can be better described by plastic behavior, which is why the focus within this work lies on the identification of the crack directions for tensile loading conditions, as already mentioned before. A similar behavior can be observed for failure mechanisms (7) and (8), causing crushed cells by reducing its dimensions in R -directions and finally causing tensile cracks transverse to the loading direction.

d) Determination of failure surfaces

The failure criterion of Tsai and Wu for orthotropic materials with different strengths in tension and compression is used to create a multisurface failure criterion, whereas each surface is assigned to a failure mode with a corresponding crack direction. The Tsai-Wu failure criterion reads:

$$\begin{aligned}
 f(\boldsymbol{\sigma}) = & a_{LL} \sigma_{LL} + a_{RR} \sigma_{RR} + a_{TT} \sigma_{TT} + \\
 & b_{LLLL} \sigma_{LL}^2 + b_{RRRR} \sigma_{RR}^2 + b_{TTTT} \sigma_{TT}^2 + \\
 & 2b_{LLRR} \sigma_{LL} \sigma_{RR} + 2b_{RRTT} \sigma_{RR} \sigma_{TT} + \\
 & 2b_{TTLL} \sigma_{TT} \sigma_{LL} + 4b_{LRLR} \tau_{LR}^2 + \\
 & 4b_{RTRT} \tau_{RT}^2 + 4b_{TLTL} \tau_{TL}^2 \leq 1.
 \end{aligned} \tag{3.13}$$

In a first step, the five tensor components a_{RR} , a_{TT} , b_{RRRR} , b_{TTTT} and b_{RRTT} , describing the surface in the RT -plane, are determined for each failure mode individually.

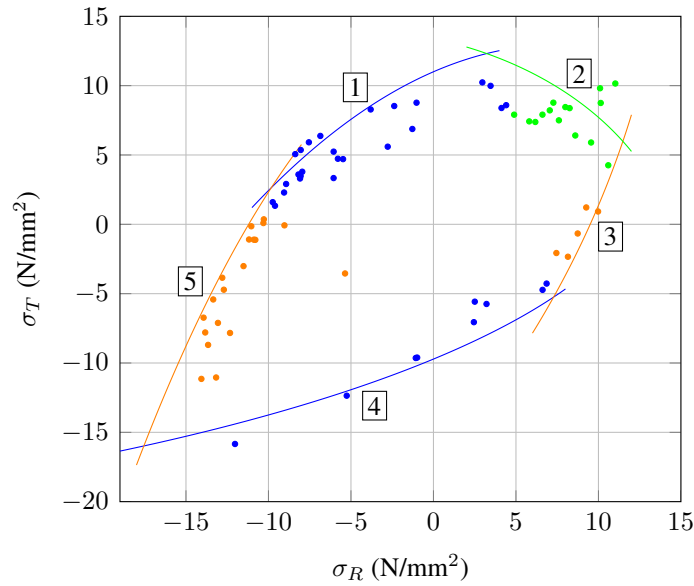


Figure 3.11: Failure surfaces for the latewood unit cell in the σ_R - σ_T plane. The different colors denote different failure modes. Failure stress states with $\tau_{RT} > 0.6 \text{ N/mm}^2$ and $\tau_{RL} = \tau_{TL} > 2.5 \text{ N/mm}^2$ or $\sigma_L < -20$ and $\sigma_L > 20$, respectively, were excluded from the determination of the failure surfaces in the σ_R - σ_T plane.

To make sure that a failure surface is only active at the intended region, the tensor components have to be restricted in the fitting process. More precisely, the curvature of each failure surface has to be chosen in a way that it is only active in the desired stress regime. In the simulation, by a subroutine each segment of the multisurface is described by a Tsai-Wu criterion and cracking is initiated if one of the failure surfaces is reached. In the aforementioned case of non-restricted failure surfaces, this would lead to false and unwanted failure mechanisms and crack directions, respectively.

In addition, for some of the failure surfaces adjustments are made, as the close inspection of failure states, and their corresponding stress curves, revealed that the simulations aborted before reaching the possible maximum stress state compared to similar simulations. Thus, for example the green curve (2) has been slightly adjusted to account for this effect, which otherwise would lead to an underestimation of the strength in this region.

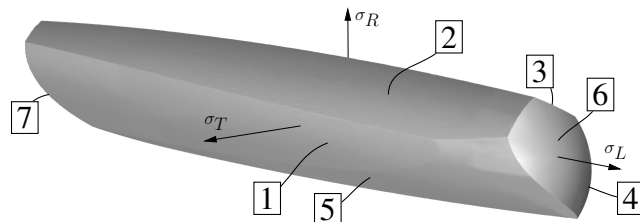


Figure 3.12: 3D representation of the latewood failure surfaces in the σ_L - σ_R - σ_T stress space with the shear stresses being equal to zero ($\tau_{LR} = \tau_{LT} = \tau_{RT} = 0$).

In the next step, the five already identified tensor components are fixed and only those failure stress states with shear stress components greater than the before defined thresholds were excluded from the fit. This means that now the normal stress σ_L is no longer restricted to values close to zero. This second fitting step now allows the determination of the following Tsai-Wu tensor components: a_{LL} , b_{LLLL} , b_{LLRR} and b_{TTLL} . In addition, two failure surfaces ([6] and [7]), restricting the stresses in L -direction are introduced. The resulting Tsai-Wu multisurface in the σ_L - σ_R - σ_T plane, with the shear stresses being equal to zero, is shown in Figure 3.12.

For the determination of the last three Tsai-Wu tensor components b_{LRLR} , b_{RTRT} and b_{TTLL} , the failure stress states obtained from simulations with non-zero shear stress components are examined. The considered shear- σ_R/σ_T stress spaces are illustrated in Figure 3.13. The applied thresholds for all other stress components are specified below each subplot. Again the failure mechanisms for all remaining simulation results are examined individually and the Tsai-Wu tensor components are chosen accordingly.

Earlywood

For the earlywood cell the same procedure as for the latewood cell was carried out, which is why just the significant differences to the abovementioned steps will be discussed in the following.

a-c) Identification of failure mechanisms and assignment to crack directions

Figure 3.14 shows the identified failure mechanisms for the earlywood unit cell and Figure 3.15 the corresponding assignment to failure modes and crack directions. Failure mechanism ① finally leads to a ruptured cell wall, giving a global crack direction parallel to the R -direction. Failure mechanism ② shows cracked cell walls in the cell corners causing a crack direction in between the global R and the T -direction. The direction of crack (positive or negative angle with the R -direction) is again determined by the existing in-plane shear stress component τ_{RT} . The cracks in failure mechanism ④ are aligned parallel to the T -direction. Failure mechanisms ⑤ and ⑥ are mostly under compressive loading in T -direction. But, in contrast to the very stiff latewood cells, here the thin-walled features of the cell results in a skewing of the cell and, finally, a diagonal global crack direction in the RT -plane. For the failure mechanisms ⑦ and ⑧, where the cells are compressed due to loads in R -direction, a crack normal in R -direction is assigned. Again it has to be emphasized that in such a case the cracking behavior is of less importance, as in most cases other modeling approaches should be more suitable to describe the failure mechanisms.

d) Determination of failure surfaces

Figure 3.16 shows the resulting failure surfaces in the σ_R - σ_T plane. It has to be noted that the two failure surfaces [5] and [6] represent the same failure mode and crack direction, but two surfaces are more suitable to describe the simulation results in that region.

Figures 3.17 and 3.18 show the resulting failure surfaces in the shear stress planes and the σ_L - σ_R - σ_T stress space, respectively.

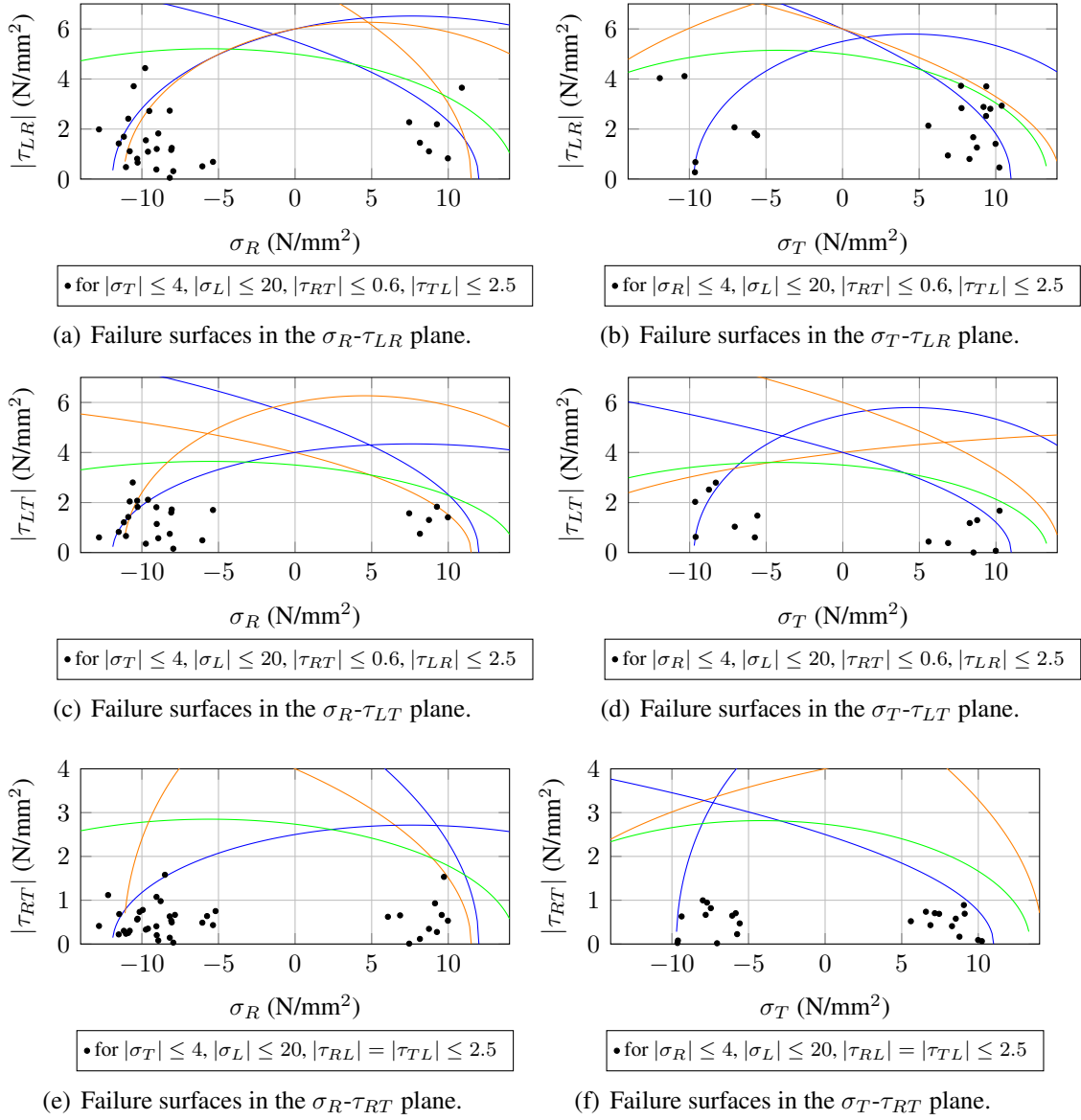


Figure 3.13: Failure surfaces for the latewood unit cell in several normal/shear-stress planes. The different colors denote different failure modes. The legends below the subplots denote the ranges in N/mm^2 for which stress states were considered in the determination process of the corresponding failure surface component.

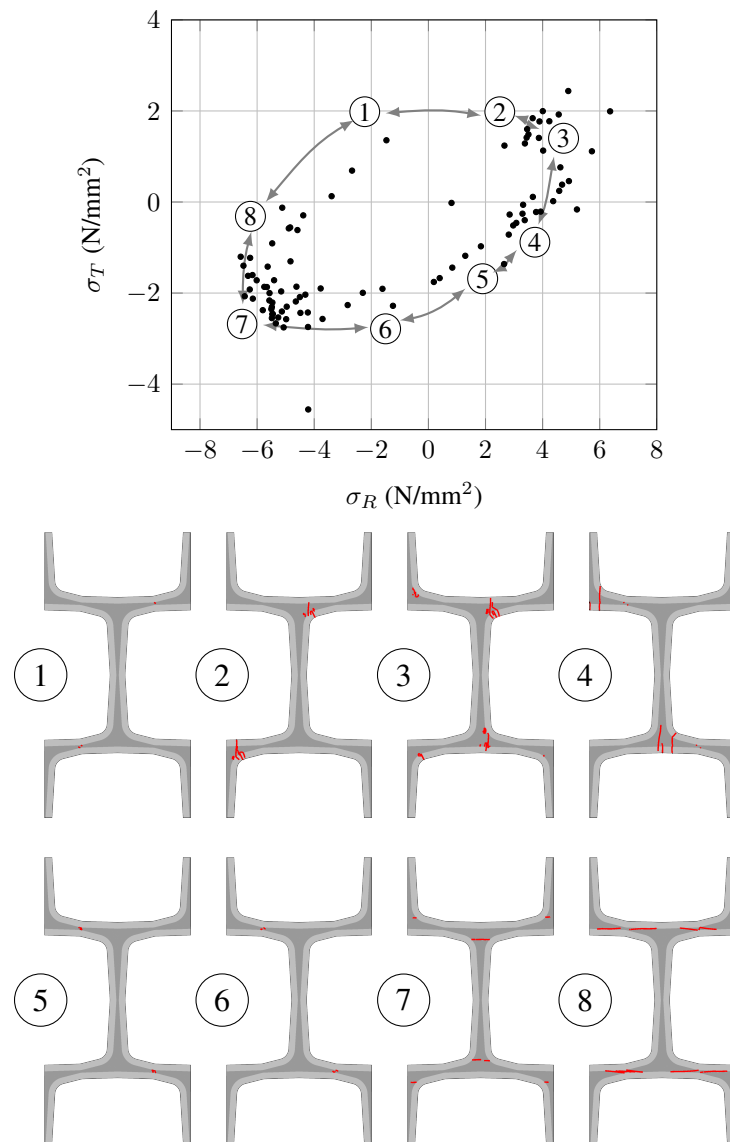


Figure 3.14: Obtained failure modes for the earlywood unit cell identified in the σ_R - σ_T plane. The different colors denote different failure modes. Failure stress states with $\tau_{RT} > 0.3\text{N/mm}^2$, $\tau_{RL} = \tau_{TL} > 1.0\text{N/mm}^2$ or $\sigma_L < -10$ and $\sigma_L > 10$, respectively, were excluded from plot.

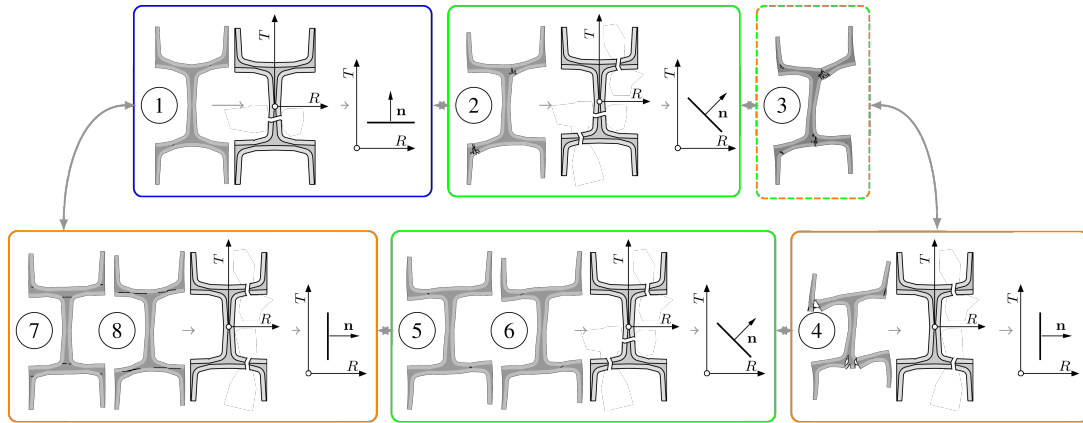


Figure 3.15: Classification of failure modes and crack directions, respectively, for the early-wood unit cells.

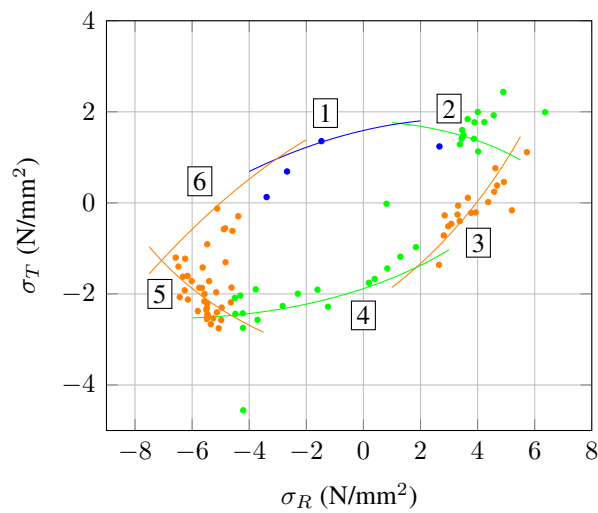


Figure 3.16: Failure surfaces for the early-wood unit cell in the σ_R - σ_T plane. The different colors denote different failure modes. Failure stress states with $\tau_{RT} > 0.3 \text{ N/mm}^2$, $\tau_{RL} = \tau_{TL} > 1.0 \text{ N/mm}^2$ or $\sigma_L < -10$ and $\sigma_L > 10$, respectively, were excluded from the determination of the failure surfaces in the σ_R - σ_T plane.

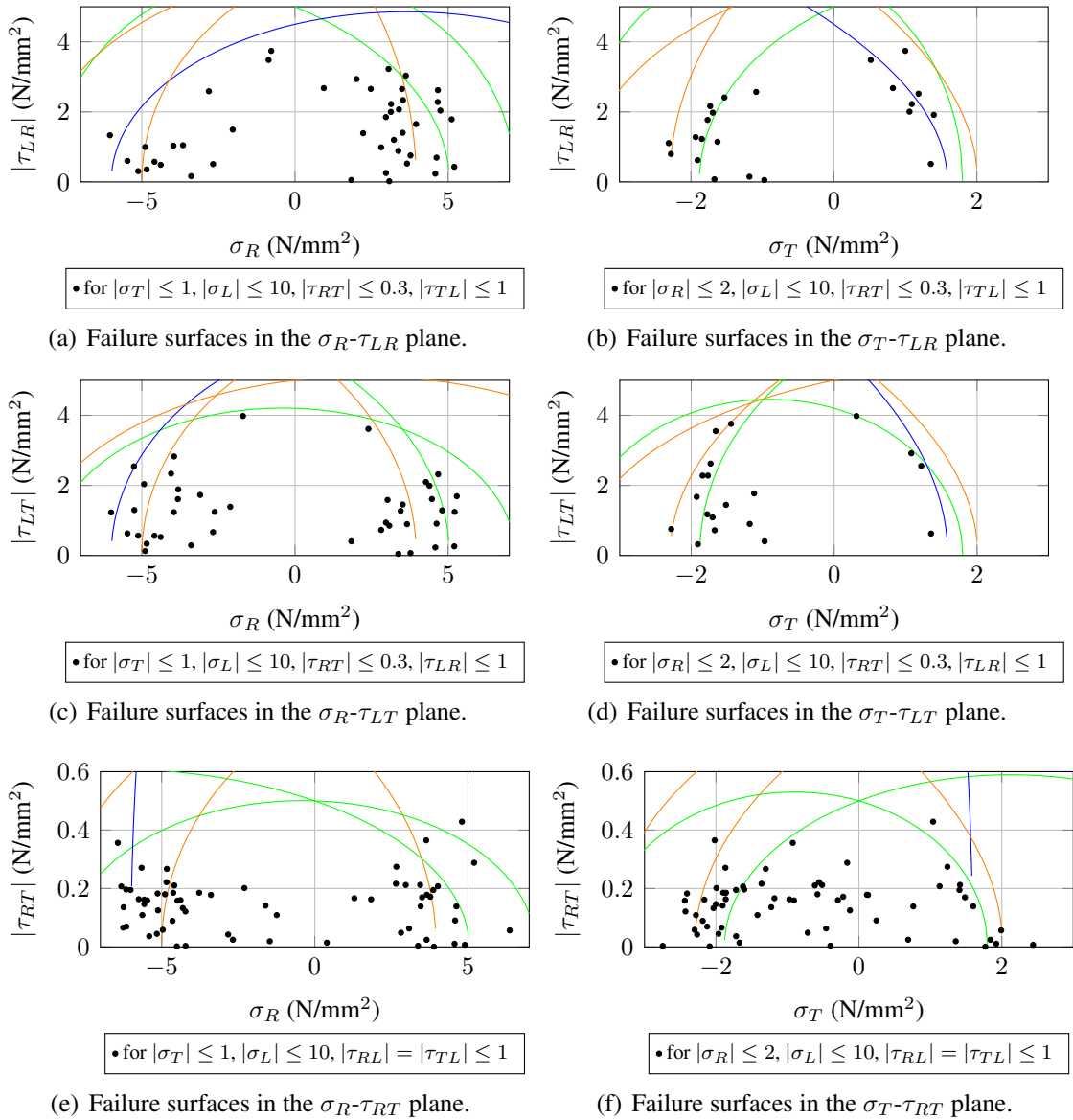


Figure 3.17: Failure surfaces for the earlywood unit cell in several normal/shear-stress planes. The different colors denote different failure modes. The legends below the subplots denote the ranges in N/mm^2 for which stress states were considered in the determination process of the corresponding failure surface component.

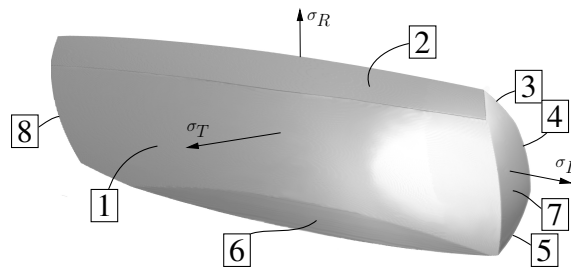


Figure 3.18: 3D representation of the earlywood failure surfaces in the σ_L - σ_R - σ_T stress space with the shear stresses being equal to zero ($\tau_{LR} = \tau_{LT} = \tau_{RT} = 0$).

3.5 Application to annual ring scale

The derived multisurface failure criterion is now applied to the annual year ring scale. This means that the two layers, earlywood and latewood, are both modeled homogeneously, with the newly obtained failure surfaces (see Figures 3.12 and 3.18) describing all failure mechanisms and crack directions at each layer.

3.5.1 Method

Dill-Langer et al. (2002) and Wittel et al. (2005) conducted uniaxial tensile tests on spruce specimens in the RT -plane. The experimental setup with cell dimension is shown in Figure 3.19. Three different fiber to loading orientations were investigated, and each specimen had an initial notch at the top border to control the position of crack initiation. The three configurations are denoted as follows: the first letter describes the growth direction parallel to the load axis and the second letter the direction of the initial notch (see Figure 3.19).

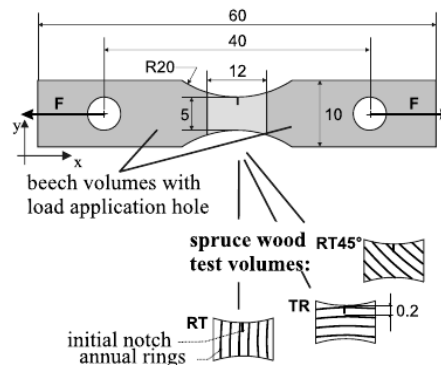


Figure 3.19: Experimental setup for the tensile test (Wittel et al., 2005)¹.

¹Reprinted from Computational Materials Science, 32(3–4), Wittel F, Dill-Langer G, Kröplin BH, Modeling of damage evolution in soft-wood perpendicular to grain by means of a discrete element approach, 594–603, 2005, with permission from Elsevier

3.5.2 Comparison of simulation and experimental results

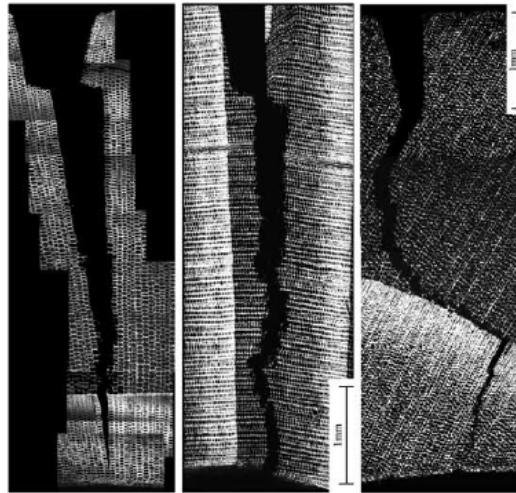


Figure 3.20: Crack patterns obtained by experiments (configurations from left to right: TR, RT and RT45°) (Wittel et al., 2005)¹.

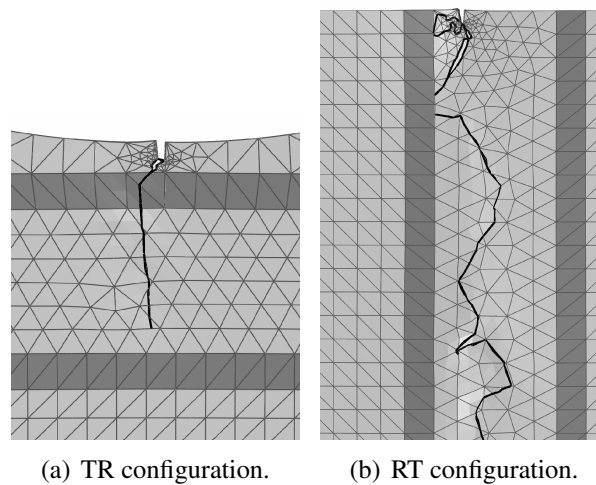


Figure 3.21: Simulation results for specimens in TR and RT configurations, respectively.

Figure 3.20 shows the crack patterns obtained by the experiments for the three described configurations. The failure mechanisms, which were already described in the previous sections, can also be identified here. The failure mechanism in the TR configuration is mainly cell wall peeling, leading to a linear crack parallel to the global R -direction. The same effect was obtained from simulation as can be seen in Figure 3.21(a). For the RT configuration the crack follows a zig-zag path, which is due to the predominant failure mechanism: cell wall rupture within the weaker earlywood layer. This effect can also be seen in both the experiment (Figure 3.20 middle) and the simulation (Figure 3.21(b)). Finally, the third configuration, with an fiber to loading

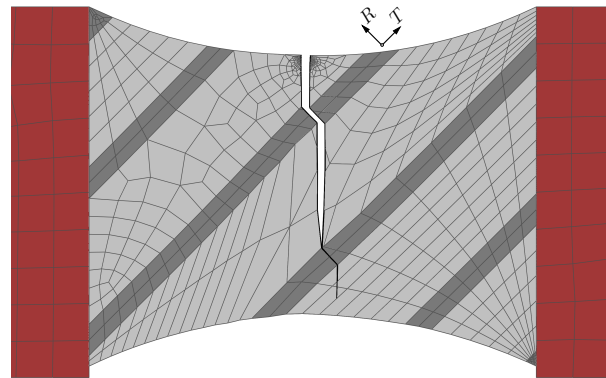


Figure 3.22: Simulation results for specimens with a RT45° configuration.

angle of 45° to the load axis, exhibits a mixed cracking behavior of the first two configurations. Within the earlywood the crack path is approximately normal to the loading direction, whereas within the latewood the crack path changes direction and is normal to the layered structure, which can be explained by the thick-walled and stiffer cells of this layer leading to a cell wall peeling within the middle lamella. Even this behavior can be reproduced very well by the developed model (see Figure 3.22).

In summary, it can be noted that the failure mechanisms found in the experiments of Dill-Langer et al. (2002) and Wittel et al. (2005) can be reproduced very well by the newly developed multisurface failure criteria for late- and earlywood.

3.6 Conclusions and outlook

The failure mechanisms of the clear wood layers, namely late- and earlywood, were identified at the wood cell level by using an approach based on the XFEM. Therefore, failure criteria for the two governing materials at this level, the middle lamella and the cell wall, were derived and implemented into a unit cell model, which is able to describe the repetitive, honeycomb-like structure of the wood cells. By using sampling techniques, a total of 800 load combinations were obtained for each of the two cell types, covering the entire stress space with all possible failure mechanisms. A classification of the resulting failure mechanisms enabled the determination of failure surfaces for each failure mode, to which a corresponding global crack direction was assigned to.

The two resulting multisurface criteria for the two cell types were finally applied to tensile tests at the annual year ring scale. The simulation results showed very good agreement for the obtained failure mechanisms compared to experiments.

In general, the derived multisurface criteria in combination with XFEM lead to a powerful tool for the description of crack initiation and direction, which can also be applied to complex stress states, where similar approaches reach their limits. Especially, the future implementation of plastic behavior for the failure surfaces, which are mostly under compression, should improve the performance of this simulation tool even further.

Thus, consequentially the next step is the homogenization of the results for the two layers to a single multisurface failure criterion at the clear wood level. By applying the same techniques used within this work, namely the unit cell method and a big sample of loading combinations in the framework of XFEM, this approach is pretty straightforward. The resulting crack initiation criterion will be implemented into an existing numerical simulation tool for wooden boards with a mathematical model for the description of the fiber course in the vicinity of knots (Lukacevic and Füssl, 2014; Lukacevic et al., 2014a). This enables the realistic simulation of failure mechanisms of wooden boards with knots and in a next step of wood products, like Cross-Laminated Timber or Glued Laminated Timber.

Discussion of common and introduction of new indicating properties for the strength grading of wooden boards (Lukacevic et al., 2014c)

Authored by Markus Lukacevic, Josef Füssl and Josef Eberhardsteiner

Submitted to *Wood Science and Technology*, 2014

The naturally grown material wood exhibits, in addition to its orthotropic material structure, several types of inhomogeneities, where most of them can be allocated to knots and the resulting local fiber deviations. Since these generally lead to a reduction of strength properties, wooden boards must be subjected to a grading process before they can be used as load-bearing elements. Within this process so-called indicating properties are recorded and used to assess the wooden board strength.

Common indicating properties are almost exclusively based on surface information of wooden boards while the 3D position and orientation of knots within a board is hardly considered. Thus, algorithms for the 3D reconstruction of wooden boards based on already available surface scans, laser scanning, X-ray or computer tomography data are assessed first within this work. This new knot information allows then the development of novel indicating properties, which consider the knots, the resulting fiber deviation regions and, for bending conditions, the knot location information by using height dependent weighting functions.

The statistical evaluation of combinations of the new indicating properties, separately for tensile and bending load conditions, shows that the correlations to experimentally obtained strength properties could be improved significantly with such an approach.

Nomenclature

KAR	knot area ratio
FAR	fiber deviation area ratio
CAR	clear wood area ratio
S	knot surfaces visible on board surface
S_b	knot surfaces on bottom surface (closest to pith for tensile and tensile surface for edgewise loading)
S_t	knot surfaces on top surface
S_l	knot surfaces on left surface
S_r	knot surfaces on right surface
S_{tb}	knot surfaces on top and bottom surfaces
S_{lr}	knot surfaces on left and right surfaces
S_{lr}^-	knot surfaces on left and right surfaces below neutral axis (tensile loaded half)
I	interface between knots and surrounding clear wood
V	knot volume
h_p	normal distance to pith in tensile loaded boards
h	distance from top surface to weighted face/volume in edgewise loaded boards
X^L	linearly weighted face/volume (from top to bottom)
$X^{\bar{L}}$	linearly weighted face/volume (from neutral axis to bottom)
X^Q	quadratically weighted face/volume (from top to bottom)
$X^{\bar{Q}}$	quadratically weighted face/volume (from neutral axis to bottom)

4.1 Introduction

Compared to other building materials, like steel or concrete, wood is a naturally grown material, and therefore exhibits a less homogeneous material structure. Not only varying material properties of the so-called clear wood, caused for example by varying density or moisture content, but also inhomogeneities like knots influence the strength and stiffness properties of timber elements. Knots and the resulting fiber deviations in their vicinity have the greatest impact on the structural behavior of wooden boards, as in most destructive bending or tension tests, failure is caused either by knots themselves or by cut fibers due to local slope of grain in their vicinities (Johansson, 2003). At a constant clear wood strength, a single critical knot may reduce the effective bending strength of a timber board up to 75 %. Thus, to ensure certain strength properties of timber boards,

which are intended for use as load-bearing elements, reliable identification and evaluation procedures are necessary. These are summarized under the term strength grading, and the most popular ones are presented in the following.

4.1.1 State of the art

In principle, two different methods of strength grading can be distinguished: manual strength grading, in which knots and growth irregularities are identified visually and the strength reduction is estimated by the inspector by means of visual grading standards, and automated strength grading, where a machine is used to measure non-destructive indicating parameters (IP), which are correlated to the bending strength. The basis for the categorization of wooden boards is the European Standard DIN EN 338 (2013), which introduces 12 strength classes of sawn softwood timber (C14 to C50). These so-called C-classes are defined according to the edgewise bending strength in N/mm^2 , which emphasizes that edgewise bending is the most important loading mode in structural use of sawn timber. All other strength values, e.g. the tensile strength, are correlated to the edgewise bending strength (Hanhijärvi et al., 2005). Furthermore, these characteristic bending strengths refer to specific board dimensions and test setups. Conversion factors for deviating conditions can be found in DIN EN 384 (2013).

In Europe, visual grading of structural timber is still highly used. To account for local differences, e.g. growth conditions, national standards, like the DIN 4074-1 (2012) for Germany and Austria, are employed. The different grading rules are almost all based on parameters of knot measurements, which can be the minimum knot diameter, the projected knot area on the end grain of the board, or the knot size measured parallel to the edge of the board. In addition, the arrangement of knots to each other (parameters of knot clusters) are considered. Naturally, visual grading methods exhibit a high level of inaccuracy and together with the inability to consider the mass density visually, the highest strength class, which can be reached by the DIN standard, is S13, which corresponds to C30. Blaß and Frese (2004) expanded these approaches, based on knot parameters, by using an additional mechanical acquisition of the boards' dimensions, density and dynamic modulus of elasticity (MOE). Through multiple linear regression analyses, they showed that by a combination of simple grading techniques, the higher strength class C35 could be reached. Johansson et al. (1992) compared the grading results of German and Swedish spruce specimens, which were tested in bending (255 pieces) and tension (245 pieces), of several standards. The achieved bending strength of the boards graded to strength class S13, which is in accordance with a characteristic bending strength of 30 N/mm^2 , was 36.9 N/mm^2 and, thus, significantly higher than the expected value. Further, they studied the potential of different knot measurements in combination with machine grading to increase the precision of strength predictions. Stapel and van de Kuilen (2013a) investigated the validity of grading standards for large growth areas and concluded that the rules of measuring knots and the number of grades in a standard influence the results. Further, they notice that allocations in DIN EN 1912 (2013), which give relationships of grades obtained by national standards to the strength classes of EN 338, are incorrect in many cases and should be reviewed. An examina-

tion of DIN 4074-1 by Stapel and van de Kuilen (2013b) regarding the influence of cross-sectional dimensions on the grade yields, showed a big influence of the boards' widths. Thus, they suggested revised threshold values for the visually graded strength classes, leading to easier grading rules and higher yields. Various research attempts have been made to find correlations between knot ratios and bending strengths. Piter et al. (2004a,b) introduced several versions of knot ratios and found a combined grading parameter including the boards' density and MOE for Argentinean *Eucalyptus grandis*. Roblot et al. (2010) automatically computed various versions of knot area ratios and reached coefficients of determination of up to $r^2 = 0.67$.

For machine-graded timber the European Standards DIN EN 14081-2 (2013) and DIN EN 14081-3 (2012) are used, defining the requirements for initial machine testing and continuing production control. The simplest machine-grading method is the section wise measurement of a board's flatwise MOE. Such obtained MOE profiles over the board length can be used to find minimum values, which are correlated to the board's edgewise MOE and, subsequently, to the edgewise bending strength. This approach has several deficiencies, for example Johansson et al. (1992) found a coefficient of determination of $r^2 = 0.66$ between machine-obtained MOE and edgewise MOE. Steffen et al. (1997) and Samson and Blanchet (1992) showed that the effect of knots on the flatwise bending stiffness is rather small. In contrast and as already mentioned, it is well-known that knots and the resulting fiber deviations strongly influence the mechanical behavior of timber elements, especially the edgewise bending strength (Johansson, 2003). This discrepancy can be explained by different dependencies on shear deformation, knots and the natural variation of MOE over the timber cross section. Steffen et al. (1997) concluded that further research should be focused on the effect of knots on strength properties as it may differ distinctly from the influence on MOE. Hanhijärvi and Ranta-Maunus (2008) tested 1000 pieces of spruce and 1000 pieces of pine in a large test series and compared several non-destructive IPs: X-ray scanning, frequency measurement and ultrasonic transit time of logs, visual scan of board sides, natural frequency measurement, X-ray scanning and acoustic-ultrasonic measurement of boards, density measurement by scale, flatwise bending stiffness and manual knot measurements. They came to the conclusion that a large part of timber boards could reach higher strength classes with more accurate strength grading systems, which would lead to a better utilization of the structural potential. Ranta-Maunus et al. (2011) tested 6226 samples, where 75% were spruce specimens and a total of 2723 of those were tested in bending, with the specimens coming from several countries, resulting in correlation matrices for those countries and an IP based on dynamic MOE and knot area ratio. Petersson (2010a,b) showed the promising potential utilization of modern scanning techniques in respect of knot locations and corresponding fiber deviations in their vicinities by means of laser scanning results for wood surfaces and end surfaces of both boards and laminated beams. Olsson et al. (2013) also used modern high resolution laser scanners to calculate the variation of the local MOE over the boards' length and defined a new IP as the lowest bending stiffness determined along the board. Olsson et al. (2012) investigated the potential of dynamic excitation measurements for the prediction of the bending strength of wooden boards. By taking into account higher bending modes, and thus the boards' inhom-

geneities, they were able to increase the coefficient of determination to 0.75. Hu et al. (2011) tried to locate imperfections in sawn timber based on flexural mode shapes by using both FE modeling and experimental studies, but concluded that the method was too sensitive to measurement errors. Lei et al. (2005) related lumber MOE and modulus of rupture (MOR) to stand/tree characteristics and results from vibration tests for black spruce. Castera et al. (1996) studied the efficiency of statistical models for grading and design purposes. They used the statistical modeling of beam strength from correlation models to simulate grading procedures for various populations of maritime pine lumber.

Table 4.1: Coefficients of determination r^2 between several indicating properties and edgewise bending strength found by various research studies.

<i>Static MOE</i>	
Johansson et al. (1992)	0.49-0.55
Larsson et al. (1998)	0.47-0.61
Steiger and Arnold (2009)	0.43
Olsson et al. (2012)	0.72
Castera et al. (1996)	0.60
Lei et al. (2005)	0.71
Ranta-Maunus et al. (2011)	0.66
<i>Dynamic MOE</i>	
Divos and Kiss (2010)	0.69
Larsson et al. (1998)	0.42-0.63
<i>Density</i>	
Larsson et al. (1998)	0.26
Olsson et al. (2012)	0.27
Ranta-Maunus et al. (2011)	0.28
<i>Knot measurements</i>	
Johansson et al. (1992)	0.26-0.35
Castera et al. (1996)	0.43
Glos and Burger (1998)	0.31
Roblot et al. (2010)	0.67
<i>Combinations of above and other IPs</i>	
Johansson et al. (1992)	0.59
Olsson et al. (2013)	0.68-0.71
Olsson et al. (2012)	0.75
Glos and Burger (1998)	0.58
Ranta-Maunus et al. (2011)	0.63

Due to the high variability in timber, EN 14081 requires the testing of at least 900 specimens for the acceptance of a new strength grading machine. That means, that the

whole test sample must be tested destructively, leading to high costs for the implementation of new grading techniques.

Table 4.1 shows an overview of coefficients of determination r^2 between several IPs and the edgewise bending strength, which could be achieved in the research studies discussed above. It can be seen that MOE, and, especially, density and several types of knot measurements by themselves are often not able to reliably predict the bending strength. Combinations of multiple single IPs and other more sophisticated IPs do reach higher correlations, but still have room for improvement.

4.1.2 Motivation

All grading techniques mentioned before, like visual inspection or empirical correlations between effective properties and different knot parameters, are based on surface information of timber boards. For this reason, the real anatomy and the spatial position as well as orientation of knots is either not considered or approximated roughly. Since there is a trend to capturing 3D geometrical information of timber boards, e.g. by computer tomography, relations between effective properties and 3D indicating properties are getting more interesting, and could improve future grading procedures dramatically. This motivated the following work, in which the 3D geometry of knots in timber boards is reconstructed and used to determine different novel indicating properties. By means of tensile and bending tests up to failure of the corresponding timber boards these IPs were compared to conventional properties and their performance could be assessed. As better grading rules can be achieved, if the rules are developed individually for each specimen (Hanhijärvi et al., 2005), within this work only spruce is investigated.

Within the next section (Section 4.2), the experimental setup and the material used in two tensile and three four-point bending test series with varying dimensions are presented. To obtain the 3D knot informations, two methods for the geometrical reconstruction of the test specimens are proposed in Section 4.3. The former one is based on a manual acquisition of knot data to reduce reconstruction inaccuracies in the development process for novel indicating properties, and the latter one is an automatic reconstruction algorithm based on laser scanning data of the boards' surfaces in combination with X-ray data. In addition, an overview of possible other methods for obtaining such 3D informations is given. Using 3D morphological knot information as input to novel indicating properties is motivated by new developments in the field of high speed grading machines utilizing for example computed tomography for logs and resulting in high quality 3D knot information.

In Sections 4.4 and 4.5, existing indicating properties are evaluated with regard to their reliability to predict strength properties, before new indicating properties for both tensile and edgewise bending strength are proposed. The latter ones are based on height distance weighted finite knot volumes, knot/clear wood interfaces and knot surfaces, as by this means, the effect that a knot is more dangerous the closer it is situated towards the tension side and fibers in its vicinity are cut at this edge, respectively, can be accounted for. Combinations of several indicating properties are investigated by means of multiple linear regression analyses.

Finally, a brief summary and concluding remarks are given in Section 4.6.

4.2 Experiments

4.2.1 Selection of material

As already mentioned, all samples were prepared of Norway spruce (*Picea abies*). Table 4.2 shows an overview of the investigated wooden boards including the corresponding type of load.

Table 4.2: Overview of the evaluated test series with the boards' dimensions.

Series	# of tests	Section [mm]	Load type
1	14	80/40	tension
2	15	80/40	tension
3	10	144/45	bending
4	8	189/45	bending
5	25	40/115,145,185	bending

Test series 1 and 2 have been conducted by an Austrian wood processing company. These samples and the ones of test series 3 and 4, which were tested at *Holzforschung Austria* (Vienna), were also used for the stiffness validation of the numerical simulation tool for wood grading in Hackspiel (2010). Test series 5 was carried out at the laboratory of the Research Center of Building Materials, Material Technology and Fire Safety Science of the Vienna University of Technology (11 specimens) and at the Laboratory for Macroscopic Material Testing of the Institute for Mechanics of Materials and Structures (IMWS) of the Vienna University of Technology (14 specimens). The boards of the last test series were selected so that significant knots are located in the area of the maximum moment in four-point bending tests, which is the worst possible configuration. Furthermore, single knots/knot groups should be situated in the center third of the board length and should especially be avoided close to the load application points. In this way, structural failure can easily be assigned to a single knot or knot group, respectively. For all specimens, sample disks were cut out of clear-wood sections, i.e. sections with no knots and no fiber deviations caused by them. These disks were weighed, dried at 105 °C and weighed again, to obtain the corresponding clear-wood density ρ_{cw} and the moisture content u for each board.

4.2.2 Four-point bending tests

The edgewise bending strength and the MOE, respectively, were obtained by subjecting the specimens to edgewise four-point bending tests according to DIN EN 408 (2010b). Figure 4.1 shows the experimental setup for test series 5, conducted at the IMWS, where

a triaxial servo-hydraulic testing machine manufactured by Walter & Bai, with built-in load cells for a maximum load of 250 kN and 10 kN, respectively, an 0 to 110 mm encoder and computer assisted analysis, was used.

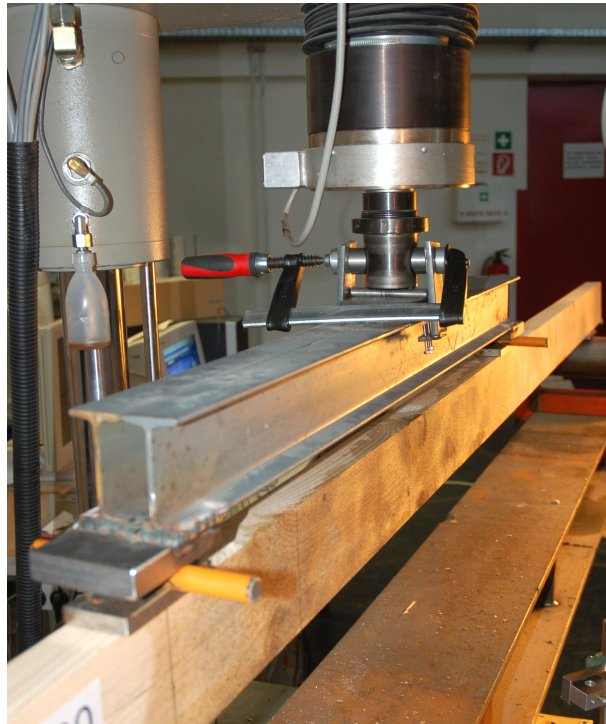


Figure 4.1: Experimental setup at the Laboratory for Macroscopic Material Testing.

The tests were performed displacement-driven, using the machine's 250 kN load cell. The load was distributed to the two load application points by a steel girder. Steel cylinders, serving as a roller bearing, with a diameter of 10 mm were placed between the girder and small steel plates, which avoid local indentations on the specimen. The loading rate was fixed at 20 mm/min and testing stopped as soon as the specimen collapsed. For every single test, a load-displacement curve up to failure was recorded and the tests were documented in detail with pictures and/or videos.

4.3 Geometrical reconstruction of test specimens

In order to link both the knot areas on the surfaces of wooden boards and the spatial position and orientation of knots themselves to the tensile or the edgewise bending strength, 3D information of knots is needed. This can be achieved by approximating knots with rotationally symmetric cones, using surface information from all four sides of the boards.

Subsequently, these truncated cones are then used for the evaluation of common and development of novel indicating properties for strength grading.

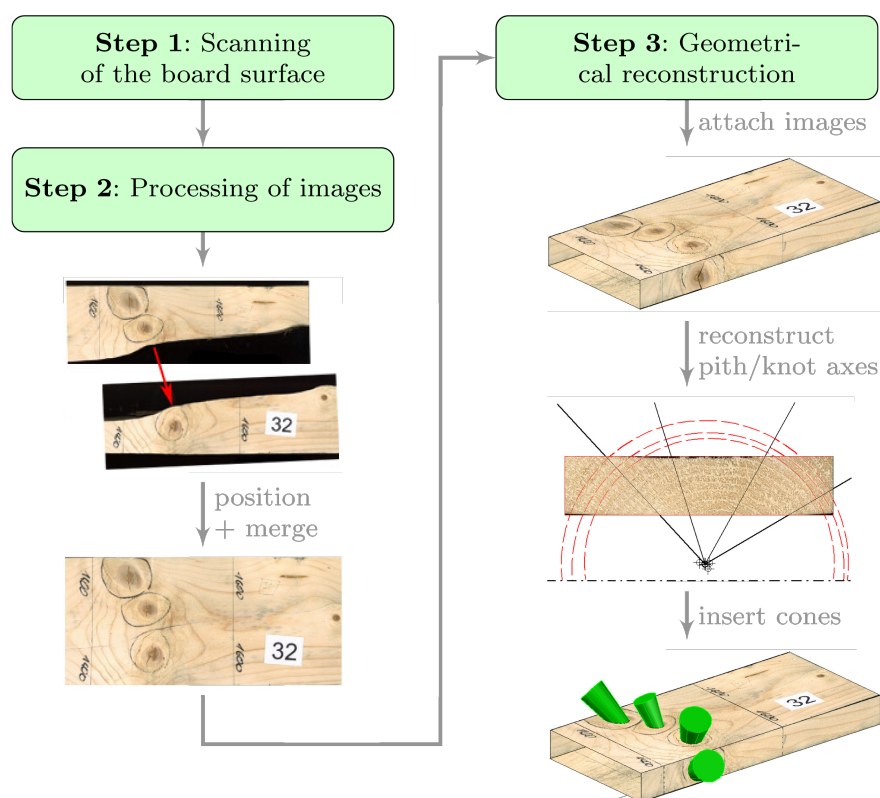


Figure 4.2: Flowchart illustrating the manual three-dimensional reconstruction process of the geometry of the tested boards (Lukacevic and Füssl, 2014).

4.3.1 Manual reconstruction

In order to obtain reliable geometrical information for the assessment of grading criteria, first, the test specimens were reconstructed manually. So, it could be ensured that the resulting geometry data for the knots is as accurate as possible. A detailed description of the manual reconstruction process is given in Lukacevic and Füssl (2014) and the flowchart, illustrating the reconstruction process of the geometry of the tested boards, can be found in Figure 4.2. Subsequently, the basics of this reconstruction process are summarized.

In a first step, the board surfaces of the knot sections, where failure originated during the experiments, were digitized with an A3 flatbed scanner. As all boards were tested up to failure, the scanned images had to be positioned and merged, before they were attached to a 3D model of the board in the computer-aided design software AutoCAD. For the reconstruction of the pith, at least two cross-section images, cut out of clear wood sections, were used. Circles were fitted into at least three annual year rings visible in these images. By connecting the arithmetic means of the resulting circle centers, a piecewise linear pith could be obtained.

As already mentioned, knots are approximated by rotationally symmetric cones, whose apexes lie on the linear pith. These cones are fitted manually into the knot sur-

faces visible on the boards' surfaces. For the case that the pith is located outside the board, each knot provides at least two sectional areas, which are used in the fitting process for an iterative reconstruction of the 3D geometry.

4.3.2 Automatic reconstruction

The manual reconstruction of knots is obviously not practicable in a high speed grading process. Thus, in the following automatic reconstruction algorithms, based on laser scanning and/or X-ray data and CT data, respectively, are presented.

Automatic reconstruction without exact pith location information

Within this work, for the automatic reconstruction of the tensile tested boards an algorithm, which was presented in Hackspiel (2010), was used and will be explained below.

Figure 4.3 shows a flowchart of this algorithm for the automatic 3D reconstruction of boards with no cross-section scans and, thus, without exact information about the pith location.

In a first step, all boards were subjected to a scanning process with a grading machine, which, by using laser scattering technique, resulted in polygon knot information for the four board surfaces and, in addition, X-ray data in the form of supplemental polygon information of the knots in the LT-plane, by using density information integrated over the board's thickness. If necessary, boards were flipped before scanning, so that the pith location was always close to or below the bottom surface, and for all boards the width coincided with the tangential material direction.

In the second step, the X-ray polygons were used to determine the pith location in the LT-plane. The according sketch in Figure 4.3 shows a board section with a total of seven knots in the LT-plane. Green filled polygons identify knots reaching one of the board's two lateral surfaces and blue filled polygons all other knots. It is now assumed that for all green filled polygons the points farthest from the corresponding lateral surfaces (marked red in the sketch) are the knots' apexes, whereas all blue filled polygons are neglected. Thus, to obtain the pith location in the LT-plane, a linear fit through all these marked points is performed.

Next, in step three, for all knot polygons lying on the top surface the knot cone heights z_i are calculated. Therefore, ellipses are fitted into the polygons by means of a least square fit. Due to poor scan polygon data, the ellipses' parameters had to be slightly modified. Once the ellipses are scaled and/or rotated, for each ellipse the intersection between the ellipse's major axis and the pith vector in the LT-plane was calculated, resulting in P_i , with l_i being the distance between the ellipse center and P_i on the top surface. Now, the knot cone's height z_i can be determined by

$$z_i = \frac{e_a}{\sqrt{e_a^2 - e_b^2}} \cdot \sqrt{l_i^2 - e_a^2 + e_b^2}, \quad (4.1)$$

with e_a and e_b denoting the major and minor axis of the ellipse, respectively, and C_i the knot cone's apex.

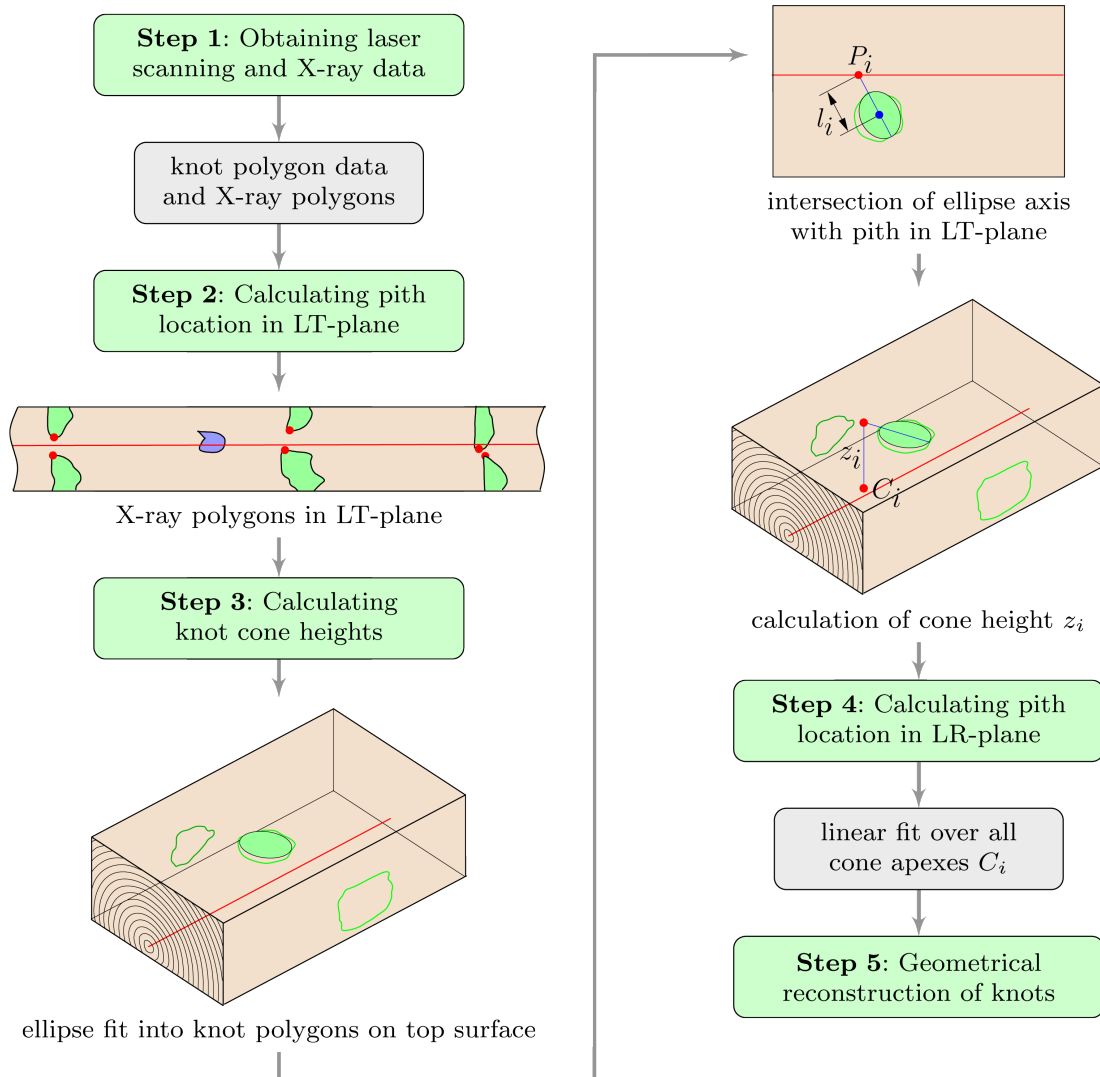


Figure 4.3: Flowchart illustrating the automatic 3D reconstruction process of the geometry of the tested boards in absence of front face scans with laser scanning and X-ray data.

Subsequently, a linear fit through all knot cone apexes C_i produces the final 3D pith vector. As the previously determined knot apexes don't lie on the fitted linear pith, the cone data has to be recalculated. For this another assumption was made, by setting the angle between pith and cone axis to a fixed value, which was found by taking the mean value of all knots found in 15 boards evaluated in Lukacevic (2009). With this constraint, the knot cone data, namely cone apexes, axes and apex angles, can be calculated.

Improved automatic reconstruction algorithms

Possible future improvements of the automatic reconstruction algorithm are for example the utilization of cross-section images. First investigations on such data showed that the annual year rings visible in such images can be used for a good approximation of the two-dimensional pith location. The approach would be the same as can be seen in Figure 4.2 for the manual determination of the pith location, and was accomplished by using Matlab's image processing tools.

Another method, already described in Hackspiel (2010), is the reconstruction based on CT images. In this investigation of this method, CT-images were taken every 5 mm along the length of the board with a resolution of 0.83 pixel/mm. Knot geometries were determined by analyzing density differences between knot and clear wood material.

The implementation of such methods in future wood grading machines at high speeds is feasible, as for example wood processing companies already introduced high-speed computed tomography for logs.

4.4 Indicating properties

In the wood grading process non-destructive indicating properties (IPs) are used to estimate strength properties of wooden boards. In the following, common IPs, which are mainly derived from knot area parameters on the board surfaces, and in this work newly developed IPs, including 3D information of knot geometry and position, are presented.

4.4.1 Common indicating properties

The German Standard DIN 4074-1 (2012), for the visual strength grading of coniferous sawn timber, accounts for knots by using a parameter called branchiness. Thereby, the maximum value of the smallest visible diameter of all knots or, for edge knots, its arch rise divided by the corresponding cross-sectional length determines the strength class of a wooden board under edgewise bending. For boards under flatwise bending or tension two branchiness factors, one for single knots and one for knot groups, are defined, where the sum of all knot dimensions parallel to the board's cross-section is divided by two times the board's width. For example, for the sample knot section in Figure 4.4 the branchiness for the knot group can be determined as

$$A = \frac{a_1 + a_2 + a_3 + a_4 + a_5}{2b}. \quad (4.2)$$

Thresholds for the branchiness are used to grade the boards into the according strength classes.

Another common IP is the so-called knot area ratio (*KAR*), which is usually defined as the total projected area of all knots within a knot section divided by the cross-sectional area. For the knots in Figure 4.4, the greenish area denotes the projected knot areas. The *KAR* can be specialized by only taking into account the knots in the outer quarters of a board to consider their higher effect on the edgewise bending strength.

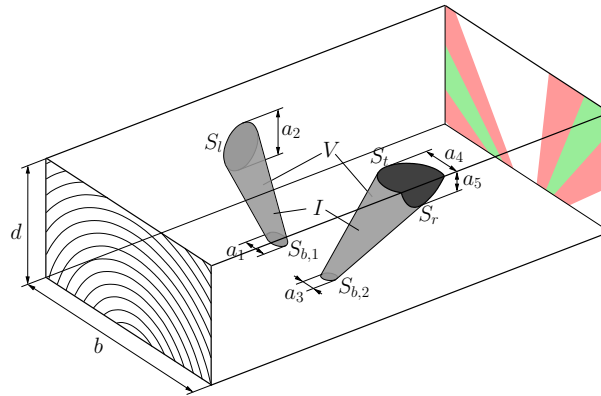


Figure 4.4: Designation of geometric parameters used for the calculation of indicating properties (greenish areas denote projected knot areas and reddish areas projected fiber deviation areas, respectively).

Furthermore, wood grading machines use various relationships of knot areas detectable on the four board surfaces (see S_l , S_r , S_t and S_b in Figure 4.4 for left, right, top and bottom knot surfaces, respectively) during the grading process. Knowledge about the exact implementation of such IPs is not available, but it can be assumed that mainly empirical correlations to strength properties are used.

4.4.2 Novel indicating properties

For the development of novel indicating properties, existing ones were modified and extended, and new approaches based on the now available 3D knot information were generated.

It can be assumed that the region, in which the fibers in the vicinity of a knot are deviated from the global longitudinal direction, is affected by the corresponding knot size. Thus, in Hackspiel (2010) and Lukacevic and Füssl (2014) these so-called fiber deviation regions for each knot were defined by another cone with the same apex and the same axis vector as the knot cone, but with a fourfold apex angle. By using this

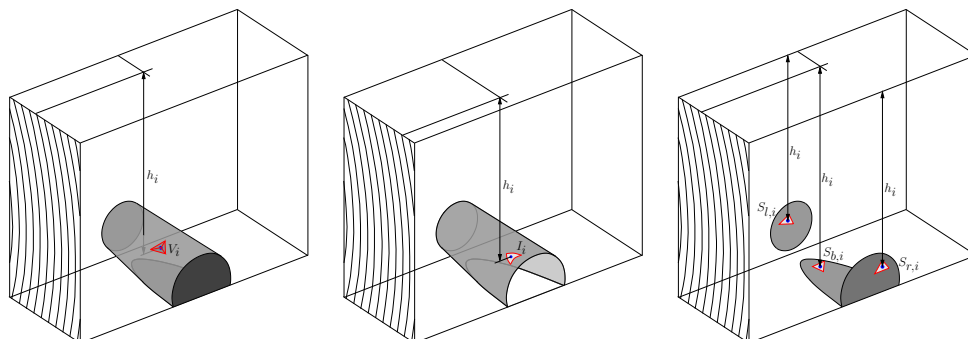


Figure 4.5: Illustration of distance h_i of finite volumes V_i (left), finite interfaces I_i (center) and finite surfaces S_i (right).

information, a so-called fiber deviation area ratio (FAR) on the basis of the KAR can be defined. The projection of the fiber deviation cones on the cross-section for a sample board can be seen in Figure 4.4 (reddish area) and the ratio is defined as the projection of the fiber deviation cone minus the projection of the knots divided by the cross-sectional area. Following the same approach, finally, a clear wood area ratio can be defined as

$$CAR = 1 - KAR - FAR. \quad (4.3)$$

The new area ratio CAR is a measure for the amount of undisturbed fibers within a cross-section, which are never deviated from their linear course, and, thus, could be a good addition to an IP, especially for tensile tested boards, as these fibers can transfer the tensile load most effectively.

The interface between knots and surrounding clear wood and the knot volume are used as additional IPs. For tensile tests the total interface and knot volume, respectively, are also some kind of measure for the disturbed zone.

IPs, presented so far, might be quite suitable for the prediction of the tensile strength, but they consider the position of the knot within the wooden board either not at all or insufficiently. Thus, in this work, the 3D information, obtained through the geometrical reconstruction should be utilized. Therefore, various weighting functions were defined:

$$w_i^L(h_i) = h_i/H \quad (4.4)$$

$$w_i^{\bar{L}}(h_i) = \begin{cases} \frac{h_i - H/2}{H/2} & \text{if } h_i > H/2 \\ 0 & \text{if } h_i \leq H/2 \end{cases} \quad (4.5)$$

$$w_i^Q(h_i) = (h_i/H)^2 \quad (4.6)$$

$$w_i^{\bar{Q}}(h_i) = \begin{cases} \left(\frac{h_i - H/2}{H/2}\right)^2 & \text{if } h_i > H/2 \\ 0 & \text{if } h_i \leq H/2 \end{cases} \quad (4.7)$$

where h_i is the distance of a finite area/volume to the top surface of the compression zone and H the height of the edgewise loaded board (see Figure 4.5). $w_i^L(h_i)$ and $w_i^{\bar{L}}(h_i)$ in Equations (4.4) and (4.5) describe linear weighting functions from zero at the top or at the neutral axis, respectively, to a value of one at the bottom (tensile zone). The quadratic weighting functions $w_i^Q(h_i)$ and $w_i^{\bar{Q}}(h_i)$ in (4.6) and (4.7) are defined analogously. This means that the closer a finite area/volume is situated towards the tensile loaded edge the higher its influence on the bending strength is assumed. For the two weighting functions denoted with a bar over the superscript, w becomes zero for all points lying in the upper half of the board, which is under compressive load in pure bending conditions. Additionally, due to the consideration of the board height H the size effect is taken into account and, thus, makes differing board heights comparable.

These weighting functions can now be applied to the knot surfaces $S_{l,i}$ and $S_{r,i}$ on the left (close to the pith) or right (close to the bark) board surface, the interfaces I_i between knots and clear wood and the knot volumes V_i . For example the total quadratically

weighted knot surfaces on the right board surface $S_r^{\bar{Q}}$ can be determined by

$$S_r^{\bar{Q}} = \sum_i S_{r,i} \cdot w_i^{\bar{Q}}(h_i). \quad (4.8)$$

4.5 Assessment of indicating properties

Within this section, IPs are evaluated with regard to their suitability to predict strength properties. First, for both tensile and edgewise bending tests common indicating properties are investigated and, by using selected sample boards, some drawbacks are demonstrated illustratively. Next, newly introduced IPs are combined by statistical means and compared to the results of common IPs.

4.5.1 Evaluation of common indicating properties

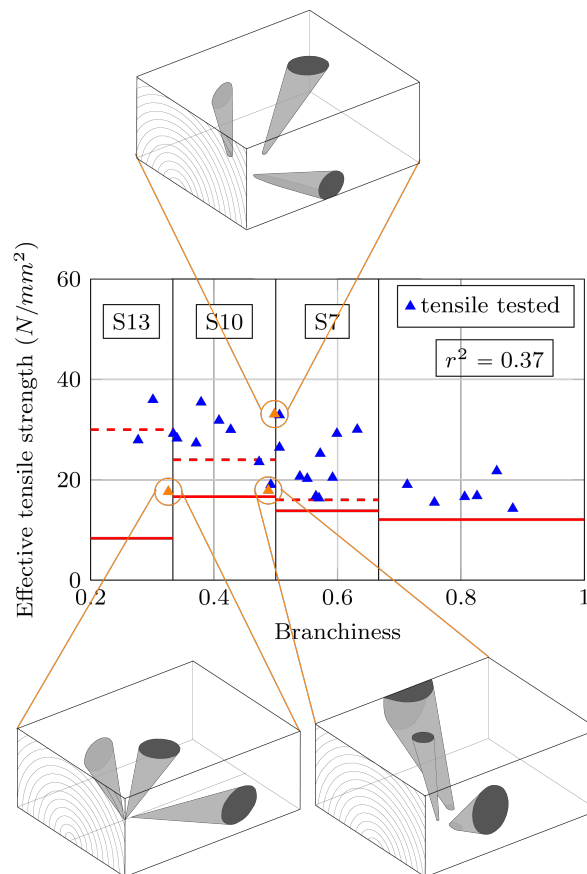


Figure 4.6: Correlation between effective tensile strength and total branchiness for the manually reconstructed boards. The columns indicate the grading classes according to the branchiness (Experimental: — 5% fractile; EN 338: - - - $f_{m,k} \hat{=} 5\%$ fractile).

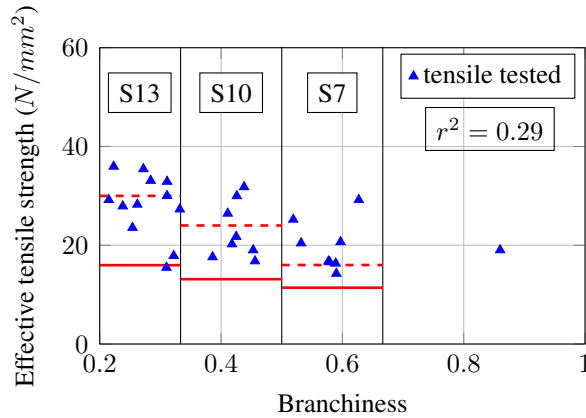


Figure 4.7: Correlation between effective tensile strength and total branchiness for the automatically reconstructed boards. The columns indicate the grading classes according to the branchiness (Experimental: — 5 % fractile; EN 338: - - - $f_{m,k} \hat{=} 5\%$ fractile).

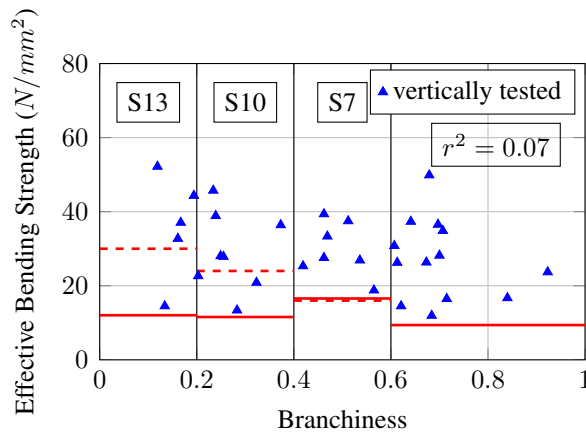


Figure 4.8: Correlation between effective bending strength and branchiness. The columns indicate the grading classes according to the branchiness (Experimental: — 5 % fractile; EN 338: - - - $f_{m,k} \hat{=} 5\%$ fractile) (Griessner, 2013).

Figures 4.6 and 4.7 show the correlations between effective strengths and the branchiness according to DIN 4074-1 (2012) for manually and automatically reconstructed boards of the tensile test series, and Figure 4.8 for the bending tests. The vertical lines show the thresholds for the allocation into the strength classes S7 to S13. The dashed, horizontal lines depict the characteristic strength values according to DIN EN 338 (2013), which comply with 5 % fractiles. The solid, horizontal lines are the actual 5 % fractiles of the test samples lying in the same strength class, which were determined according to DIN EN 14358 (2013):

$$f = \exp(\mu - k(n) \cdot \sigma), \tag{4.9}$$

with μ and σ being mean and standard deviation, respectively, and $k(n)$ a correction value, which is a function of the sample size n . It can be clearly seen that the experimentally obtained fractiles do not match the strength values defined in the European

Standard, but are in most cases significantly lower. Moreover, in Figure 4.8 the experiments don't even reflect the decreasing trend of the characteristic bending strengths $f_{m,k}$. Additionally, according to the branchiness, a considerable amount of boards does not fulfill the minimum requirements for grading class S7 and, thus, would have to be discarded, although high strength values in the edgewise bending tests could be reached.

The illustration of selected knot groups in Figure 4.6 should help to explain the inability of the branchiness to describe the influence of the knot position on the tensile strength. The knot group at the bottom left shows three moderately sized knots, which yield a good branchiness value of 0.326 but nevertheless a rather low strength of 17.62 N/mm^2 . This can be explained as follows, by keeping the 3D fiber flow in mind: since all three knot apexes lie close to the bottom surface, they are just not generating a knot area on the bottom surface, which would increase the branchiness, but at the same time disturb the longitudinal grain direction immediately under the surface. This effect is further enhanced as all three knots extend transversely through the board. Thus, only very few fibers can transfer the tensile stresses through the knot section undisturbedly, as most fibers are cut at the board's surfaces due to the resulting fiber deviations. These cut fibers are potential starting points of cracking. The knot group depicted in Figure 4.6 on the bottom right shows a configuration with a higher branchiness factor due to bigger knot dimensions. Nevertheless, in the corresponding tensile test a similar tensile strength could be reached. Compared to the first knot group, here the knot, reaching the top left edge, still enables some fibers on the bottom left to transfer the stresses unobstructedly. A knot group with almost the same branchiness factor but a significantly higher strength value is depicted at the top of Figure 4.6. At first glance, this knot configuration is similar to the first group, but on closer inspection it can be noticed that the knot reaching the right surface is cut along the whole length at the bottom surface, which results in the high branchiness factor. Further, the knot on the left has rather small dimensions and the knot apexes are further apart, which leads to much smaller zones of deviated fibers, and thus less discontinuities and better stress transfer capabilities. These examples clearly show that IPs based directly on surface information are not able to capture geometry induced strength fluctuations. The course of the knot within the board must be considered, which is partially true for the knot area ratio (KAR).

The correlation between the KAR and the manually and automatically reconstructed boards of the tensile tests is already higher than for the branchiness ($r^2 = 0.62$ and 0.43 , respectively), and shows a clear and expected trend. A smaller KAR leads to higher strengths and also the three chosen test samples, depicted in the sketches of Figure 4.6 and marked in Figure 4.9, are much closer to the regression line.

In contrast, the coefficient of determination between the KAR and the edgewise bending strength is just 0.25 (see Figure 4.11). This is mostly caused by the inability of this IP to describe the knot location within the board. Thus, the same knot located either in the compression zone or tensile zone lead to exactly the same KAR value. To explain this effect, three selected knot groups of tested specimens can be found in Figure 4.11. In addition, it should be kept in mind that all knot sections are taken from the center third of wooden boards loaded under four-point bending. Because of this, it can be assumed that these sections are mostly under pure bending, with the highest

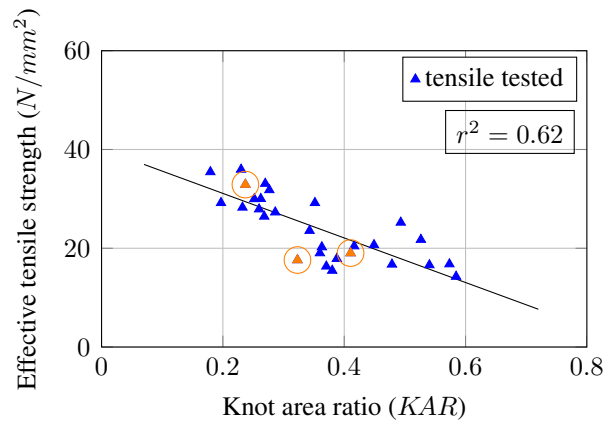


Figure 4.9: Correlation between effective tensile strength and KAR for the manually reconstructed boards.

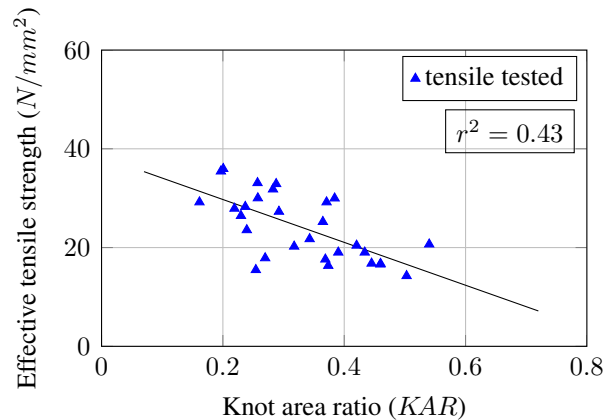


Figure 4.10: Correlation between effective tensile strength and KAR for the automatically reconstructed boards.

compressive stresses at the top and highest tensile stresses at the bottom, respectively. As the low tensile strength, especially in perpendicular-to-grain direction, of wood is predominantly the cause for crack initiation, special focus is laid on the lower parts of the investigated sections. The left group shows a knot section with three knots, where two of them lie in the compression zone or close to the neutral axis, respectively, and just parts of the third one in the tensile zone, as this knot is a splay knot. This leaves a lot of undisturbed fibers in the tensile zone of the board, resulting in a high bending strength. The middle group shows two knots, with one situated close to the top surface and one starting at the neutral axis and reaching the lower left edge. Thus, especially close to the lower right edge, the absence of big fiber deviations allows a good stress transfer in the highest loaded part of the board, so that a relatively high bending strength could be reached, although the KAR value is almost three times the one of the first knot section. The next section, depicted in the right sketch, shows four knots, with two of them in the critical part of the board. As both of these knots reach the bottom

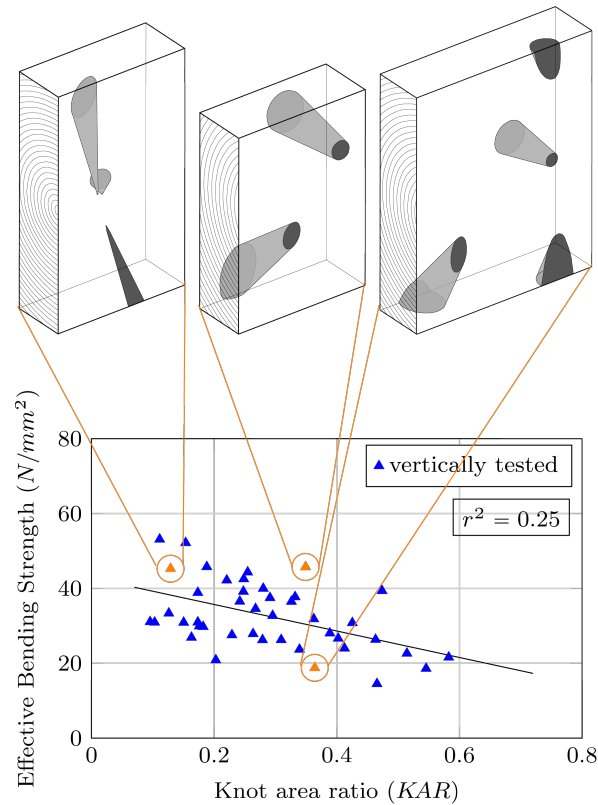


Figure 4.11: Correlation between effective edgewise bending strength and KAR .

surface, they cause a high amount of fiber deviations, which leads to a lot of cut fibers at the highest loaded surface. Due to this fiber deviations, these cut fibers are loaded in perpendicular-to-grain direction, which results in the low bending strength of the tested board, although the corresponding KAR value is almost the same as for the previously discussed board, which reached more than double the bending strength. Hence, even if the KAR value is able to capture strength fluctuations under pure tension moderately, the prediction of bending strength needs further IPs.

4.5.2 Evaluation of novel indicating properties

The novel IPs, which were presented in Section 4.4.2, try to overcome some of the shortcomings of the common IPs by considering the failure triggering effect of the knot location and also of the resulting fiber deviations in the vicinities of knots in different ways. Combinations of several new IPs and the resulting coefficients of determination can be found in Tables 4.3 and 4.4 for the tensile and edgewise bending test series, respectively. In addition to obvious combinations of predictor variables (e.g. all quadratically weighted areas/volumes), statistical methods were used to find the best regression models out of the high number of predictor variables. Within this work, Mallows's C_p (Mallows, 1973) is used for model selection, as it allows the consideration of overfitting, which is the effect of obtaining higher coefficients of determination when

additional predictor variables are added to a regression model. As usually the best model with only the essential, and thus low number of variables, is desired, this approach to reduce the number of predictor variables in such a combination for a new IP was chosen. For a subset model with p chosen predictor variables out of a set of $k > p$ variables, Mallows's C_p statistic is defined as

$$C_p = \frac{SSE_p}{s^2} - (n - 2p), \tag{4.10}$$

where s^2 is the mean squared error (MSE) of the complete set of k regressors, SSE_p the residual sum of squares for the subset model containing p parameters and n the sample size. A plot of C_p versus p can be used to decide on subset models, as for correct models C_p will tend to be close to or smaller than p . Finally, the picked predictor variables are fitted to a linear model to estimate the experimental strengths.

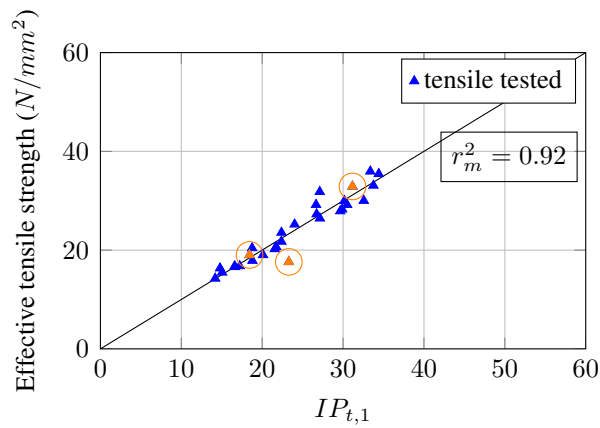


Figure 4.12: Correlation between tensile strength and $IP_{t,1}(KAR, FAR, S_{tb}, S_{lr}, I, V)$ for the manually reconstructed boards.

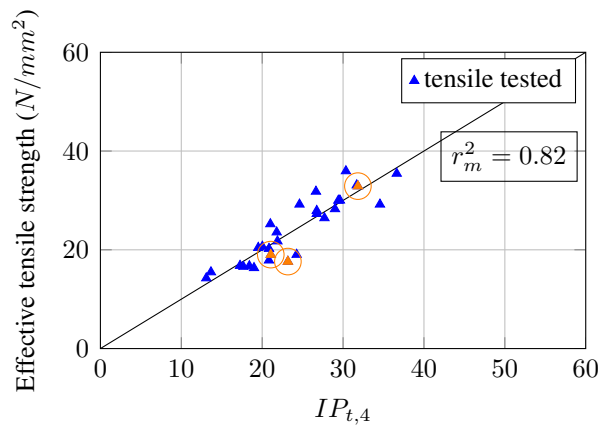


Figure 4.13: Correlation between tensile strength and $IP_{t,4}(KAR, S, I, V)$ for the manually reconstructed boards.

Table 4.3: Indicating properties IP_t and resulting coefficients of determination for tensile tested boards and both manual (r_m^2) and automatical (r_a^2) reconstruction. The marked IPs are discussed in detail.

$IP_{t,\dots}$	KAR	FAR	CAR	S_b	S_{tb}	S_{lr}	S	I	V	h_p	r_m^2	r_a^2
1	•	•			•	•		•	•		0.92	0.83
2	•				•	•		•	•		0.90	0.70
3	•					•		•	•		0.82	0.61
4	•						•	•	•		0.82	0.67
5		•	•					•			0.80	0.47
6	•	•							•		0.80	0.46
7		•	•						•		0.79	0.47
8	•	•	•								0.78	0.45
9			•					•	•		0.78	0.50
10		•	•				•				0.76	0.51
11	•	•									0.74	0.43
12		•	•			•					0.74	0.45
13			•						•	•	0.72	0.54
14					•	•		•	•		0.71	0.55
15			•					•			0.71	0.37
16		•	•							•	0.69	0.56
17		•	•	•							0.68	0.50
18		•	•								0.67	0.43
19	•		•								0.67	0.43
20			•						•		0.67	0.43
21	•										0.62	0.43
22									•		0.59	0.39
23								•			0.58	0.34
24							•				0.54	0.42

For the tensile test series, the marked IPs in Table 4.3 were selected to be discussed in detail. The corresponding correlation plots with the estimated strengths can be found in Figures 4.12 to 4.14. $IP_{t,1}$, which reached the highest coefficient of determination ($r_m^2 = 0.92$), is a function of knot area ratio (KAR), fiber deviation area ratio (FAR), total knot area on top and bottom surface (S_{tb}), on left and right surface (S_{lr}), total interfaces (I) and knot volumes (V). As can be seen in Figure 4.12, the obtained strength values agree very well with the experimentally ones, with the marked values denoting the discussed samples of Figure 4.6. As this high correlation was reached with a number of six predictor values, next $IP_{t,4}$ is investigated, which is a function of only four such predictor values: KAR , total knot area (S), I and V , with two of them using the now available 3D knot information. With this combination still a very good agreement between the estimated and experimental tensile strengths could be obtained. The last

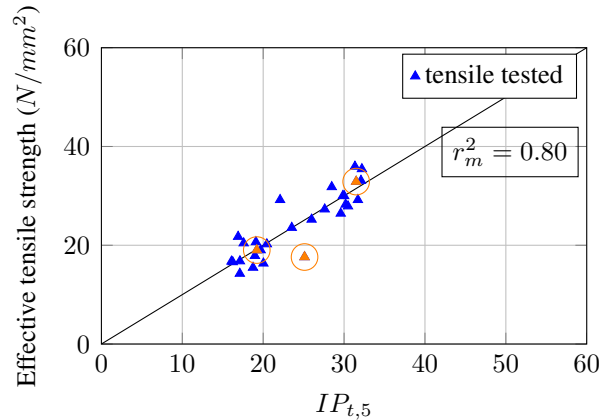


Figure 4.14: Correlation between tensile strength and $IP_{t,5}(KAR, CAR, I)$ for the manually reconstructed boards.

analyzed combination, $IP_{t,5}$, is just based on KAR , clear wood area ratio (CAR) and I , which reaches a coefficient of determination of 0.80, with only some moderate outliers. For example, the strength of the board shown in Figure 4.9 on the bottom left, which is denoted by the marked outlier on the right of the regression line, is overestimated with this IP. Anyhow, the results of both common IPs, KAR and branchiness, can be easily outperformed. In fact, closer inspection of Table 4.3 reveals that even the knot volumes, areas and interfaces by themselves reach similar correlation results as the KAR .

An overview of the evaluated combinations of predictor values resulting in new indicating properties IP_b for wooden boards under edgewise bending, can be found in Table 4.4. Analogously to the tensile tests, three IPs were picked for closer investigation and marked in the overview table. The corresponding correlation plots can be found in Figures 4.15 to 4.17. The highest coefficient of determination was found for $IP_{b,1}$ with a linear model of seven different predictor variables ($r^2 = 0.89$), considering knot volumes, interfaces and knot surfaces, all weighted by their location in the board with respect to the top surface or neutral axis, respectively. By considering these variables, now the strengths of all of the three selected sample boards (marked in Figure 4.15) can be estimated very well. $IP_{b,4}$, plotted in Figure 4.16, combines linearly weighted (with a value of zero at and above the neutral axis, and one at the bottom surface) interfaces (I^L), knot surfaces on the left board surface (S_t^L) and on the bottom surface (S_b), in addition with the clear wood density (ρ_{cw}), in a linear model. This combination of only four predictor variables to a new IP shows still a very good agreement when compared to the experimental strengths ($r^2 = 0.78$). Within this IP only knots lying in the lower half of the board were considered in a weighted fashion. This approach could be confirmed by evaluating the starting points of structural failure during the conducted bending tests, where for almost all experiments failure started at or close to the tensile loaded edge and in the vicinity of knots (Lukacevic et al., 2014a). This can be explained by high fiber deviations in the vicinities of such knots, which on one hand leads to fibers being cut at the bottom surface and on the other hand to high tensile stresses in perpendicular-to-

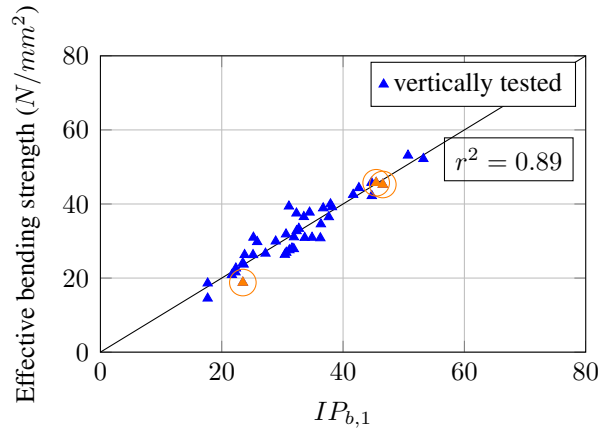


Figure 4.15: Correlation between edgewise bending strength and $IP_{b,1}(V^{\bar{L}}, V^{\bar{Q}}, I, I^L, I^Q, S_{tr}^{\bar{L}}, S_{tr}^{\bar{Q}})$.

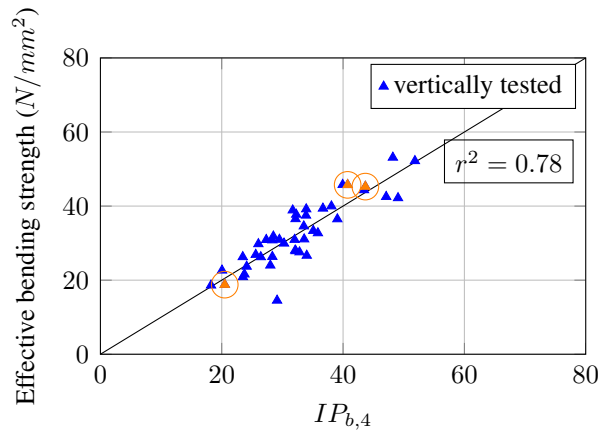


Figure 4.16: Correlation between edgewise bending strength and $IP_{b,4}(\rho_{cw}, \bar{I}^{\bar{L}}, \bar{S}_b^{\bar{L}})$.

grain directions, and thus to discontinuities causing failure. The third examined combination, $IP_{b,6}$ is based on quadratically weighted knot volumes, interfaces and surfaces on both the right and left board surface. Here, as well, a relatively high coefficient of determination ($r^2 = 0.76$) could be obtained. For all three closely examined new IPs, the marked sample boards lie much closer towards the regression line compared to the *KAR* (cf. Figure 4.11).

The assessment of these new IPs shows that, by considering the 3D knot location and morphology, high correlations can be obtained with a reasonable amount of variables. Further common IPs, like various versions of the boards' MOE, were not used within this assessment, as this information was not available for all the boards. Thus, within this work, the focus is on those IPs, which can be obtained by visual methods. Future incorporations of other IPs, like the MOE, should only improve the resulting correlation even further.

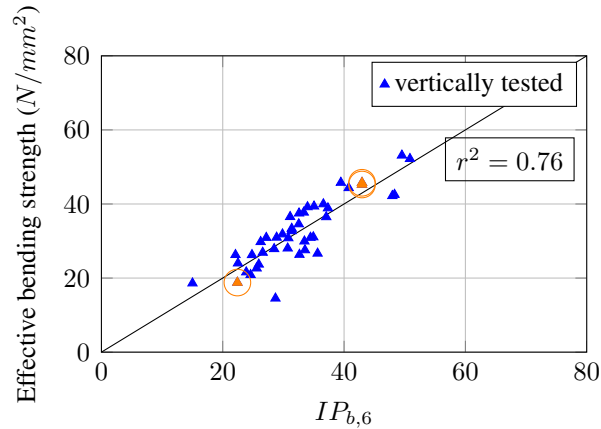


Figure 4.17: Correlation between edgewise bending strength and $IP_{b,6}(V^{\bar{Q}}, I^{\bar{Q}}, S_l^{\bar{Q}}, S_r^{\bar{Q}})$.

4.6 Conclusions

Within this paper, the ability of common and new indicating properties for the strength grading of wooden boards was assessed on the basis of tensile and edgewise bending tests. The new IPs utilize 3D information of knot locations and orientations within the boards, by using interface areas between knots and surrounding clear wood, and knot volumes, which can be obtained by manual or automatic reconstruction of the boards geometry. Additionally, IPs were introduced which are able to take the distance of knot parameters to the tensile loaded edge through weighting functions into account. Based on the obtained results, the following conclusions can be drawn:

- The inability of common IPs to consider the 3D location and morphology of knots within a wooden board was assessed and illustrated by means of selected knot groups. The introduction of new IPs, which use the information obtained from the reconstructed boards, led to strongly improved correlations. This could be confirmed by closely examining several sample boards, whose strength values couldn't be predicted by using the common IPs.
- The presented algorithm for the automatic 3D reconstruction of wooden boards based on laser scanning data shows the high potential of the new developed IPs, which use 3D geometric information. Especially, the latest trend of grading machines, which are utilizing CT data in a high speed scanning process, emphasizes that the use of 3D geometric data will be the future of timber strength grading. Within this work, the coefficient of determination for the automatically reconstructed boards were lower than for the manually reconstructed ones, which is mainly due to the low quality of the available data. Anyhow, still higher correlations compared to common IPs, obtained with the manual reconstruction, could be obtained.
- The separate consideration of tensile and bending load cases can be justified by their differing failure mechanisms. Especially the coefficients of determination

for the bending load case, which is used as the decisive strength property in most standards, were highly improved.

Due to the high effort for the manual reconstruction process, future investigations should focus on the improvement of automatic reconstruction algorithms based on bigger sample sizes. This should finally lead to improved grading procedures on the one hand and on the other hand could be used in the assessment of wood products like Cross-Laminated Timber or Glued Laminated Timber.

Conclusions and Outlook

In the following the main findings of the thesis are summarized and an outlook to future research perspectives, building on the work presented herein, is given.

Main Findings Concerning the Mechanical Behavior of Wooden Boards with Knots

A previously developed numerical simulation tool for wooden boards was adapted and implemented into the commercial FE software `Abaqus`. This simulation tool includes a mechanical model for a density and moisture dependent characterization of the clear-wood material and allows for the description of the 3D fiber course in the vicinity of knots by determining the principle material directions in each integration point directly. This approach not only considers the 2D fiber deviations around a knot in the LT-plane but also incorporates information of the so-called dive angle in the out-of-plane, the global R-direction. To validate the model in the **elastic regime**, i.e. the stress and strain fields resulting from numerical simulations, a comprehensive series of four-point bending tests was conducted. These tests were accompanied by digital image correlation measurements, leading to full-field deformation information for the entire load history. The comparison of the experimentally obtained strain fields to the simulation results proved the capability of the simulation tool to reproduce the mechanical behavior in the vicinity of knots under edgewise bending load, when a few deficiencies are kept in mind. The rigid body motions of cracked edges led to an overestimation of the actual strain values in these areas. Otherwise, the agreement of both experimentally and numerically obtained strain fields was very good, as not only the visual comparison of the respective contour plots showed good agreement, but also the evaluation of strain peak positions and magnitudes showed no big discrepancies. Additionally, the comparison of principle strain directions showed clearly identifiable similarities, especially in areas with large strains, which can be mainly attributed to the high accuracy of the computed 3D fiber course based on a 3D reconstruction of the tested specimens.

Further, the numerical simulation tool is now able to determine the effective strength of wooden boards by means of a **structural failure** criterion based on the evaluation of stress states in the vicinity of knots. This approach considers the morphology of knots, which in reality are the main cause for the qualitative downgrading of timber elements. It was assumed that the point of global failure can be related to the point of starting

stress transfer mechanisms. By investigating the stress states in the vicinity of knots, this stress transfers are clearly identifiable. Another noteworthy characteristic of this approach is the lack of empirical parameters, meaning that no identification experiments are required to calibrate the structural failure criterion. Comparisons of the numerical simulations to the results of the mentioned four-point bending tests and also to previously conducted tensile tests showed a very good agreement of the strength values.

Minor deficiencies of the presented structural failure criterion and the wish for the realistic simulation of the **failure mechanisms** in wood led to the development of a multisurface failure criterion, which allows for the realistic determination of not only crack initiation but also global crack direction, and thus of the entire crack path. This was accomplished by thorough investigations of the failure mechanisms of late- and earlywood by using an approach based on XFEM. To account for the different failure mechanisms within the two wood layer types, the investigations were based on so-called unit cells, which are able to represent the repetitive structure of wood within these layers, namely the honeycomb-like structure in the RT-plane. By using individual material descriptions and failure criteria for the most important cell components, i.e. for the middle lamella and the cell wall, two unit cell models were developed. The application of latin hypercube sampling enabled the generation of a large number of samples (800 each) with a large variability of loading conditions for the normal and shear components. By subjecting the unit cells to these loading conditions and by using periodic boundary conditions, all possible failure mechanisms and the transition points in between could be determined. The classification of the resulting failure mechanisms, the determination of failure surfaces for each failure mode and, finally, the assignment of global crack directions, led to the definition of two multisurface failure criteria for both early- and latewood individually. These criteria, which allow the numerical determination of crack initiation with assigned global crack directions, was applied to tensile tests on the annual year ring scale. Comparisons to experiments for several fiber to loading angles showed a very good agreement.

Although the abovementioned approaches describe powerful tools for the description of the mechanical behavior of timber elements, their direct implementation to **practical applications** in the timber industry are problematical. Their primary field of application are the assessment of complex timber structures, the evaluation of the mechanical behavior of structural elements and the design of new wood products. Thus, the focus of the last part of this work was put on the evaluation of common and the development of novel indicating properties (IPs) for the strength grading of wooden boards. Here, the 3D reconstruction information of knots and wooden boards, obtained during the mentioned experiments, were used to find better ways to incorporate the morphology of knots by using the 3D information on knot location and orientation within boards. The inability of common IPs to consider these morphologies was assessed and illustrated by means of selected knot groups. The newly developed IPs were based on interface areas between knots and surrounding clear wood and knot volumes. In addition, IPs for the edgewise bending strength were obtained by considering the distance of the just

mentioned knot parameters to the tensile loaded edge through weighting functions. A statistical analysis of the IPs proved the enhanced capability of estimating strength properties by including the additional information on knots. Algorithms for the manual and automatic 3D reconstruction of wooden boards based on laser scanning data were presented and the possible incorporation of CT data in a high speed scanning process was discussed.

In summary it can be stated that 3D numerical simulations represent a promising approach for the performance prediction of wooden boards. Advanced identification methods for the timber morphology, like laser scanning and computer tomography, deliver necessary input data for such simulation tools and surface-based measurement techniques allow for sufficient validation. Sophisticated material models even allow the description of complex mechanical processes in wood.

Thus, numerical simulations are a useful addition to experimental studies and can strongly contribute to new insights into the complex mechanical behavior of wood and wood products.

Perspectives and Future Research Studies

The most recent development of the multisurface failure criteria for latewood and earlywood individually predetermines the focus of the immediate next steps of future research studies. By defining another repetitive unit on the next higher length scale and by using the same approach of the unit cell method in combination with a large sample of loading conditions, the homogenized **failure mechanisms for clear wood** could be determined in a straightforward manner. In addition, in future implementations the failure surfaces, which are mostly under compression, will serve as criteria for the start of plastic behavior instead of cracking, which will lead to an increased performance of this tool. The resulting multisurface failure criterion would enable the realistic determination of crack initiation and also crack direction in the framework of XFEM. Consequentially, the next step is the implementation of this criterion into the framework of the numerical simulation tool for wooden boards, which enables the realistic calculation of fiber deviations in the vicinity of knots. Furthermore, this model can easily be extended to study also wood products, like Glued Laminated Timber or Cross-Laminated Timber.

Simultaneously, the **validation** of this modeling approach must be conducted at several length scales as well, from comparisons to experiments with regard to fracture energy, comparisons with 2D fracture mechanisms found in literature up to comparisons with full-scale strength tests of wooden boards with knots.

The simulation tool will also be used for further improvements of indicating properties. Parameter studies of critical knot configurations should be the basis for the evaluation and optimization of current methods in the **strength grading** of wooden boards. In addition, the enhancement of automatic reconstruction algorithms with regard to knot morphologies and 3D location information with the incorporation of novel scanning techniques, will lead to to a much higher accuracy in the determination of effective strength properties.

Bibliography

- Aicher, S., Gustafsson, P. J., Haller, P., and Petersson, H. (2002). Fracture mechanics models for strength analysis of timber beams with a hole or a notch—a report of ritem tc-133.
- Babuska, I. and Melenk, J. M. (1997). The partition of unity method. *Int. J. Numer. Meth. Engng.*, 40(4):727–758.
- Bader, T. K., Hofstetter, K., Hellmich, C., and Eberhardsteiner, J. (2010). Poromechanical scale transitions of failure stresses in wood: from the lignin to the spruce level. *ZAMM-Journal of Applied Mathematics and Mechanics/Zeitschrift für Angewandte Mathematik und Mechanik*, 90(10-11):750–767.
- Bader, T. K., Hofstetter, K., Hellmich, C., and Eberhardsteiner, J. (2011). The poroelastic role of water in cell walls of the hierarchical composite softwood. *Acta Mechanica*, 217(1-2):75–100.
- Belytschko, T. and Black, T. (1999). Elastic crack growth in finite elements with minimal remeshing. *Int. J. Numer. Meth. Engng.*, 45(5):601–620.
- Blaß, H. and Frese, M. (2004). Sortierverfahren für die kombinierte maschinelle und visuelle festigkeitssortierung. *Holz als Roh- und Werkstoff*, 62(5):325–334.
- Böhm, H. J. (2004). *A short introduction to continuum micromechanics*. Springer.
- Castera, P., Faye, C., and El Ouadrani, A. (1996). Prevision of the bending strength of timber with a multivariate statistical approach. In *Annales des sciences forestières*, volume 53, pages 885–896. EDP Sciences.
- Cramer, S. and Goodman, J. (1983). Model for stress analysis and strength prediction of lumber. *Wood Fiber Science*, 15(4):338–349.
- Danielsson, H. and Gustafsson, P. J. (2014). Fracture analysis of glued laminated timber beams with a hole using a 3D cohesive zone model. *Engineering Fracture Mechanics*, 124–125:182–195.
- Dantec Dynamics (2012). ISTRA 4D Software Manual Q-400 System. Manual Version: 2.4.0, Software Version 4.3.1.379.

- Dias, A., Van De Kuilen, J., Cruz, H., and Lopes, S. (2010). Numerical modeling of the load-deformation behavior of doweled softwood and hardwood joints. *Wood and Fiber Science*, 42(4):480–489.
- Dias, A., Van de Kuilen, J., Lopes, S., and Cruz, H. (2007). A non-linear 3D FEM model to simulate timber-concrete joints. *Advances in Engineering Software*, 38(8-9):522–530.
- Dill-Langer, G., Lütze, S., and Aicher, S. (2002). Microfracture in wood monitored by confocal laser scanning microscopy. *Wood Science and Technology*, 36(6):487–499.
- DIN 4074-1 (2012). Sortierung von Holz nach der Tragfähigkeit – Teil 1: Nadelschnittholz. In German.
- DIN EN 14081-2 (2013). Holzbauwerke - Nach Festigkeit sortiertes Bauholz für tragende Zwecke mit rechteckigem Querschnitt - Teil 2: Maschinelle Sortierung; zusätzliche Anforderungen an die Erstprüfung. In German.
- DIN EN 14081-3 (2012). Holzbauwerke - Nach Festigkeit sortiertes Bauholz für tragende Zwecke mit rechteckigem Querschnitt - Teil 3: Maschinelle Sortierung, zusätzliche Anforderungen an die werkseigene Produktionskontrolle. In German.
- DIN EN 14358 (2013). Holzbauwerke - Berechnung der charakteristischen 5%-Quantile und Mittelwerte für Erstprüfung und werkseigene Produktionskontrolle. In German.
- DIN EN 1912 (2013). Bauholz für tragende Zwecke - Festigkeitsklassen - Zuordnung von visuellen Sortierklassen und Holzarten. In German.
- DIN EN 338 (2013). Bauholz für tragende Zwecke - Festigkeitsklassen. In German.
- DIN EN 384 (2013). Bauholz für tragende Zwecke - Bestimmung charakteristischer Werte für mechanische Eigenschaften und Rohdichte. In German.
- DIN EN 408 (2010a). Holzbauwerke – Bauholz für tragende Zwecke und Brettschichtholz – Bestimmung einiger physikalischer und mechanischer Eigenschaften. In German.
- DIN EN 408 (2010b). Holzbauwerke – Bauholz für tragende Zwecke und Brettschichtholz – Bestimmung einiger physikalischer und mechanischer Eigenschaften. In German.
- Divos, F. and Kiss, S. (2010). Strength grading of structural lumber by portable lumber grading-effect of knots. In *The Future of Quality Control for Wood & Wood Products The Final Conference of COST Action E*, volume 53.
- Dorn, M. (2012). *Investigations on the serviceability limit state of dowel-type timber connections*. PhD thesis, Vienna University of Technology.

- Dorn, M., de Borst, K., and Eberhardsteiner, J. (2013). Experiments on dowel-type timber connections. *Engineering Structures*, 47:67–80.
- Dubois, F., Mèitè, M., Pop, O., and Absi, J. (2012). Characterization of timber fracture using the digital image correlation technique and finite element method. *Engineering Fracture Mechanics*, 96:107–121.
- Eberhardsteiner, J. (2002). *Mechanisches Verhalten von Fichtenholz: Experimentelle Bestimmung der biaxialen Festigkeitseigenschaften*. Springer Wien, New York. In German.
- El Omri, A., Fennan, A., Sidoroff, F., and Hihi, A. (2000). Elastic-plastic homogenization for layered composites. *European Journal of Mechanics - A/Solids*, 19(4):585–601.
- Fengel, D. and Wegener, G. (1983). *Wood: chemistry, ultrastructure, reactions*. Walter de Gruyter.
- Foley, C. (2003). *Modelling the effects of knots in structural timber*. PhD thesis, Lund University.
- Fries, T.-P. and Belytschko, T. (2010). The extended/generalized finite element method: An overview of the method and its applications. *Int. J. Numer. Meth. Engng.*, 84(3):253–304.
- Frühmann, K., Burgert, I., Stanzl-Tschegg, S., and Tschegg, E. (2003). Mode I fracture behaviour on the growth ring scale and cellular level of spruce (*Picea abies* [L.] Karst.) and beech (*Fagus sylvatica* L.) loaded in the transverse crack propagation system. *Holz-forschung*, 57(6):653–660.
- Gloimüller, S. (2012). *Multiscale modeling and experimental investigation of the hygroexpansion behavior of softwood*. PhD thesis, Vienna University of Technology.
- Glos, P. and Burger, N. (1998). Maschinelle Sortierung von frisch eingeschnittenem Schnittholz. 56(5):319–329.
- Goodman, J. and Bodig, J. (1978). Mathematical model of the tension behaviour of wood with knots and cross grain. In *Proceedings from the First Int. Conf. On Wood Fracture*.
- Gravouil, A., Moës, N., and Belytschko, T. (2002). Non-planar 3D crack growth by the extended finite element and level sets-part II: Level set update. *International Journal for Numerical Methods in Engineering*, 53(11):2569–2586.
- Griessner, M. (2013). Bending strength of wooden boards with knots – evaluation of experiments using full-field deformation measurements as a basis for the optimization of a 3D numerical simulation tool. Master’s thesis, Vienna University of Technology.

- Guindos, P. (2011). *Three-dimensional Finite Element models to simulate the behavior of wood with presence of knots, applying the flow-grain analogy and validation with close range photogrammetry*. PhD thesis, University of Santiago de Compostela, Department of Agroforestry Engineering.
- Guindos, P. and Guaita, M. (2013). A three-dimensional wood material model to simulate the behavior of wood with any type of knot at the macro-scale. *Wood Science and Technology*, 47(3):585–599.
- Hackspiel, C. (2010). *A numerical simulation tool for wood grading*. PhD thesis, Vienna University of Technology.
- Hanhijärvi, A. and Ranta-Maunus, A. (2008). Development of strength grading of timber using combined measurement techniques. *VTT, Espoo*.
- Hanhijärvi, A., Ranta-Maunus, A., and Turk, G. (2005). *Potential of strength grading of timber with combined measurement techniques: report of the Combigrade-project, phase I*. VTT Technical Research Centre of Finland.
- Hansbo, A. and Hansbo, P. (2004). A finite element method for the simulation of strong and weak discontinuities in solid mechanics. *Computer Methods in Applied Mechanics and Engineering*, 193(33-35):3523–3540.
- Hatayama, Y. (1983). A new estimation of structural lumber considering the slope of grain around the knots. *Bulletin, Forestry and Forest Products Research Institute Japan*, 326:69–167.
- Hepworth, D. and Vincent, J. (1998). Modelling the mechanical properties of xylem tissue from tobacco plants (*nicotiana tabacum* 'samsun') by considering the importance of molecular and micromechanisms. *Annals of Botany*, 81(6):761–770.
- Hill, R. (1948). A theory of the yielding and plastic flow of anisotropic metals. *Proceedings of the Royal Society of London. Series A. Mathematical and Physical Sciences*, 193(1033):281–297.
- Hoffman, O. (1967). The brittle strength of orthotropic materials. *Journal of Composite Materials*, 1(2):200–206.
- Hofstetter, K., Hellmich, C., and Eberhardsteiner, J. (2005). Development and experimental validation of a continuum micromechanics model for the elasticity of wood. *European Journal of Mechanics A/Solids*, 24:1030–1053.
- Hofstetter, K., Hellmich, C., and Eberhardsteiner, J. (2007). Micromechanical modeling of solid-type and plate-type deformation patterns within softwood materials. A review and an improved approach. *Holzforschung*, 61(4):343–351.

- Hu, M., Johansson, M., Olsson, A., Bengtsson, C., and Brandt, A. (2011). Grading of sawn timber using the vibration technique : locating imperfections based on flexural mode shapes. In *17th international nondestructive testing and evaluation of wood symposium*, pages 269–276. University of West Hungary.
- Johansson, C.-J. (2003). *Timber Engineering*, chapter 3, pages 23–43. J. Wiley.
- Johansson, C.-J., Brundin, J., and Gruber, R. (1992). Stress grading of swedish and german timber - a comparison of machine stress grading and three visual grading systems. Technical Report 23, Swedish National Testing and Research Institute.
- Karihaloo, B. L. (1995). *Fracture mechanics and structural concrete*. Longman Scientific & Technical Harlow, Essex, England.
- Kohlhauser, C. (2009). *Elasticity tensor determination by means of ultrasonic pulse transmission*. PhD thesis, Vienna University of Technology.
- Kollmann, F. (1982). *Technologie des Holzes und der Holzwerkstoffe*. Springer-Verlag, zweite Auflage / erster Band.
- Landelius, J. (1989). Finit area metoden. en bra metod för beräkning av uppfläckningsbrott? *Rep. No. TVSM*, 5043:66. In Swedish.
- Lang, R. and Kaliske, M. (2013). Description of inhomogeneities in wooden structures: modelling of branches. *Wood Science and Technology*, 47.
- Larsson, D., Ohlsson, S., Perstorper, M., and Brundin, J. (1998). Mechanical properties of sawn timber from norway spruce. 56(5):331–338.
- Le Magorou, L., Bos, F., and Rouger, F. (2002). Identification of constitutive laws for wood-based panels by means of an inverse method. *Composites Science and Technology*, 62(4):591–596.
- Lei, Y., Zhang, S., and Jiang, Z. (2005). Models for predicting lumber bending mor and moe based on tree and stand characteristics in black spruce. *Wood Science and Technology*, 39(1):37–47.
- Lukacevic, M. (2009). Validation and optimization of a numerical simulation tool for wood grading. Master's thesis, Vienna University of Technology.
- Lukacevic, M. and Füssl, J. (2014). Numerical simulation tool for wooden boards with a physically based approach to identify structural failure. *European Journal of Wood and Wood Products*, 72(4):497–508.
- Lukacevic, M., Füssl, J., and Eberhardsteiner, J. (2014c). Discussion of common and introduction of new indicating properties for the strength grading of wooden boards. *Wood Science and Technology*. Submitted to.

- Lukacevic, M., Füssl, J., Griessner, M., and Eberhardsteiner, J. (2014a). Performance assessment of a numerical simulation tool for wooden boards with knots by means of full-field deformation measurements. *Strain*. (in press).
- Lukacevic, M., Füssl, J., and Lampert, R. (2014b). Failure mechanisms of clear wood identified at wood cell level by an approach based on the extended finite element method. *Computational Materials Science*. Submitted to.
- Mackenzie-Helnwein, P., Eberhardsteiner, J., and Mang, H.A. (2003). A multi-surface plasticity model for clear wood and its application to the finite element analysis of structural details. *Computational Mechanics*, 31(1–2):204–218.
- Mallows, C. L. (1973). Some comments on c_p . *Technometrics*, 15(4):661–675.
- Masuda, M. (1988). Theoretical consideration on fracture criteria of wood dproposal of finite small area theory. In *Proceedings of the 1988 International Conference on Timber Engineering, Seattle*, volume 2, pages 584–595.
- Mattheck, C. (1997). *Design in der Natur*. Rombach Verlag, Freiburg. In German.
- McKay, M. D., Beckman, R. J., and Conover, W. J. (1979). A comparison of three methods for selecting values of input variables in the analysis of output from a computer code. *Technometrics*, 21(2):239–245.
- Melenk, J. and Babuska, I. (1996). The partition of unity finite element method: Basic theory and applications. *Computer Methods in Applied Mechanics and Engineering*, 139(1):289–314.
- Michel, J., Moulinec, H., and Suquet, P. (1999). Effective properties of composite materials with periodic microstructure: a computational approach. *Computer methods in applied mechanics and engineering*, 172(1):109–143.
- Moës, N., Cloirec, M., Cartraud, P., and Remacle, J.-F. (2003). A computational approach to handle complex microstructure geometries. *Computer Methods in Applied Mechanics and Engineering*, 192(28):3163–3177.
- Moës, N., Dolbow, J., and Belytschko, T. (1999). A finite element method for crack growth without remeshing. 46(1):131–150.
- Moës, N., Gravouil, A., and Belytschko, T. (2002). Non-planar 3D crack growth by the extended finite element and level sets-part i: Mechanical model. *International Journal for Numerical Methods in Engineering*, 53(11):2549–2568.
- Mori, T. and Tanaka, K. (1973). Average stress in matrix and average elastic energy of materials with misfitting inclusions. *Acta Metallurgica*, Volume 21, Issue 5:571–574.
- Murata, K., Masuda, M., and Ukyo, S. (2006). Analysis of strain distribution of wood using digital image correlation method—four-point bend test of timber including knots. *Transactions of the Visualization Society of Japan*, pages 57–63. In Japanese.

- Nagai, H., Murata, K., and Nakano, T. (2011). Strain analysis of lumber containing a knot during tensile failure. *Journal of Wood Science*, 57(2):114–118.
- Olsson, A., Oscarsson, J., Johansson, M., and Källsner, B. (2012). Prediction of timber bending strength on basis of bending stiffness and material homogeneity assessed from dynamic excitation. *Wood Science and Technology*, 46(4):667–683.
- Olsson, A., Oscarsson, J., Serrano, E., Källsner, B., Johansson, M., and Enquist, B. (2013). Prediction of timber bending strength and in-member cross-sectional stiffness variation on the basis of local wood fibre orientation. *European Journal of Wood and Wood Products*, 71(3):319–333.
- Oscarsson, J., Olsson, A., and Enquist, B. (2012). Strain fields around knots in norway spruce specimens exposed to tensile forces. *Wood Science and Technology*, 46(4):593–610.
- Osher, S. and Sethian, J. A. (1988). Fronts propagating with curvature-dependent speed: Algorithms based on hamilton-jacobi formulations. *Journal of Computational Physics*, 79(1):12–49.
- Petersson, H. (2010a). Strength grading and prediction of shape stability by use of optical and laser-based scanning techniques. In *WCTE 2010, World Conference on Timber Engineering*.
- Petersson, H. (2010b). Use of optical and laser scanning techniques as tools for obtaining improved FE-input data for strength and shape stability analysis of wood and timber. In *IV European Conference on Computational Mechanics*, Paris. May 2010.
- Phillips, G., Bodig, J., and Goodman, J. (1981). Flow-grain analogy. *Wood Science*, 14(2):55–64.
- Piter, J., Zerbino, R., and Blaß, H. (2004a). Machine strength grading of argentinean eucalyptus grandis : Main grading parameters and analysis of strength profiles according to european standards. *Holz als Roh- und Werkstoff*, 62(1):9–15.
- Piter, J., Zerbino, R., and Blaß, H. (2004b). Visual strength grading of argentinean eucalyptus grandis. *Holz als Roh- und Werkstoff*, 62(1):1–8.
- Puck, A. (1996). *Festigkeitsanalyse von Faser-Matrix-Laminaten: Modelle für die Praxis*. Hanser München. In German.
- Puck, A. and Schuermann, H. (1998). Failure analysis of frp laminates by means of physically based phenomenological models. *Composites Science and Technology*, 58(7):1045–1067.
- Rabczuk, T., Zi, G., Gerstenberger, A., and Wall, W. A. (2008). A new crack tip element for the phantom-node method with arbitrary cohesive cracks. *Int. J. Numer. Meth. Engng.*, 75(5):577–599.

- Ranta-Maunus, A., Denzler, J., and Stapel, P. (2011). Strength of european timber. part 2. properties of spruce and pine tested in gradewood project. Technical report, VTT Technical Research Centre of Finland, Espoo, Finland.
- Resch, E. and Kaliske, M. (2005). Bestimmung des Faserverlaufs bei Fichtenholz. Technical Report 10:117–130, Leipzig Annual Civil Engineering Report.
- Roblot, G., Bleron, L., Meriaudeau, F., and Marchal, R. (2010). Automatic computation of the knot area ratio for machine strength grading of douglas-fir and spruce timber. *European Journal of Environmental and Civil Engineering*, 14(10):1317–1332.
- Samson, M. and Blanchet, L. (1992). Effect of knots on the flatwise bending stiffness of lumber members. *Holz als Roh- und Werkstoff*, 50(4):148–152.
- Sandhaas, C., van de Kuilen, J.-W., and Blass, H. (2012). A 3D constitutive wood model using the concepts of continuum damage mechanics. In Eberhardsteiner, J., Böhm, H., and Rammerstorfer, F., editors, *CD-ROM Proceedings of the 6th European Congress on Computational Methods in Applied Sciences and Engineering (ECCOMAS 2012)*. Vienna University of Technology, Austria. ISBN: 978-3-9502481-9-7.
- Schmidt, J. and Kaliske, M. (2006). Zur dreidimensionalen Materialmodellierung von Fichtenholz mittels eines Mehrflächen-Plastizitätsmodells. 64(5):393–402.
- Schmidt, J. and Kaliske, M. (2007). Simulation of cracks in wood using a coupled material model for interface elements. *Holzforschung*, Volume 61, Issue 4.
- Schmidt, J. and Kaliske, M. (2009). Models for numerical failure analysis of wooden structures. *Engineering Structures*, 31(2):571–579.
- Schniewind, A. and Centeno, J. (1973). Fracture toughness and duration of load factor I. Six principal systems of crack propagation and the duration factor for cracks propagating parallel to grain. *Wood and Fiber Science*, 52:152–159.
- Serrano, E. and Enquist, B. (2005). Contact-free measurement and non-linear finite element analyses of strain distribution along wood adhesive bonds. *Holzforschung*, 59(6):641–646.
- Serrano, E. and Gustafsson, J. (2006). Fracture mechanics in timber engineering - strength analyses of components and joints. *Material and Structures*, 40:87–96.
- Shigo, A. (1990). *Die neue Baumbiologie*. Bernhard Thalacker, Braunschweig. In German.
- Sjödin, J., Enquist, B., and Serrano, E. (2006). Contact-free measurements and numerical analyses of the strain distribution in the joint area of steel-to-timber dowel joints. *Holz als Roh - und Werkstoff*, 64(6):497–506.
- Sjödin, J. and Serrano, E. (2008). A numerical study of methods to predict the capacity of multiple steel-timber dowel joints. *Holz als Roh - und Werkstoff*, 66(6):447–454.

- Sjödin, J., Serrano, E., and Enquist, B. (2008). An experimental and numerical study of the effect of friction in single dowel joints. *Holz als Roh - und Werkstoff*, 66(5):363–372.
- Song, J.-H., Areias, P. M. A., and Belytschko, T. (2006). A method for dynamic crack and shear band propagation with phantom nodes. *Int. J. Numer. Meth. Engng.*, 67(6):868–893.
- Stapel, P. and van de Kuilen, J.-W. G. (2013a). Efficiency of visual strength grading of timber with respect to origin, species, cross section, and grading rules: a critical evaluation of the common standards. *Holzforschung*, 68(2):203–216.
- Stapel, P. and van de Kuilen, J.-W. G. (2013b). Influence of cross-section and knot assessment on the strength of visually graded norway spruce. *European Journal of Wood and Wood Products*, 72(2):213–227.
- Steffen, A., Johansson, C.-J., and Wormuth, E.-W. (1997). Study of the relationship between flatwise and edgewise modull of elasticity of sawn timber as a means to improve mechanical strength grading technology. *Holz als Roh-und Werkstoff*, 55(2-4):245–253.
- Steiger, R. and Arnold, M. (2009). Strength grading of norway spruce structural timber: revisiting property relationships used in en 338 classification system. 43(3-4):259–278.
- Stingray F-504bc (2013). <http://www.alliedvisiontec.com/emea/products/cameras/firewire/stingray/f-504bc.html>. 01.11.2013.
- Sukumar, N., Chopp, D., Moës, N., and Belytschko, T. (2001). Modeling holes and inclusions by level sets in the extended finite-element method. *Computer Methods in Applied Mechanics and Engineering*, 190(46):6183–6200.
- Suquet, P. (1997). *Continuum micromechanics*. Springer-Verlag New York, Inc.
- Sutton, M., Mingqi, C., Peters, W., Chao, Y., and McNeill, S. (1986). Application of an optimized digital correlation method to planar deformation analysis. *Image and Vision Computing*, 4(3):143–150.
- Sutton, M., Wolters, W., Peters, W., Ranson, W., and McNeill, S. (1983). Determination of displacements using an improved digital correlation method. *Image and Vision Computing*, 1(3):133–139.
- Tsai, S. W. (1965). Strength characteristics of composite materials. Technical report, Philco Corp, Newport Beach, CA.
- Tsai, S. W. and Wu, E. M. (1971). A general theory of strength for anisotropic materials. *Journal of composite materials*, 5(1):58–80.

- Wells, G. N. and Sluys, L. J. (2001). A new method for modelling cohesive cracks using finite elements. *Int. J. Numer. Meth. Engng.*, 50(12):2667–2682.
- Wittel, F., Dill-Langer, G., and Kröplin, B.-H. (2005). Modeling of damage evolution in soft-wood perpendicular to grain by means of a discrete element approach. *Computational Materials Science*, 32(3-4):594–603.
- Xavier, J., Belini, U., Pierron, F., Morais, J., Lousada, J., and Tomazello, M. (2013). Characterisation of the bending stiffness components of MDF panels from full-field slope measurements. 47(2):423–441.
- Xavier, J., de Jesus, A., Morais, J., and Pinto, J. (2012). Stereovision measurements on evaluating the modulus of elasticity of wood by compression tests parallel to the grain. *Construction and Building Materials*, 26(1):207–215.
- Zandbergs, J. and Smith, F. (1988). Finite element fracture prediction for wood with knots and cross grain. *Wood Fiber Science*, 20(1):97–106.
- Zaoui, A. (2002). Continuum micromechanics: survey. *Journal of Engineering Mechanics*, 128(8):808–816.
- Zimmermann, T., Sell, J., and Eckstein, D. (1994). Rasterelektronenmikroskopische Untersuchungen an Zugbruchflächen von Fichtenholz. *Holz als Roh-und Werkstoff*, 52(4):223–229. In German.

Publications and Conference Contributions

Publications

Lukacevic, M., Füssl, J.:

Numerical simulation tool for wooden boards with a physically based approach to identify structural failure,

European Journal of Wood and Wood Products, 72 (2014), 4, 497–508.

Lukacevic, M., Füssl, J., Griessner, M., Eberhardsteiner, J.:

Performance Assessment of a Numerical Simulation Tool for Wooden Boards with Knots by Means of Full-Field Deformation Measurements,

Strain, (2014), DOI: 10.1111/str.12093.

Hackspiel, C., de Borst, K., Lukacevic, M.:

A Numerical Simulation Tool for Wood Grading Model Development,

Wood Science and Technology, 48 (2014), 3, 633–649.

Hackspiel, C., de Borst, K., Lukacevic, M.:

A Numerical Simulation Tool for Wood grading: Model Validation and Parameter Studies,

Wood Science and Technology, 48 (2014), 3, 651–669.

Füssl, J., Lukacevic, M., Kandler, G., Eberhardsteiner, J.:

A Comprehensive Mechanical Modeling Approach for the Design of Wood-based Products,

IACM Expressions, 35 (2014), 8–12.

Conference Papers

Lukacevic, M., Füssl, J.:

A Criterion for the Effective Bending Strength of Wooden Boards with Knots Derived by a 3 D Finite-Element Tool,

In: *Forschungskolloquium Holzbau "Forschung und Praxis,* Universität Stuttgart, Stuttgart, 2012.

Conference Presentations and Posters

Lukacevic, M., de Borst, K., Füssl, J., Eberhardsteiner, J.:

A criterion for the effective bending strength of wooden boards derived by a 3D Finite-Element tool,

Forschungskolloquium Holzbau "Forschung und Praxis", Stuttgart, Germany, 12/03/2012–13/03/2012 (oral presentation).

Lukacevic, M., de Borst, K., Füssl, J., Eberhardsteiner, J.:

A criterion for the effective bending strength of wooden boards with knots derived by a 3D Finite-Element tool,

6th European Congress on Computational Methods in Applied Sciences and Engineering (ECCOMAS 2012), Vienna, Austria, 10/09/2012–14/09/2012 (oral presentation).

Lukacevic, M., Füssl, J., Eberhardsteiner, J.:

A criterion for the effective bending strength of wooden boards with knots derived by a 3D Finite-Element tool,

COST Young Researchers' Forum at the 8th FTP Conference, Barcelona, Spain, 11/03/2013–12/03/2013 (poster presentation).

Lukacevic, M., Füssl, J., Eberhardsteiner, J.:

Influence of knot groups on effective mechanical properties of solid-wood based products determined by means of 3D Finite-Element simulations,

International Conference of the Engineering Mechanics Institute (EMI 2013), Evanston, IL, USA, 04/08/2013–07/08/2013 (oral presentation).

Lukacevic, M., Füssl, J., Eberhardsteiner, J.:

Influence of knot groups on effective mechanical properties of solid-wood based products determined by means of 3D Finite-Element simulations,

12th International Conference on Computational Plasticity (COMPLAS XII), Barcelona, Spain, 03/09/2013–05/09/2013 (oral presentation).

Lukacevic, M., Füssl, J., Eberhardsteiner, J.:

Numerical simulation tool for wooden boards with knots,

5th European Conference on Computational Mechanics (ECCM V), Barcelona, Spain, 20/07/2014–25/07/2014 (oral presentation).

Curriculum Vitae

Personal Data

Name: **Dipl.-Ing. Markus LUKACEVIC**
Date of Birth: 17th July 1983
Place of Birth: Vienna, Austria
Nationality: Austrian
Current address: Embelgasse 54/11, 1050 Vienna, Austria

Education

04/2009 – 07/2014 Doctoral studies in Civil Engineering at Vienna University of Technology, Vienna, Austria
10/2003 – 03/2009 Diploma studies in Civil Engineering at Vienna University of Technology, Vienna, Austria
09/1997 – 06/2002 High school student in Civil and Environmental Engineering, Mödling, Austria

Activities Abroad

06/2010 COST Action FP0802 “Trainingsschool on Experimental Techniques”, Max Planck Institute for Colloids and Interfaces, Potsdam-Golm, Germany
08/2006 – 01/2007 Exchange student, University of Illinois at Urbana-Champaign, IL, USA

Awards

2009 Award of the city of Vienna for excellent diploma theses at the Vienna University of Technology
2007, 2008, 2009 Award for excellent performance as a student, granted by the Faculty of Civil Engineering, Vienna University of Technology
2002 Honorary ring for excellent performance as a student, granted by the alumni association of the HTBLuVA Mödling